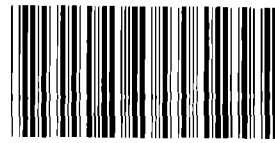


CONTRACTOR REPORT

SAND91-7012
Unlimited Release
UC-261



8533848

**SANDIA NATIONAL
LABORATORIES
TECHNICAL LIBRARY**

Stress Calculation for the Sandia 34-Meter Wind Turbine Using the Local Circulation Method and Turbulent Wind

B. Masse, H. Pastorel
Institut de recherche d'Hydro-Quebec
800 Montee Sainte Julie
Varenes, Quebec J3X 1s1
Canada

Prepared by Sandia National Laboratories Albuquerque, New Mexico 87185
and Livermore, California 94550 for the United States Department of Energy
under Contract DE-AC04-76DP00789

Printed November 1992

Issued by Sandia National Laboratories, operated for the United States Department of Energy by Sandia Corporation.

NOTICE: This report was prepared as an account of work sponsored by an agency of the United States Government. Neither the United States Government nor any agency thereof, nor any of their employees, nor any of their contractors, subcontractors, or their employees, makes any warranty, express or implied, or assumes any legal liability or responsibility for the accuracy, completeness, or usefulness of any information, apparatus, product, or process disclosed, or represents that its use would not infringe privately owned rights. Reference herein to any specific commercial product, process, or service by trade name, trademark, manufacturer, or otherwise, does not necessarily constitute or imply its endorsement, recommendation, or favoring by the United States Government, any agency thereof or any of their contractors or subcontractors. The views and opinions expressed herein do not necessarily state or reflect those of the United States Government, any agency thereof or any of their contractors.

Printed in the United States of America. This report has been reproduced directly from the best available copy.

Available to DOE and DOE contractors from
Office of Scientific and Technical Information
PO Box 62
Oak Ridge, TN 37831

Prices available from (615) 576-8401, FTS 626-8401

Available to the public from
National Technical Information Service
US Department of Commerce
5285 Port Royal Rd
Springfield, VA 22161

NTIS price codes
Printed copy: A05
Microfiche copy: A01

Distribution
Category UC-261

SAND91-7012
Unlimited Release
Printed November 1992

Stress Calculation for the Sandia 34-Meter Wind Turbine Using the Local Circulation Method and Turbulent Wind

B. Masse and H. Pastorel
Institut de recherche d'Hydro-Quebec
800 Montee Sainte Julie
Varenes, Quebec J3X 1s1
Canada

Sandia Contract 55-2631

ABSTRACT

Stress calculation for wind turbine blades is an important task for the manufacturers of wind turbines. A good prediction of stress level is required to tabulate the fatigue life of the rotor. Design of critical blade joints is based on such calculations. Aerodynamic loads and atmospheric turbulence have been identified as important factors in estimating fatigue damage. This report describes a stress estimate procedure and its application to the Sandia/DOE34-meter wind turbine. The procedure uses the computer code developed at IREQ (MCL) [1] for aerodynamic load calculation including atmospheric turbulence. Aerodynamic loads are decomposed into modal components and applied to structures using the finite element program NASTRAN. Rotating modes are computed as a linear composition of stationary modes. The stress distributions as functions of frequency are extracted from the modal frequency response for critical locations on the blade. Stress distributions are calculated for the first five harmonics of the rotational speed and for off-harmonic frequencies. Calculated stress amplitude spectra are compared with Malcolm's results and with test data. The results indicate that improved aerodynamic loading is obtained from MCL and that aeroelastic effects needs to be added to obtain better agreement.

Table of Contents

1. Introduction	7
Statement of work.....	8
2. Unsteady aerodynamic loads with turbulence.....	9
Interfacing the turbulence model with the MCL code	9
Modifications to MCL	13
Performance estimation with MCL	14
Aerodynamic loads with turbulence	20
3. Interfacing with NASTRAN	23
Aerodynamic loads on structural nodes	23
Details of aerodynamic input.....	25
4. Computation using NASTRAN	27
Description of the NASTRAN procedure.....	27
Parked frequencies.....	27
Rotating frequencies and eigenvectors.....	29
5. Stress calculations and their results	35
Description of the procedure	35
Modal response.....	36
Stress results	38
Comparison with results from Malcolm	50
6. Conclusions	57
7. References	59
Appendix 1.	61
Normal modes of vibration	61
Appendix 2.	67
Generalized complex eigenvectors	67
Appendix 3.	79
Aerodynamic harmonic loading	79
Appendix 4.	83
Aerodynamic modal loads applied in NASTRAN.....	83

1. Introduction

Loads on the blades of vertical axis wind turbines, including those of the Darrieus type, are cyclic due to rotation of the blade upwind and downwind, inducing an oscillation of the angle of attack relative to the blade. As this effect is related to the rotation of the rotor, the frequencies contained in the load signal occur at integer multiples of the rotational frequency. Atmospheric turbulence adds stochastic components to cyclic loads, introducing energy between each per revolution cyclic frequency. Experimental stress measurements show the cyclic nature of the response as well as the stochastic effect on the structure. With high winds, stresses on the blades induced by the aerodynamic loading exceed those produced by the inertial loads of the structure.

Several studies were conducted in the past to model atmospheric turbulence on other structures than wind turbines. NASA published a good handbook related to wind turbines in 1979 [2]. Models for spectral densities and spatial coherence in a neutral atmosphere are already well defined. The use of turbulence models to calculate unsteady aerodynamic loads on wind turbine blades is recent but justified by experimental observations that turbulence has a significant impact on the fatigue life of the structure.

Sandia National Laboratories [3] was the first to introduce turbulence models for load and stress calculation on Darrieus rotor blades. Indal Technologies [4] have used Sandia models to estimate stresses on the blades of their 6400-500Kw wind machine. Both used the double-multiple streamtube aerodynamic model to calculate aerodynamic loads. Recently, IREQ [5] introduced the local circulation model for aerodynamic load calculation. Comparisons have been made with experimental stress measurements by different authors. Agreement between measured and predicted stress data is not complete in all cases published to date, and many aspects are being questioned. Differences between results from various calculation methods can be produced by different aerodynamic models, the way in which dynamic stall is introduced, assumptions about the behavior of the turbulent flow field passing through the rotor, the random or deterministic solution used and other differences in computation methods.

Previous work has shown that it is important to introduce atmospheric turbulence to calculate stresses on the blades of wind turbines, especially if fatigue of structural components is to be evaluated. This importance is more relevant for a large-size rotor because low-frequency content of turbulence is prone to excite low-vibration modes of the structure. Furthermore, aerodynamic models used to estimate stochastic loads based on the double-multiple streamtube codes, as used by Sandia and Indal, are quasi-static and probably not completely suitable when turbulence is introduced.

Statement of work

The objective of this project was to investigate an alternative way to calculate stresses on the 34-meter Sandia/DOE Test Bed wind turbine with atmospheric turbulence included. Turbulence is introduced using Veers' [3] model. The unsteady local circulation model of IREQ (MCL) [1] was used to calculate the loads, and the structural code was also from IREQ.

The different tasks were the following:

- 1) Interface turbulence model with MCL.
- 2) Modify MCL to accept variable-chord, variable-airfoil section blades.
- 3) Calculate unsteady aerodynamic loads on the Test Bed operating in the Bushland, Texas, stochastic wind environment with a 20 m/s wind speed.
- 4) Convert the MCL-generated aerodynamic loads into a NASTRAN compatible format.
- 5) Using NASTRAN, generate a fan plot and compare these results with those previously predicted at Sandia National Laboratories.
- 6) Calculate stresses on Test Bed blade elements under the same operating conditions as in Task 3.

2. Unsteady aerodynamic loads with turbulence

Aerodynamic codes based on momentum theory are not valid for unsteady flow for the following reasons:

- wake effects are not considered because no wake model is used.
- wake crossing by the blades is not considered.
- streamtubes are assumed independent, with no interaction between the tubes.
- unsteady effects, like turbulence, are considered as a succession of static solutions.

The unsteady aerodynamic code, MCL, which IREQ developed, does not have those limitations. The wake is modeled, and the code uses a time-marching method so that the vorticity shed by the rotor blades is transported downstream by the wake. The wake downstream from the rotor contains the vorticity shed previously by the blades and induces velocities back to the blades a few moments later. This "delay" is not considered in streamtube models. The computer time required by MCL is greater than that required by the momentum codes, and it has been found more practical to make aerodynamic simulations outside stress calculations. As a first step, turbulence was introduced in MCL as described in the following section.

Interfacing the turbulence model with the MCL code

For the present project, the Kaimal spectrum as suggested by Frost [2] was used. If f is the frequency, V is the wind speed at 10 meters from the ground, h is the height, Z_o is the surface roughness coefficient, and C_1 and C_2 are constants for longitudinal and lateral directions, the spectral density is expressed as follows:

$$S(f) = \frac{C_1 \bar{v} h \left[\ln \left(\frac{10}{Z_o} + 1 \right) \ln \left(\frac{h}{Z_o} + 1 \right) \right]^{-1}}{1 + C_2 \left[\frac{hf \ln(10/Z_o + 1)}{\nabla \ln(h/Z_o + 1)} \right]^{5/3}} .$$

The values used for C_1 and C_2 are the same suggested by Frost and used by Veers and Malcolm, because no better values were known from test site atmospheric data.

Turbulence is calculated using the method published by Veers [3] and described by Malcolm [4]: This method consists of generating turbulence time series at an array of points in space upstream of the rotor, as shown in Figure 1. For each of the points in the array, the time series represents longitudinal and lateral perturbations about a mean value. Details about the time series generation are not given in this report; they are described by Veers. The present aerodynamic calculation with turbulence differs from previous work in the aerodynamic model used and, as a result, the way turbulence is introduced.

As mentioned previously, for each point in the array time series, longitudinal and lateral fluctuations are generated. We assume that those perturbations travel downstream with the general flow, as influenced by the wake-induced velocities. Inside the rotor, a linear variation is assumed, as illustrated in Figure 2.

The assumption that the perturbations are passed through the rotor with a velocity influenced by the wake is not straightforward. Velocities induced by the wake must be known inside the rotor to calculate the speed of the perturbations. The perturbations influence the general flow and the induced velocities required to locate these perturbations. One way to resolve the problem is to suppose that the perturbations move with the flow's velocity without influence from induced velocities from the wake. Since the induced velocities are an important part of the main stream flow, this assumption is not acceptable.

A better assumption was made. MCL uses a closed form solution for the wake-induced velocities as initial values to start the simulation. It has been

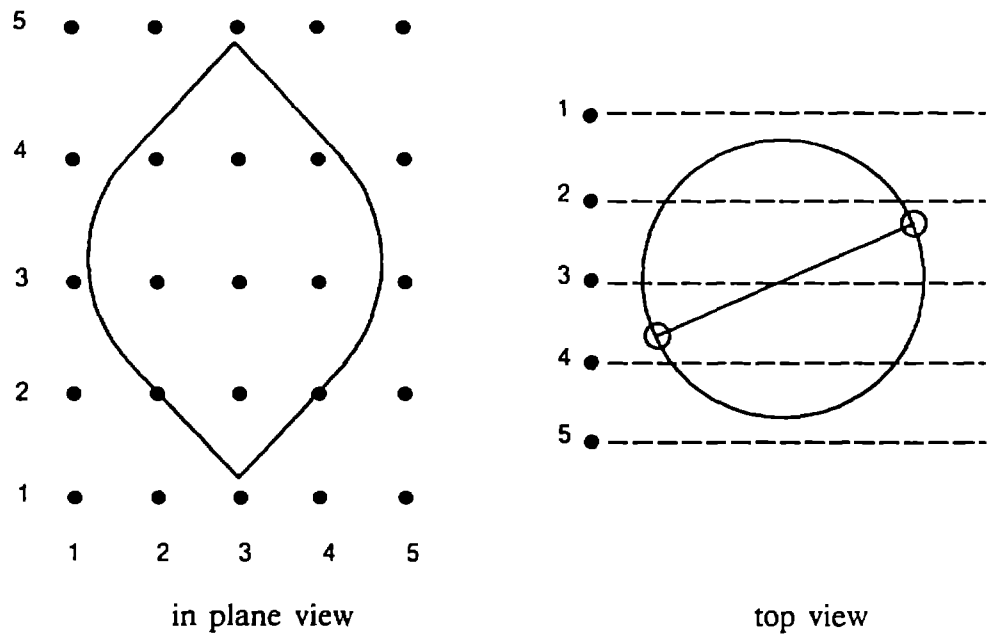


Figure 1: Example of the locations of points for wind simulation.

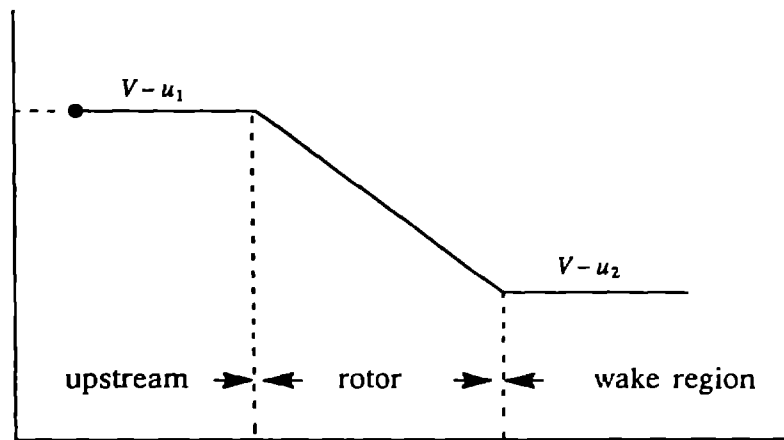


Figure 2: Wind velocity through the rotor

shown that, compared to the unsteady induced velocities, this estimation is quite accurate [1]. The assumption is that the induced velocities obtained from the closed form solution, which are as accurate as the solution from the double-multiple streamtube models, are used to calculate the positions of perturbations in the flow field. The velocity upstream of the rotor is the velocity of the uniform flow minus the velocity induced by the wake at the upstream crossing of the rotor blade trajectory. Downstream, the uniform flow field is reduced by the value of the induced velocity of the downstream rotor azimuthal crossing. Inside the rotor, a linear estimation between the two values is used.

Figure 3 shows in a schematic view the displacement of the perturbations within the rotor. Each element of the time series is moved downstream with the flow field, including induced velocities from the wake along a straight line. In this figure the rotational plane is shown for two different heights, close to the top of the rotor and close to the equator. The spacing between transverse lines shows that wind speed is larger near the top as compared to the equator. This is the effect of wind shear. The curvature of those lines is an indication of the differences in transport velocity between the center of the rotor and the edges. The flow is largely retarded in the center and almost undisturbed at the edges. This retardation is also more severe at the equator than near the top. As the blades cross this field of perturbations, the local velocity of the flow field is calculated for each blade at each time step.

The perturbations as "seen" by the blades must be evaluated at different heights and different azimuthal positions. The locations at which local velocities, including perturbations, are required do not correspond exactly to the locations where perturbations are known. Some interpolation is needed to estimate all the values required, because it is not yet possible to calculate the perturbations at every point used in the aerodynamic model. To avoid interpolation between time series of stochastic nature, along the height of the rotor, the closer series is used. The series close to the equator influences a certain zone close to the equator, and so on for different heights.

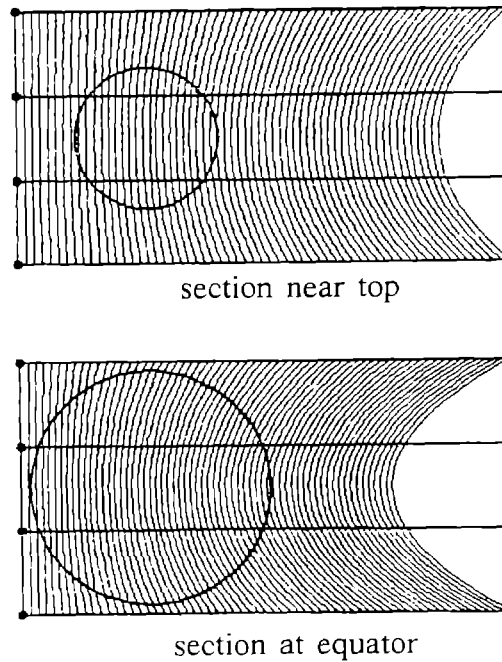


Figure 3: Schematic view of the displacement of perturbations through the rotor

In the rotational plane, the blade position is calculated, and the closest series is associated for the perturbations. This is done again to avoid interpolation between two series. The only interpolation used is within the same series to estimate the longitudinal and transverse perturbations between two points on a fine grid (see Figure 3).

Modifications to MCL

The 34-meter-diameter Darrieus vertical axis wind turbine erected near Bushland, Texas, by Sandia National Laboratories is a research-oriented machine [6 and 7]. It is a variable-chord and variable-airfoil section blade rotor. MCL has been modified to accept this special configuration. The rotor geometry and the airfoil section data were obtained from SNL [8]. The blade elements used in MCL calculations were chosen in such a way that the chord and the airfoil section are constant along the element. The edges of the elements were selected in such a way that one edge is located at the

blade/blade joints. Figure 4 shows the aerodynamic element configuration used for the present project. In the computer code, the elements are numbered to take into account the blade chord and the associated airfoil section used in the aerodynamic calculation.

Performance estimation with MCL

In order to verify the variable-chord and the variable-airfoil section version of MCL, performance calculations for the SNL 34-meter turbine at 28 and 34 rpm were done. The results are presented in Figure 5, where MCL is compared to SLICEIT from SNL and experimental data from the 34-meter Test Bed. As shown in Figure 5, the results obtained with MCL differ from those calculated with SLICEIT, which is a double-multiple streamtube code using the same airfoil data and a very similar dynamic stall model. The calculation with MCL agrees well with measured data.

The question is then to explain the difference between MCL's local circulation model results and those from the double-multiple streamtube code SLICEIT. The difference is both for high winds, as shown in Figure 5, and for the low wind, as seen using the C_p curves of Figure 6. For high winds, the local circulation model predicts a higher power than the double-multiple streamtube code. The agreement with experimental data is good at 34 rpm, but power is overestimated at 28 rpm. In this range of wind speed, the blades operate in the dynamic stall regime, and dynamic stall models need further development. The double-multiple streamtube model underestimates power at both rotational speeds, the under-prediction being more severe at 34 rpm. For low winds, Figure 6 shows that both codes overestimate the performance at both rotational turbine speeds, the overestimation being less severe for MCL. This behavior indicates that rotor drag is larger than that estimated from airfoil data. This seems to be confirmed by Berg [9 and 10]; better fairings of blade-blade joints should improve performance of the turbine in low winds.

To verify that the modified version of MCL gives proper results and that its comparison with SLICEIT in the previous figures is valid, previous calculations using the local circulation method [1] are presented in Figures 7-9. Figure 7 shows the power curve of the Sandia 17-meter wind turbine. For high winds, the comparison between the two prediction methods gives a

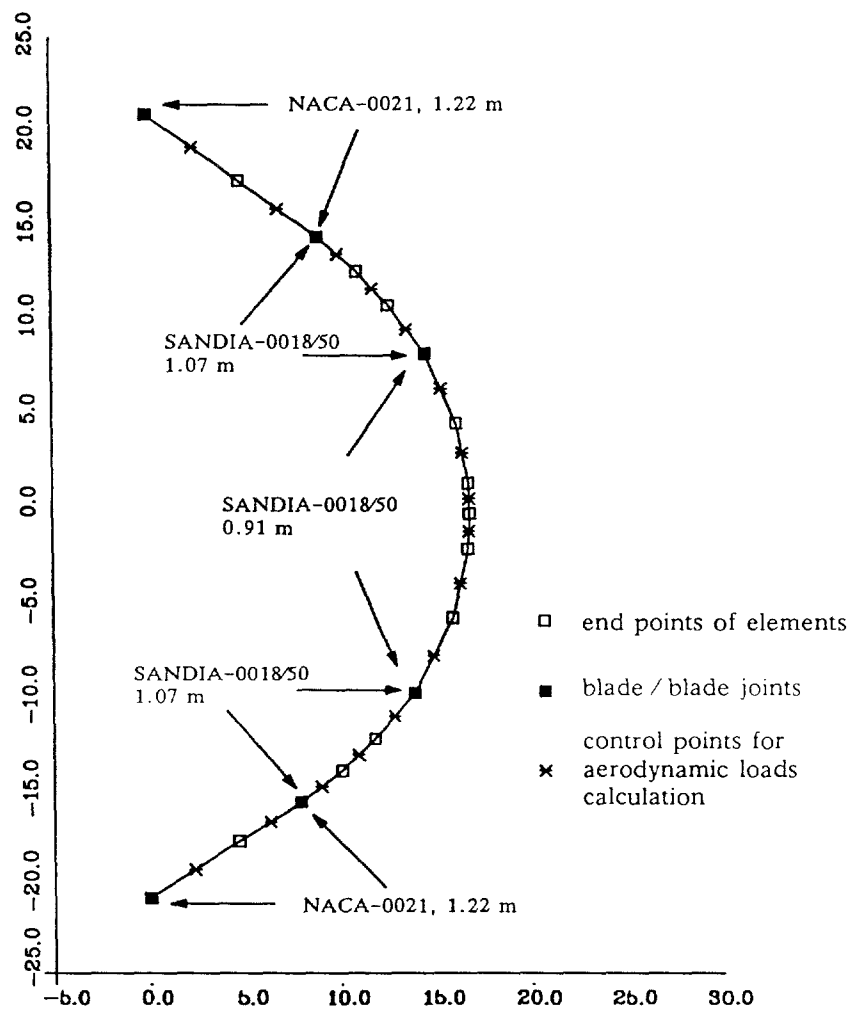


Figure 4: Aerodynamic elements

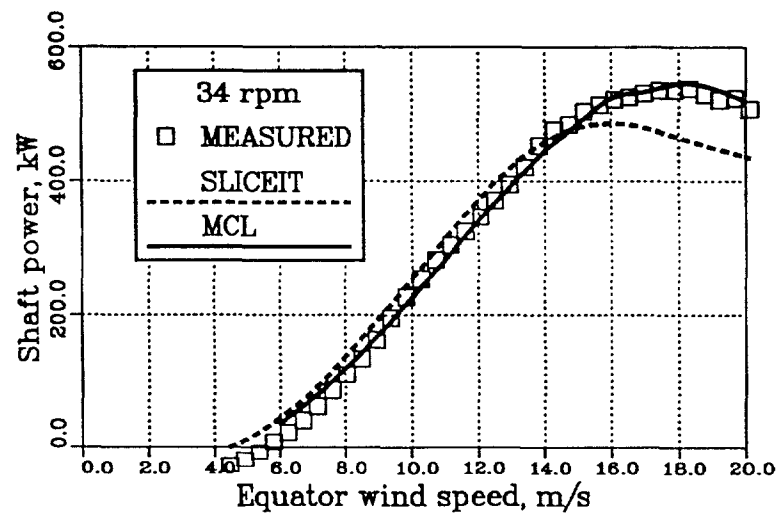
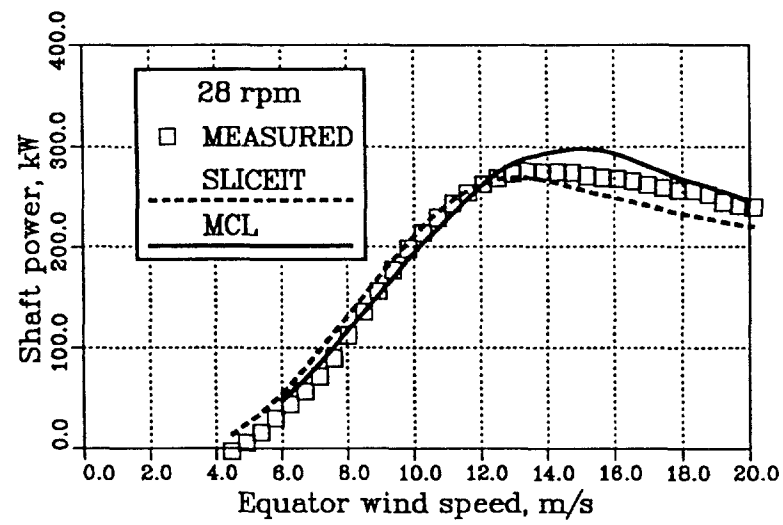


Figure 5: Performance of Sandia's 34-m Test Bed

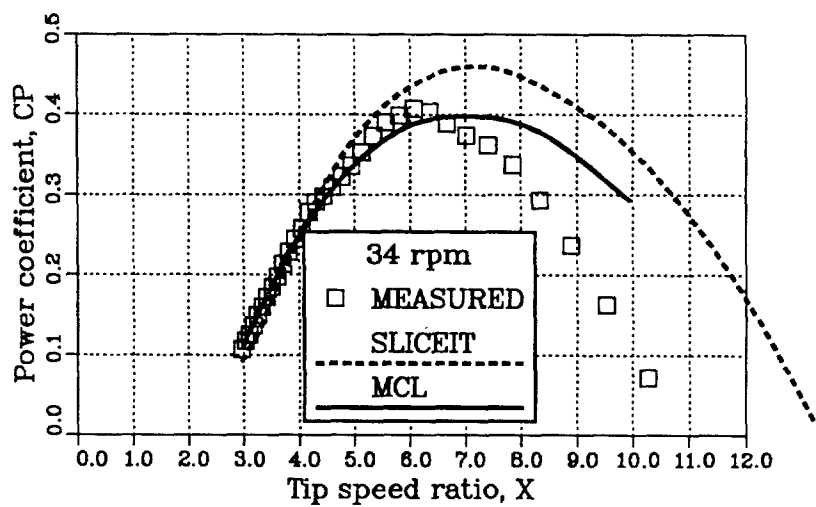
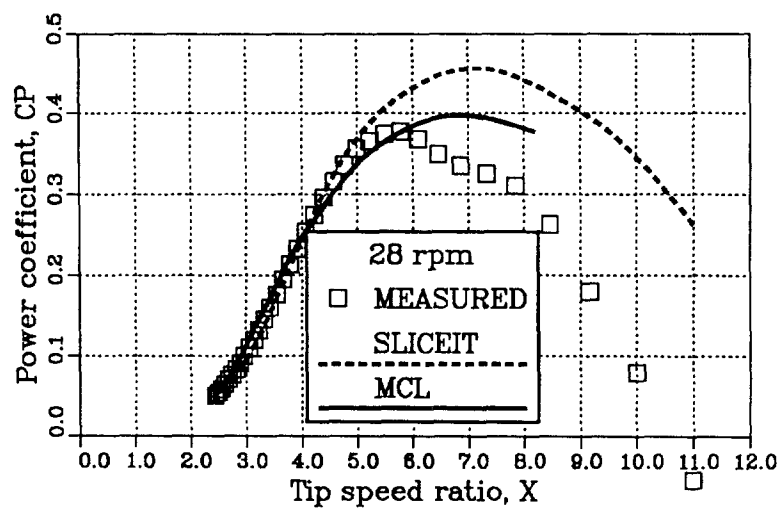


Figure 6: Performance of Sandia's 34-m Test Bed

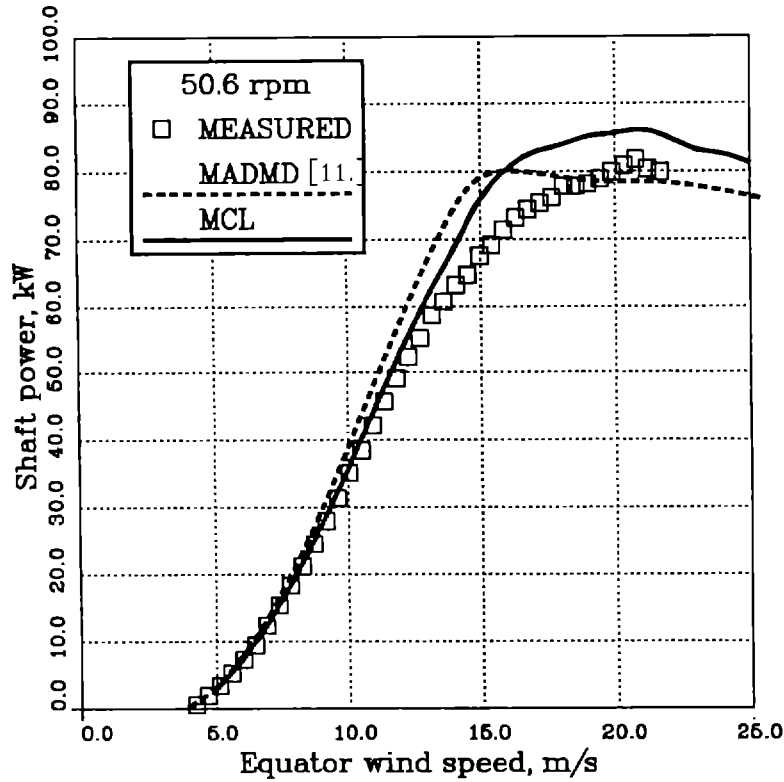


Figure 7: Performance of Sandia's 17-m turbine

result very similar to that obtained on the 34-meter turbine. MCL estimates a higher power than the double-multiple streamtube model for high wind with the same dynamic stall model. In the medium-wind range, MCL is closer to experimental data. A comparison between Figures 5 and 7 shows the same type of differences between the two methods.

To be sure that differences observed between the two codes are not related to dynamic stall models for high winds, the K_p curve for the 17-meter turbine is calculated with both codes without dynamic stall, and the results are presented with experimental data in Figure 8. The corresponding C_p curve is shown in Figure 9. The same difference is observed between the two curves; the maximum power is higher using the local circulation model for high winds and lower in the medium-wind range. Figure 9 shows that lower performance

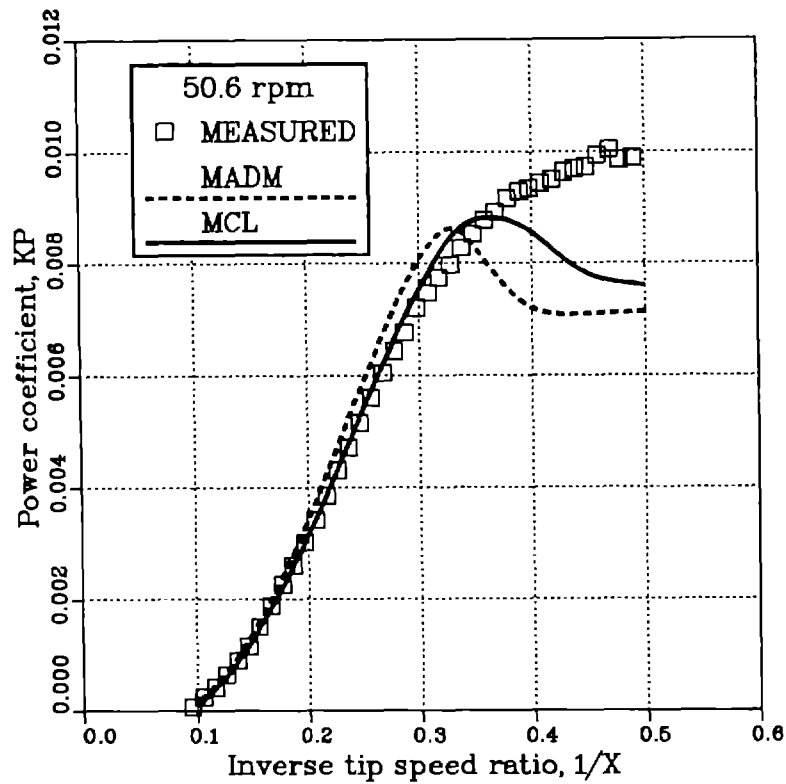


Figure 8: Performance of Sandia's 17-m turbine
(without dynamic stall prediction model)

at low wind is predicted with MCL, as observed on the 34-meter turbine. Calculations of performance for both the 17 and 34-meter turbines give similar results, which tend to confirm the reliability of the modified version of MCL. These calculations confirm also that the difference between the two models comes from specific calculation of the velocities induced by the wake. The difference between the two aerodynamic models is related to differences in the approach. From the results obtained for both the 17 and 34-meter turbines, confidence in the local circulation code, MCL, has been established,

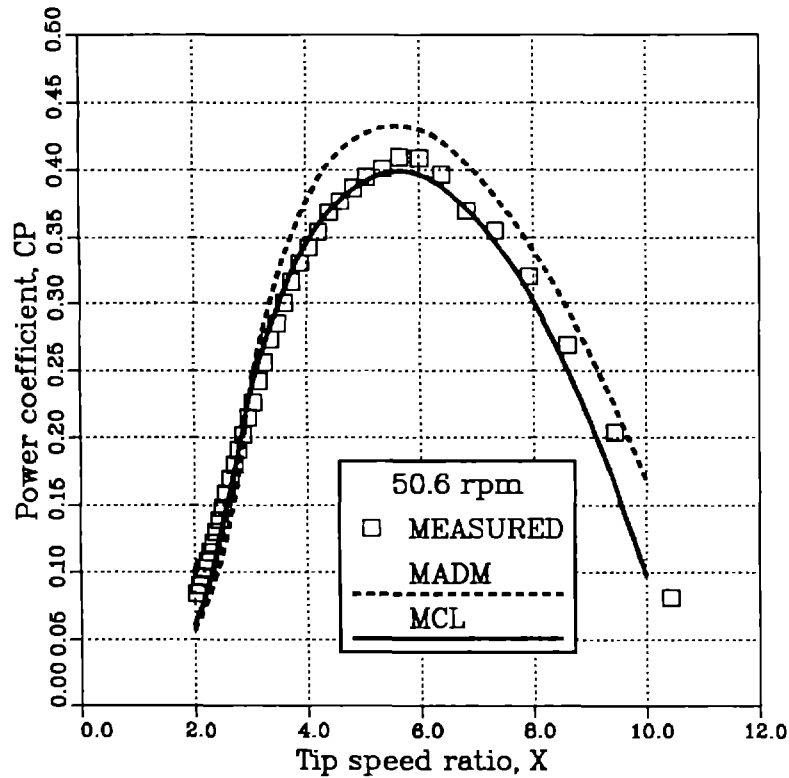


Figure 9: Performance of Sandia's 17-m turbine
(without dynamic stall prediction model)

Aerodynamic loads with turbulence

With the modifications discussed above, unsteady aerodynamic code MCL is used for a turbulent flow field to estimate the unsteady aerodynamic loads applied at different locations along the blades. As stated above, turbulence, being considered as local velocity perturbations, is introduced in the load calculation as a modification of the angle of attack and the relative wind velocity. The corresponding changes of vorticity in the wake are kept from one time step too the other, and introduce a delay in the induced effects.

Figure 10 represents the spectra for the normal and the tangential forces at the equatorial position along the blade of the 34-meter turbine. This curve contains 106 frequencies between 0 and 4 hertz. Loads at harmonic frequencies are clearly seen on each curve. The 10% turbulence level used in this simulation gives off-harmonic frequencies as expected. The spectra show the amplitude of the loads, but in the structural calculation real and imaginary parts are used to take into account the phase of these loads.

Direct validation of aerodynamic loads is not feasible. The response of the rotor under the action of such aerodynamic loading is the only means of evaluation. If computed stresses compare with measured values, one can assume that aerodynamic input is valid. The following sections of this report describe how calculated aerodynamic loads are translated into modal loads and are used to calculate unsteady stresses for critical blade locations.

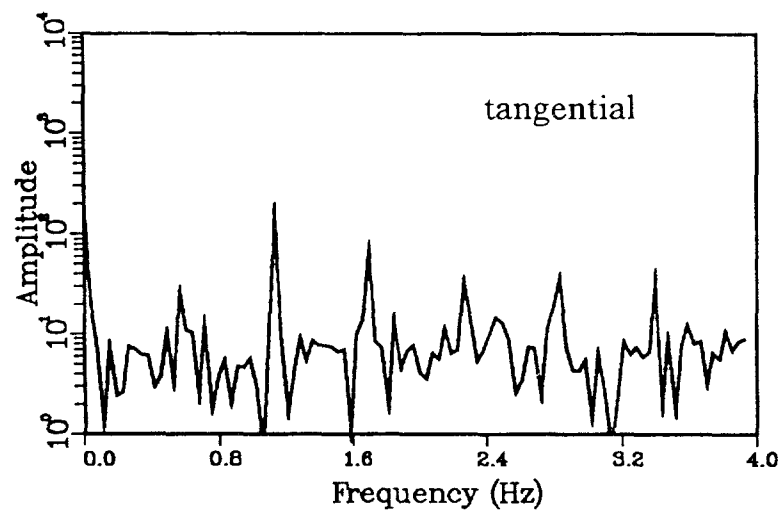
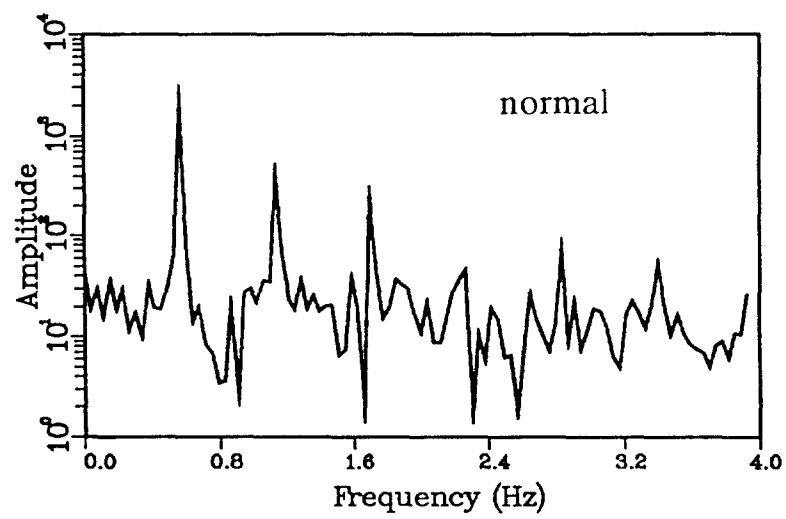


Figure 10: Aerodynamic loads at equator (N/m)
(34-meter turbine, 34 rpm, 10% turbulence)

3. Interfacing with NASTRAN

To introduce unsteady aerodynamic loads as input for NASTRAN, the time series are first transformed into the frequency domain and are then used for the solution at each frequency. This type of interface allows the user to select an arbitrary number of revolutions of aerodynamic simulation and it still gives the possibility of solving for a constant number of frequencies in the structural calculation. A Fourier transform of each load time series is performed for the frequency range of interest. The loads are then introduced in NASTRAN on each node of the blades.

Aerodynamic loads on structural nodes

A computer program has been developed to read the node coordinates where aerodynamic loads are applied and to convert from aerodynamic elements to structural elements. MCL utilizes 16 nodes, as shown in Figure 11, and these are more concentrated close to the equator, the loads being larger in this area. For structural calculation, the blade is modeled using 44 nodes concentrated close to the roots and the blade-blade joints.

The aerodynamic loads at the structural nodes used by NASTRAN are obtained using cubic spine interpolation between loads calculated by MCL at aerodynamic nodes. This is done at each frequency of interest. The aerodynamic input consists of real and imaginary components of the normal and tangential loads for each aerodynamic node for the two blades. The translation program converts the loads to structural nodes in the system of coordinates used in NASTRAN.

Interpolation to determine loads between the aerodynamic nodes is not the ideal situation because of stochastic content of the loads, but it allows the use of more complex aerodynamic simulations. A simulation for each structural node would require a large amount of computer time. The main component of the load is periodic, and the stochastic components represent fluctuations of a few percent about the main load. If close to a resonance, these small perturbations will produce significant fluctuation of stresses. Interpolation,

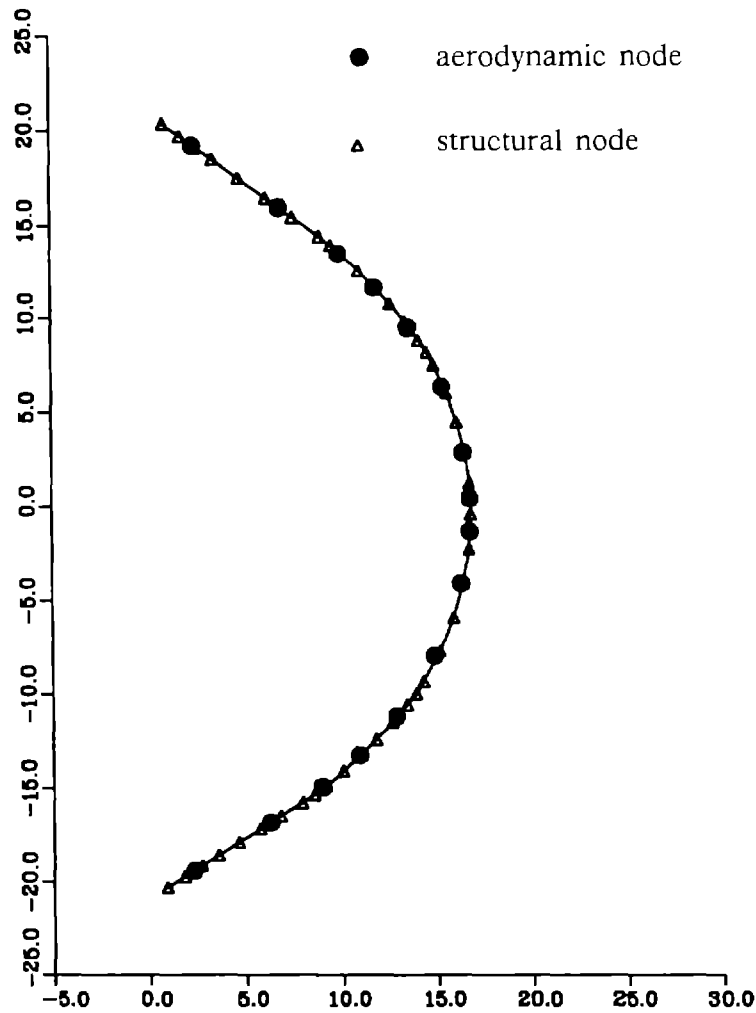


Figure 11: Aerodynamic and structural nodes

with nodes being distributed as in Figure 11 is probably a good approximation.

Any aerodynamic computer code can be used with the present approach. The only requirement is that the loads, in the frequency domain, be given for certain nodes along the blade in the format required by the interface computer code. Computer time required to generate the loads does not influence the structural solution. This gives the possibility of integrating

different aerodynamic loads from different codes and of modeling the structure as accurately as required at critical locations. This approach also permits using exactly the same nodes for both aerodynamics and structure.

Details of aerodynamic input

Figure 11 shows the location of the aerodynamic and structural nodes. Loads used for interpolation are per unit of blade length in the normal (or radial) and tangential directions. The interface program calculates interpolated loads for structural nodes, the blade length on which they are applied and their projections in the coordinate system (X,Y,Z) for the structure.

These projections are input into NASTRAN using "DAREA" cards; the interpolated loads are input using "TABLED1" cards. To limit the size of load data, loads are introduced in the frequency domain using a given number of frequencies in a given range. The interface program generates the NASTRAN input file required for calculations with the following information:

For each structural node N:

- Two DAREA cards: one gives projections in the rotor plane, (X,Z) of the blade length (L_x , L_z) relevant to the node (Figure 12) and the other gives L_y , which is the length on which out of plane loads are applied.
- Four TABLED1 cards: for each frequency, they give the real and imaginary parts of normal and tangential loads relative to the blade. These loads are forces per unit length with the same sign convention as for the aerodynamic code. The first two cards refer to the first DAREA card that gives L_x and L_z , and the two next cards refer to the second DAREA card that gives L_y .

With this information, NASTRAN automatically generates F_x , F_y , and F_z , the loads applied to the node N of the structure. The sign convention between aerodynamic and structural codes is taken into account in the DAREA cards. In the example in Figure 12, the fluid flow program gives a normal positive load along vector n , in NASTRAN L_x will be positive and L_z negative.

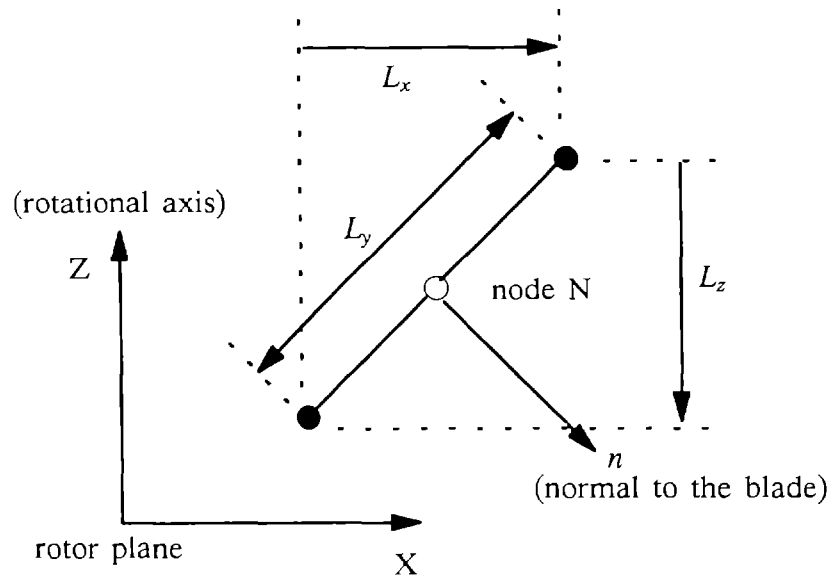


Figure 12: Structural element projections

For the whole structure:

- One RLOAD1 card combines the DAREA cards and a FREQ1 card, which gives the sequence of frequencies to be analyzed.

The aerodynamic-structure interface program is a convenient tool for incorporating elaborate aerodynamic simulations into a structural computation without a reduction in the number of structural nodes. It automatically generates the NASTRAN input for applied loads. This approach permits using any aerodynamic code without sacrificing on the structural model because of computer time constraints.

4. Computation using NASTRAN

A structural model of the SNL 34-meter wind turbine was obtained from Sandia. The first task was to verify the model by calculating the Campbell diagram (fan plot). The procedure used was developed at IREQ and was already checked against the Sandia approach using the Magdalen Island wind turbine [12].

Description of the NASTRAN procedure

Work is done in two parts:

- The non-linear stiffness matrix, the Coriolis and the softening matrices are calculated using solution 64 of NASTRAN, modified by a DMAP code developed at IREQ.
- Modes and frequencies are evaluated using solution 70 of NASTRAN assuming that the non-linear stiffness matrix is proportional to the square of the rotational velocity. This work requires a DMAP code to modify solution 70.

Parked frequencies

To compute the zero rpm frequencies, the "bulk deck" from Sandia was used with an analysis set including all the column and blade GRID points but retaining only the first three translational degrees of freedom as master degrees of freedom to be used in the Guyan reduction technique. Table 1 shows a comparison with Sandia's analytical calculation and experimental measurements. IREQ calculations underestimate the frequencies as compared to Sandia data, both analytical and measured. This is probably because IREQ's procedure uses a concentrated mass approach, which tends to underestimate the natural frequencies of the structure. To compute parked frequencies, the rotation around the "Z" axis at GRID point 1 (bottom of the column) has been blocked, bringing the first propeller mode (1Pr) to 1.6 Hz.

This assumes an infinite stiffness of the drive train when the rotor is parked, which is not necessarily the case in reality.

The principal difference between experimental and numerical calculations is for the first BE mode. This disagreement is certainly related to small differences between the finite element model and the real structure.

Table 1: Frequencies at 0 rpm

Mode	IREQ calculated	Sandia calculated	Sandia measured	IREQ deviation	Sandia deviation
1FA	1.05	1.05	1.06	1.0%	1.0%
1FS	1.05	1.05	1.06	1.0%	1.0%
1Pr	1.60	1.56	1.52	5.2%	2.6%
1BE	1.70	1.72	1.81	6.4%	5.2%
2FA	2.05	2.07	2.06	0.7%	0.5%
2FS	2.12	2.14	2.16	1.9%	1.0%
1TI	2.42	2.46	2.50	3.2%	1.6%
1TO	2.55	2.58	2.61	2%	1.2%

Mode Shape Abbreviations	
1FA	First Flatwise Antisymmetric
1FS	First Flatwise Symmetric
1Pr	First Propeller
1BE	First Blade Edgewise
2FA	Second Flatwise Antisymmetric
2FS	Second Flatwise Symmetric
1TI	First Tower In-Plane
1TO	First Tower Out-of-Plane

Rotating frequencies and eigenvectors

Figure 13 shows the Campbell diagram for the SNL 34-meter turbine, calculated using the approach described above. Frequencies obtained at 0 rpm agree with those obtained in the analysis of the parked rotor except for the first propeller mode. This is a rigid body mode restrained at the lower end by a soft spring.

Between 1 and 2 Hz, three modes are dominant: 1FA, 1FS and 1BE. Analysis has shown that the symmetric mode, 1FS, is uncoupled to the two others, which are antisymmetric. *Below 40 rpm*, the second complex eigenvector computed by NASTRAN has a real part from the 1FA mode and an imaginary part from the 1BE mode. The fourth complex eigenvector is similar to the first except that the real part comes from the 1BE mode and the imaginary part is from the 1FA. *Above 40 rpm*, the second complex eigenvector has a real part from the 1BE mode and the imaginary from a combination of the 1FA and the 1TI modes. The contribution of the former is 33.7% and the contribution of the latter is 61.2% at 46 rpm. The fourth complex eigenvector then has its real part from the 1FA mode and its small imaginary part (16%) from the 1BE mode. This means that the two modes (1FA and 1BE) are coupled when the turbine rotates, and this coupling is stronger close to 40 rpm. Nevertheless, the frequencies of the second and fourth eigenvectors never take the same value; the modes do not cross over. In order to check this point, a computation at each 5 rpm was done. The frequencies computed in this range agree with those in Figure 2 of Ashwill and Veers [13].

In the 2-3 Hz range, the complex eigenvectors 5, 6, 7 and 8 are found. *Eigenvector 6* has a strongly dominant real part coming from the 2FS mode, weakly coupled by the imaginary part to the 12th natural mode, 3Pr. This eigenvector does not couple to the three others (5, 7 and 8). Compared with Sandia's analytical results, the eigenfrequencies are slightly lower, but the agreement is acceptable. *Eigenvectors 5, 7 and 8* are coupled together. Above 20 rpm, eigenvector 7 has a real part, most of it from 2FA and a little from 1TI, and an imaginary part, most of it from 1TO, which decreases as the rpm increases. Below 20 rpm, the real part is mainly from 1TI, with a weak contribution from 2FA. This behavior explains the crossover shown in Sandia's fan-plot between 20 and 30 rpm. Eigenvector 5 shows that 2FA is

dominant over the range of rpm, with a contribution from 1TI increasing with the angular speed of the rotor. No crossover is observed in the range considered. The following three tables (2,3 and 4) give complex eigenvectors 5, 6, 7 and 8 computed at 16, 21 and 26 rpm. Agreement with Sandia computations is good.

Table 2: Eigenvectors at 16 rpm

#	Real part	Imaginary part
5	$-0.3 \times 1\text{TI} + 1.0 \times 2\text{FA}$	$-0.36 \times 1\text{TO}$
6	$1.0 \times 2\text{FS}$	
7	$1.0 \times 1\text{TI} + 0.63 \times 2\text{FA}$	$0.62 \times 1\text{TO}$
8	$1.0 \times 1\text{TO}$	$0.73 \times 1\text{TI} - 0.18 \times 2\text{FA}$

Table 3: Eigenvectors at 21 rpm

#	Real part	Imaginary part
5	$-0.51 \times 1\text{TI} + 1.0 \times 2\text{FA}$	$-0.57 \times 1\text{TO}$
6	$1.0 \times 2\text{FS}$	$-0.1 \times 12^{\text{th}} \text{ mode}$
7	$0.96 \times 1\text{TI} + 1.0 \times 2\text{FA}$	$0.6 \times 1\text{TO} + 0.33 \times 1\text{BE}$
8	$0.15 \times \text{BE} + 1.0 \times 1\text{TO}$	$0.21 \times 2\text{FA} - 0.8 \times 1\text{TI}$

Table 4: Eigenvectors at 26 rpm

#	Real part	Imaginary part
5	$-0.67 \times 1\text{TI} + 1.0 \times 2\text{FA}$	$-0.76 \times 1\text{TO} - 0.56 \times 1\text{BE}$
6	$1.0 \times 2\text{FS}$	$-0.14 \times 12^{\text{th}} \text{ mode}$
7	$0.72 \times 1\text{TI} + 1.0 \times 2\text{FA}$	$0.44 \times 1\text{TO} + 0.29 \times 1\text{BE}$
8	$1.0 \times 1\text{TO} - 0.17 \times 1\text{BE}$	$0.84 \times 2\text{TI} - 0.23 \times 1\text{FA}$

For the range between 3.5 and 5 Hz, overall behavior agrees with Sandia computations except that one more mode is predicted at 3.43 Hz for the stationary rotor (Fig. 13). Frequencies of the modes in this range being above 5p excitation, no investigation was done in this area. Agreement with Sandia computations is good.

The following table is a comparison of the twenty first frequencies computed at Sandia and IREQ at 30 rpm. The results show a maximum deviation of 5% at 8 Hz and confirm that geometric and Coriolis effects are properly introduced.

Table 5: Frequencies and mode shapes at 30 rpm

Complex eigenvectors			Frequencies		
Order	Real part	Imag. part	IREQ	Sandia	Difference
1	1PR	–	0.23	0.23	0%
2	1FA	–	1.32	1.31	0.8%
3	1FS	–	1.33	1.32	0.8%
4	1BE, 1TO	1TI, 1FA	1.61	1.61	0%
5	2FA, +1TI	1TO, 1BE	2.06	2.06	0%
6	2FS	3PR	2.51	2.51	0%
7	2FA, –1TI	1TO, 1BE	2.59	2.59	0%
8	1TO, 1BE	1TI, 2FA	2.92	2.92	0%
9	2PR	3FS, 1FS	3.60	3.62	0.6%
10	2BE, –2TO	2TI	3.69	3.69	0%
11	3FA, 2TI	2BE, 2TO	3.90	3.94	1.0%
12	3FS, 2FS	3PR, 2PR	4.00	4.04	1.0%
13	3PR	3FS, 2FS	4.03	4.09	1.5%
14	2BE, +2TO	3FA, 2TI	4.20	4.22	0.5%
15	2TO, 2BE	2TI	4.71	4.72	0.2%
16	4FS	–	5.64	5.80	2.8%
17	4FA	–	5.72	5.87	2.6%
18	3BE	–	7.86	7.99	1.6%
19	5FA	–	7.97	8.42	5.3%
20	5FS	–	8.03	8.48	5.3%

5. Stress calculations and their results

Stress computation is done directly in NASTRAN using the same procedure as described in Section 4 for modes and frequencies. Aerodynamic loads are obtained from the aerodynamic-structure interface and they are superimposed on the static loads. The first step is done using the modified solution 64 and the second step with solution 71, modal frequency response.

Description of the procedure

In the modal form, the equation to be solved is the following:

$$\Phi^t M \Phi \ddot{q} + 2\Omega \Phi^t C \Phi \dot{q} + [\Phi^t K \Phi + \Omega^2 \Phi^t (KG - S) \Phi] q = \Phi^t F$$

where:

- $\Phi^t M \Phi = I$, identity matrix, dimension p where p is the number of modes used for the analyses.
- $\Phi^t C \Phi = C^*$, reduced Coriolis matrix, dimension $p \times p$.
- $\Phi^t K \Phi = \Lambda$, diagonal matrix for the natural frequencies, dimension $p \times p$.
- $\Phi^t (KG - S) \Phi = K^*$, non-linear reduced stiffness matrix, dimension $p \times p$.
- Φ , p first natural modes of the structure at zero rpm.
- $\Phi^t F = F^*$, modal loads, dimension $p \times n$, where n is the number of frequencies retained at the aerodynamic load generation step.

The solution q of this equation is the modal response with a dimension identical to the dimension of the modal loads ($p \times n$). The modal loads

represent the aerodynamic force contribution for each of the natural modes. The equation $x = \Phi q$ gives the displacements.

The above equation was solved using solution 71 of NASTRAN without using the random module. The results were obtained with only one simulation per case of turbulence. Several additional simulations would be required to decrease relative errors of estimated spectra.

Modal response

Table 6: Eigenfrequencies and eigenvectors at 34 rpm in the frequency range of the aerodynamic loads.

Eigenvector				r = Excitation freq. / Eigenfreq.				
Order	Frequency	Real part	Imaginary part	1P	2P	3P	4P	5P
1	0.23	1×1PR			4.93			
2	1.38	1×1FA	.14×1BE	0.41		1.23		
3	1.39	1×1FS			0.815		1.63	
4	1.58	.26×1TO + 1×1BE +.2×2FA	.24×1FA +.43×1TI	0.358		1.074		1.79
5	2.05	.93×1TO + 1×1BE	-.76×1TI -.94×2FA	0.276		0.828		1.38
6	2.59	1×2FS			0.437		0.875	
7	2.67	1×2FA -.56×1TI	.34×1TO -.24×1BE	0.212		0.636		1.06

Table 6 shows the frequencies and the eigenvectors in the excitation range of the aerodynamic loads, from 1P to 5P.

The right part of the table shows the ratio of the excitation frequency to the natural frequency, called factor r , for each of the eigenvectors. A value close to 1.0 represents a condition close to resonance where the response of the structure is very sensitive to the amount of damping. This condition is met for eigenvectors 7 and 4. In the first case, operation of the turbine is close to a 5P crossing, and close to a 3P crossing in the second case. The former is characterized by induced flatwise stresses coming from excitation of the 2FA mode at 5P. Due to the proximity of the eigenfrequency, a response is expected at this frequency in addition to the 5P response because of wind turbulence excitation. The 3P crossing with eigenvector 4, at 1.58 Hz, induces both flatwise and edgewise stresses due to coupling in-plane modes (1FA, 2FA, and 1TI) with out-of-plane modes (1BE and 1TO). A response is also expected at eigenfrequencies of 1.38 Hz and 2.05 Hz.

Modal loads presented in the following table (Table 7), show, for various natural modes, the magnitudes of aerodynamic loads at harmonic frequencies. Symmetric modes are excited by even harmonics and antisymmetric modes by odd harmonics of loading. Modal loading is described in more detail in Appendixes 3 and 4.

Table 7: Modal Loads at harmonic frequencies (in/s²).

Mode	Load amplitudes (34 rpm)				
	1P	2P	3P	4P	5P
1PR		290.		55.	
1FA	175.		75.		20.
1FS		145.		40.	
1BE	95.		190.		80.
2FA	88.		32.		38.
2FS		124.		48.	
1TI	960.		120.		40.
1TO	10.		48.		28.
3FA	142.		25.		
2PR		18.		13.	
3FS		62.		18.	
3PR		128.		36.	
2BE	34.		43.		14.
2TI	130.		16.		
2TO	13.		9.		
4FS		145.			
4FA	250.		50.		
5FS		22.			
3BE	42.		36.		13.

Stress results

The following tables show stress results for element 104 of NASTRAN, located at the upper root-blade connection, computed at 10% and 30% turbulence levels, with and without 2% structural damping. Computed stresses are compared at harmonic and off-harmonic frequencies with experimental stresses measured by Sandia on the 34-meter Test Bed.

**Table 8: Harmonic stresses in MPa at 34 rpm
in a 15.6 m/s wind (upper root)**

	<i>10% turb. 2% mod. da. 0% str. da.</i>		<i>10% turb. 2% mod. da. 2% str. da.</i>		<i>30% turb. 2% mod. da. 0% str. da.</i>		<i>30% turb. 2% mod. da. 2% str. da.</i>		<i>Sandia experimental data [13.]</i>	
Freq.	Flat wise	Lead -Lag	Flat wise	Lead -Lag	Flat wise	Lead -Lag	Flat wise	Lead -Lag	Flat wise	Lead -Lag
1P	1.54	2.50	1.54	2.51	1.46	2.52	1.46	2.53	2.20	1.48
2P	7.60	1.20	7.56	1.20	6.17	0.70	6.14	0.70	4.17	0.89
3P	2.33	1.36	2.33	1.40	1.43	0.44	1.48	0.43	1.51	1.55
4P	1.13	0.48	1.14	0.48	0.79	0.71	0.77	0.72	0.86	0.24
5P	2.51	1.33	2.46	1.29	1.93	0.29	1.92	0.29	0.40	0.29

**Table 9: Off-Harmonic stresses in MPa at 34 rpm
in a 15.6 m/s wind (upper root)**

	<i>10% turb. 2% mod. da. 0% str. da.</i>		<i>10% turb. 2% mod. da. 2% str. da.</i>		<i>30% turb. 2% mod. da. 0% str. da.</i>		<i>30% turb. 2% mod. da. 2% str. da.</i>		<i>Sandia experimental data [13.]</i>	
Freq.	Flat wise	Lead -Lag	Flat wise	Lead -Lag	Flat wise	Lead -Lag	Flat wise	Lead -Lag	Flat wise	Lead -Lag
1.28	2.20		2.14		6.30		6.12		1.70	
1.39	6.17	2.30	4.00	1.39	13.70	4.38	8.94	2.70	1.34	0.46
1.51	1.28		1.24		3.20	3.10	0.55		0.55	
1.55		2.10		1.62		6.40		5.00		0.51
1.62		1.82		1.58		3.62		3.20		1.09
2.04		1.26		1.00		1.85		1.46		0.94
2.56	1.20		0.92		3.37		2.75		0.78	
2.68	1.97		1.55		3.20		2.70		0.46	

For *harmonic stresses*, damping has little effect. The effect of increasing turbulence level is a reduction of harmonic stresses with the exception of the lead-lag stress at 4P where an increase is observed. The flatwise stress reduction and the lead-lag stress at 1P, which is essentially unchanged, is greater at 2P, 3P, 4P, and 5P than for 1P. The general tendency of the computations as compared with measured values is to overestimate the stresses, except at 1P, where they are underestimated. Flatwise stresses at 2P are overestimated because of a close resonance condition ($r=0.815$) of the 1FS mode.

Experimental data show a strong response at this frequency, but not as high as computed. The 1FS mode is probably highly damped by the aeroelastic damping because of the flatwise motion. However, a reduction from 7.6 MPa to 4.17 MPa (see Table 8) cannot be produced by aeroelastic damping only, a value of 30% of critical damping is required to produce that reduction. The difference may come from the averaging process used during experimental measurement, which is different from the deterministic approach used for computations. Another source of discrepancies may be an overestimation of the 2P contribution for the 1FS mode in the modal loads, too much energy being distributed for this mode at that frequency. The overestimation at 5P, in both flatwise and lead-lag stresses, is due to a near resonance condition ($r=1.06$) for eigenvector 7. At this frequency, the coupling between 2FA, mixed with 1TI, and 1BE mixed with 1TO, induces both lead-lag and flatwise stresses. Aerodynamic damping would reduce the overestimation by damping in-plane modes, but not enough to bring computed values in the range of measured data.

From Table 9, showing *off-harmonic stresses*, it can be seen that stresses are overestimated compared with measured values, very sensitive to damping and strongly correlated with the turbulence level, increasing rapidly as turbulence varies from 10% to 30%. The 10% case is closer to Sandia measurements. Turbulence excites resonances that are sensitive to damping. An aeroelastic model would damp flatwise resonances, improving off-harmonic stresses estimation.

Figures 14 to 21 show stress amplitude spectra obtained with the present calculation procedure and compare them with measured stress spectra. The calculated data are shown below the experimental data for each of the figures. The first set of results (Figs. 14 to 17) has been obtained with 2% modal damping and no structural damping, whereas the second set of results (Figs. 18 to 21) was calculated using 2% structural damping.

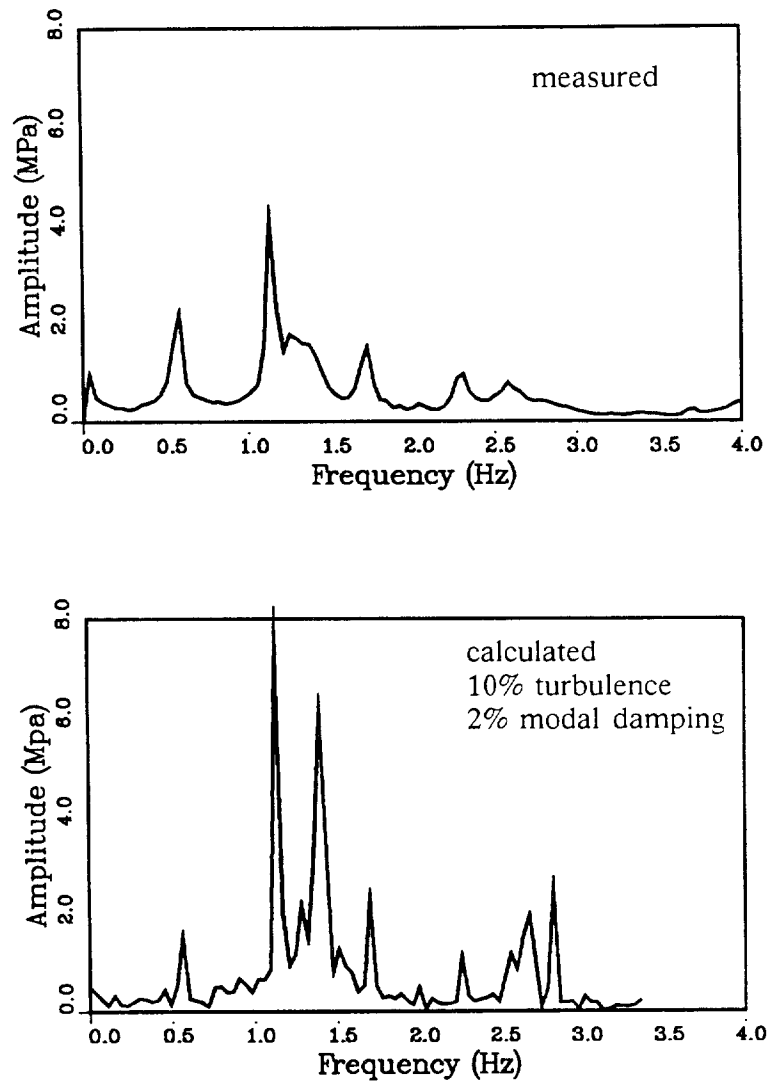


Figure 14: Amplitude spectra of flatwise stress response at 34 rpm, 15.6 m/s wind.

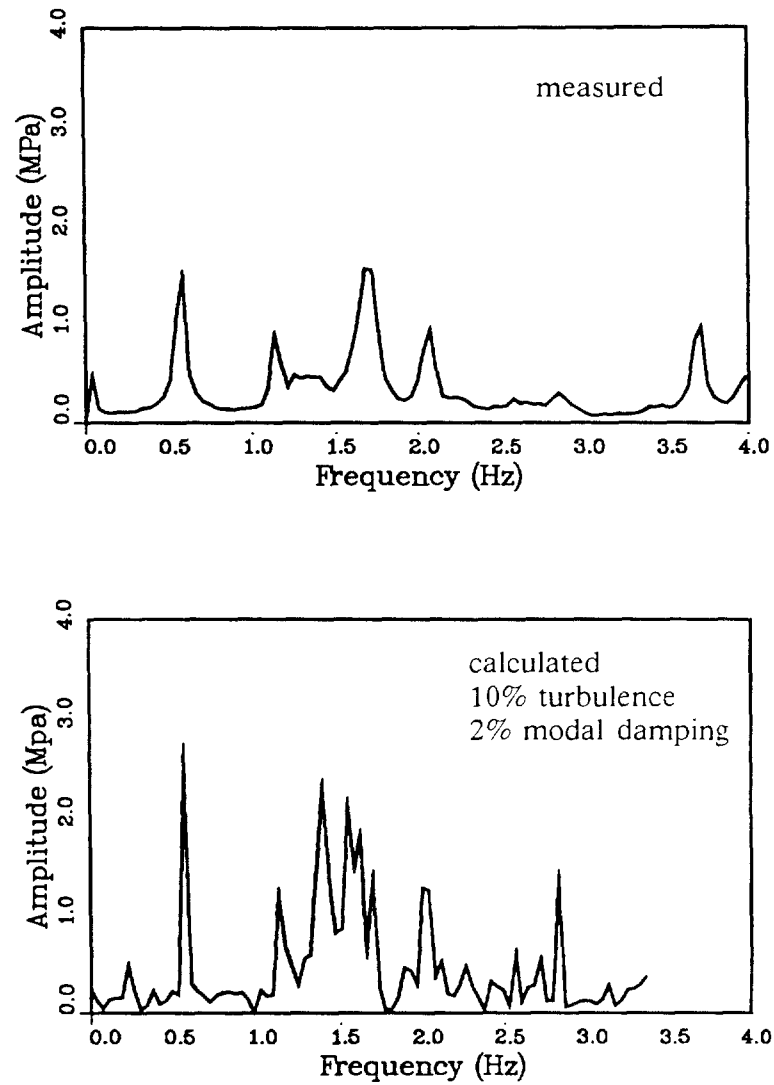


Figure 15: Amplitude spectra of lead-lag stress response at 34 rpm, 15.6 m/s wind.

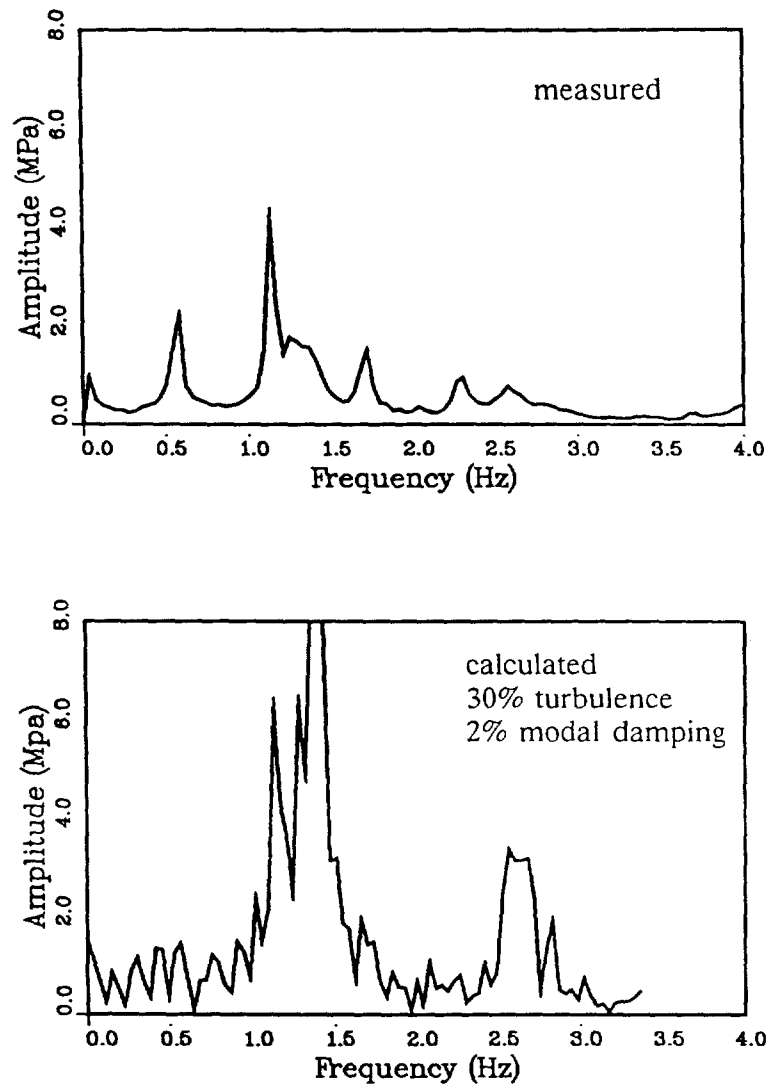


Figure 16: Amplitude spectra of flatwise stress response at 34 rpm, 15.6 m/s wind.

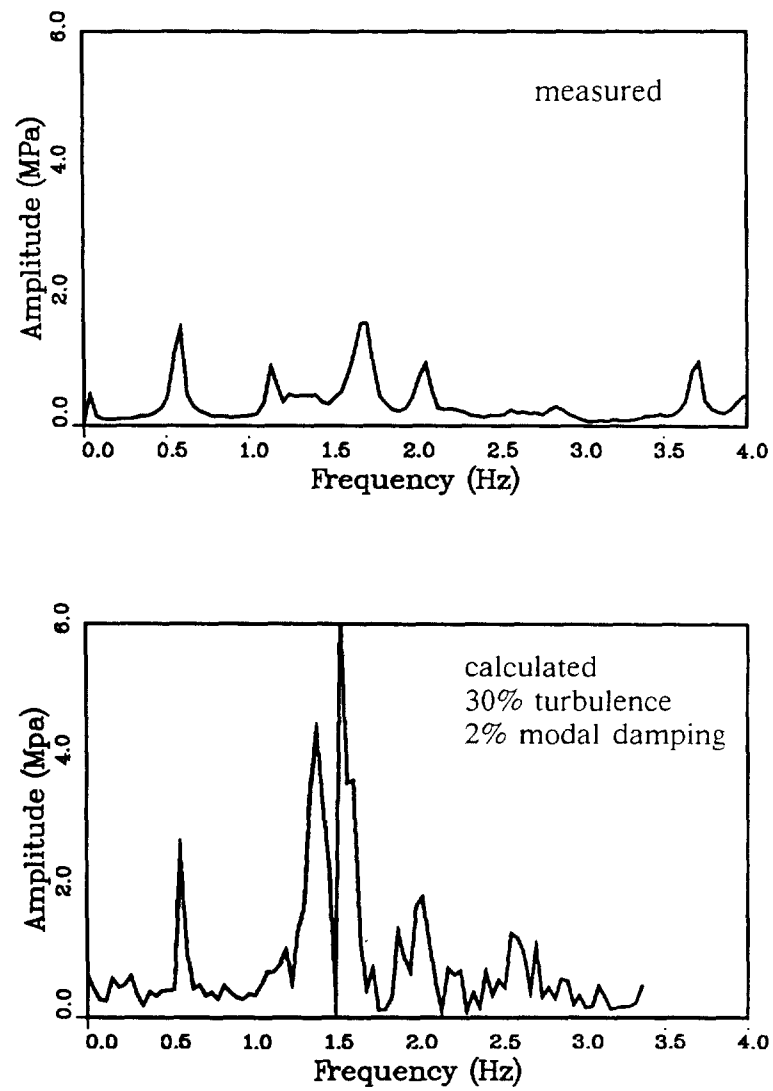


Figure 17: Amplitude spectra of lead-lag stress response at 34 rpm, 15.6 m/s wind.

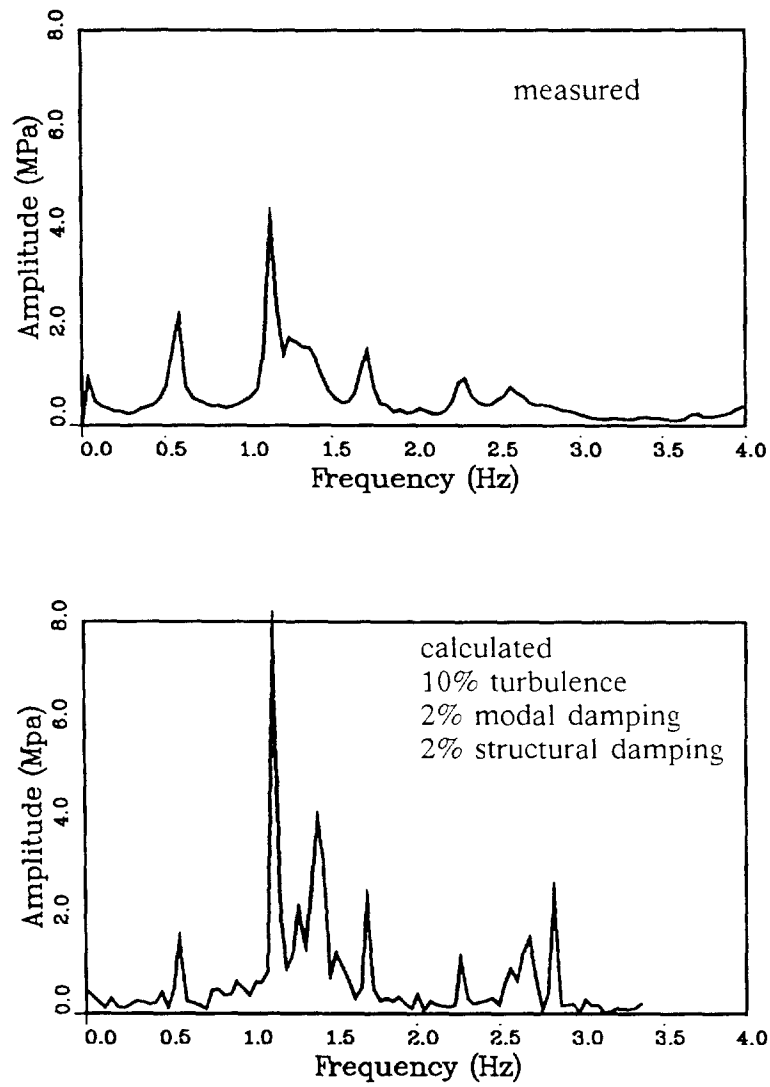


Figure 18: Amplitude spectra of flatwise stress response at 34 rpm, 15.6 m/s wind.

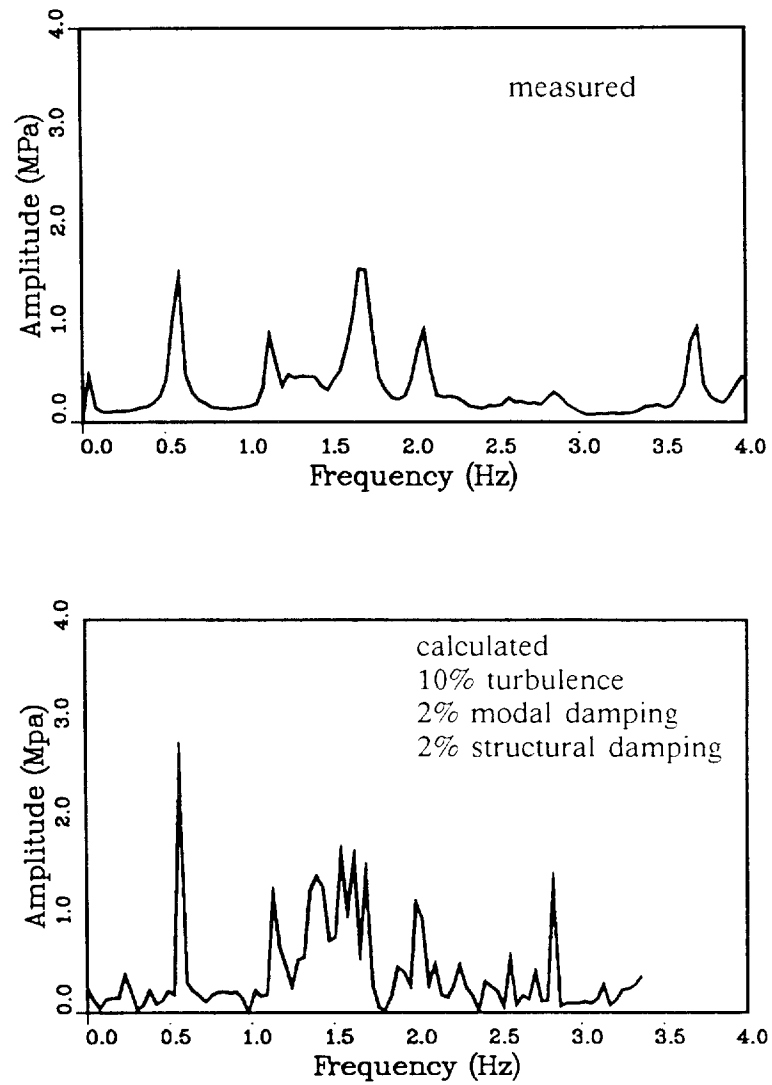


Figure 19: Amplitude spectra of lead-lag stress response at 34 rpm, 15.6 m/s wind.

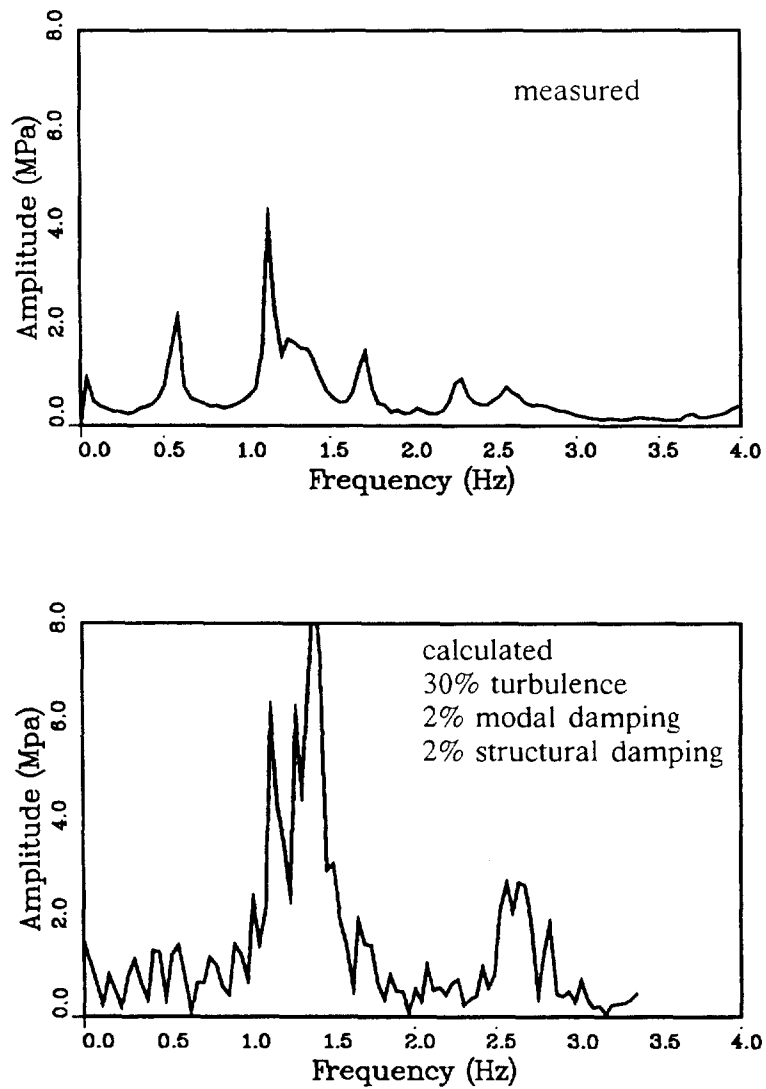


Figure 20: Amplitude spectra of flatwise stress response at 34 rpm, 15.6 m/s wind.

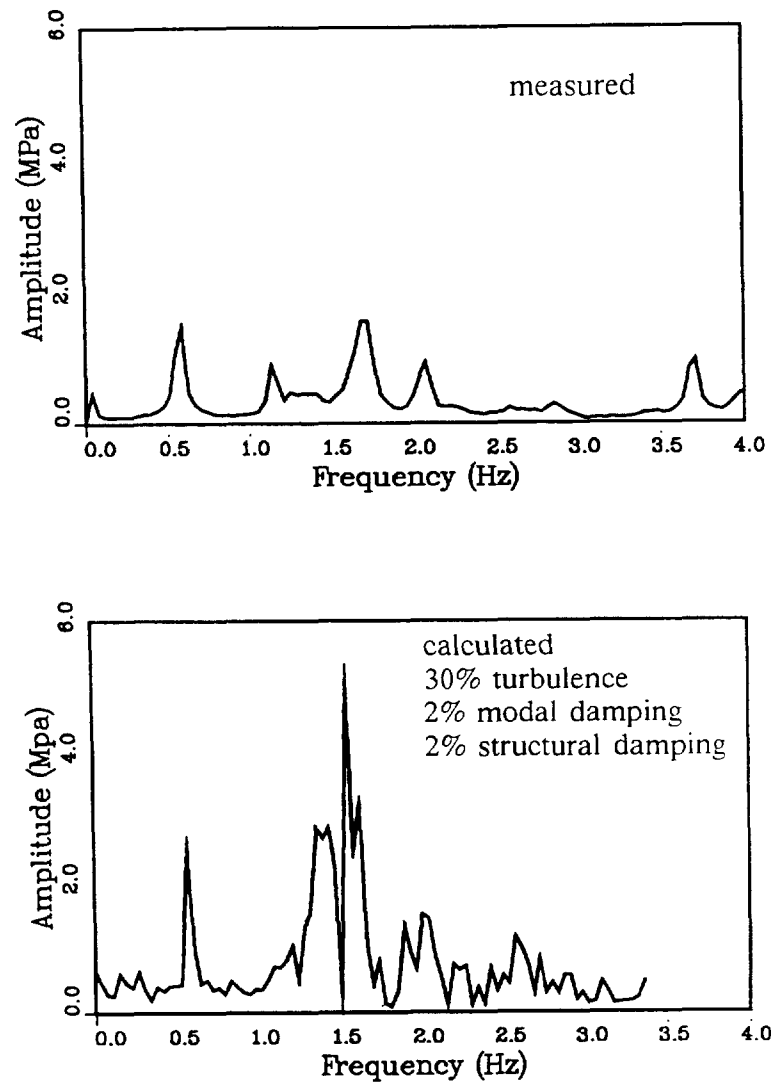


Figure 21: Amplitude spectra of lead-lag stress response at 34 rpm, 15.6 m/s wind.

Comparison with results from Malcolm

The results presented in the preceding section show a flatwise stress underestimation at 1P. Malcolm [4] used the "Mode Acceleration Module (MAM)" of NASTRAN to approximate the effect of high-frequency modes neglected in the modal response [4]. This module was used and results are shown in Table 10.

Table 10: Harmonic stresses in MPa at 34 rpm in a 15.6 m/s wind with 10% turbulence using 2% modal damping and 2% structural damping. (upper root)

	without MAM		with MAM		Sandia experimental [13.]	
Fre- quency	flat- wise	lead- lag	flat- wise	lead- lag	flat- wise	lead- lag
1P	1.54	2.51	2.70	3.00	2.20	1.48
2P	7.56	1.20	8.05	1.32	4.17	0.89
3P	2.33	1.40	2.18	1.43	1.51	1.55
4P	1.14	0.48	1.17	0.42	0.86	0.24
5P	2.46	1.29	2.46	1.29	0.40	0.29

The high-frequency modes approximation with MAM modifies 1P and 2P stresses when compared to the solution without the MAM and it insures a good numerical convergence with a limited number of modes in the modal response solution. The effect on off-harmonic stresses is negligible.

A comparison with Sandia measured data and Malcolm's predictions, using the TRES4 computer model, [13] is shown in Figures 22 to 25. The two computer models, IREQ's and TRES4, differ as shown in Table 11.

Table 11: Characteristic of computer models.

	IREQ's model	TRES4
Aerodynamic model	unsteady (MCL)	quasi-steady (DMST)
NASTRAN's solution	modal frequency response <i>without random module</i>	modal frequency response <i>with random module</i>
Damping model	2% modal	aeroelastic
Time step (s)	0.049	0.11
Number of revolutions	15	16

IREQ's aerodynamic model, with its unsteady wake, introduces phase lags to the aerodynamic loads. This gives a better representation of reality and should give a more adequate load distribution. However, the present approach overestimates off-harmonic stresses as compared to TRES4. The effect of the aeroelastic damping model is important for the flatwise modes. The number of wind turbine revolutions is almost the same in the two calculations, but the time step used is half of the one used in Malcolm.

Figure 22 shows good agreement for flatwise stresses at 10% turbulence. The 2P response is slightly higher in IREQ's model. There is a 1FS response at 1.39 Hz in our results that is not present in Malcolm's calculation due to the aeroelastic damping effect. The 3P response is in better agreement with experimental data in IREQ's model. In the edgewise direction, IREQ's model is closer to experimental data (Figure 23) in the 1.5-1.7 Hz range and again 3P response is closer to measured values. Figures 24 and 25 show similar results for a 30% turbulence level. A strong 1FS resonance at 1.39 Hz is shown in the flatwise stresses. A random vibration analysis and an aeroelastic damping model would be required to bring the stress levels in the experimental range. For edgewise stresses, where aeroelastic damping has little effect, IREQ's model does not show the strong 1.58 Hz resonance of Malcolm [4]. This seems to indicate that the 3P aerodynamic excitation from MCL is more accurate as compared to the excitation produced from the DMST model. To excite the 1.58 Hz complex eigenvector, the 3P aerodynamic loading must have the same phase relationship as the eigenvector. Both IREQ's

calculations and experimental data do not show such behavior. It is believed that the phase lag is estimated more accurately with MCL because of the unsteady wake model. The differences between flatwise and edgewise responses when compared to Malcolm's results tend to indicate that aeroelastic damping is responsible for most of the other differences between the two prediction models.

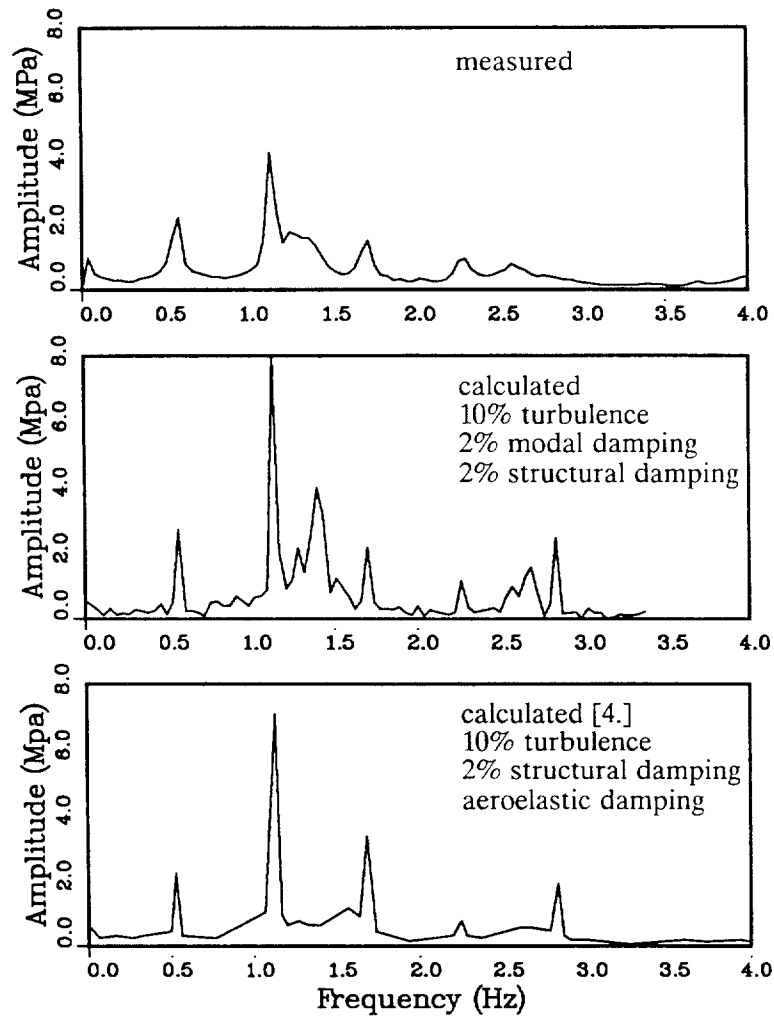


Figure 22: Amplitude spectra of flatwise stress response at 34 rpm, 15.6 m/s wind.

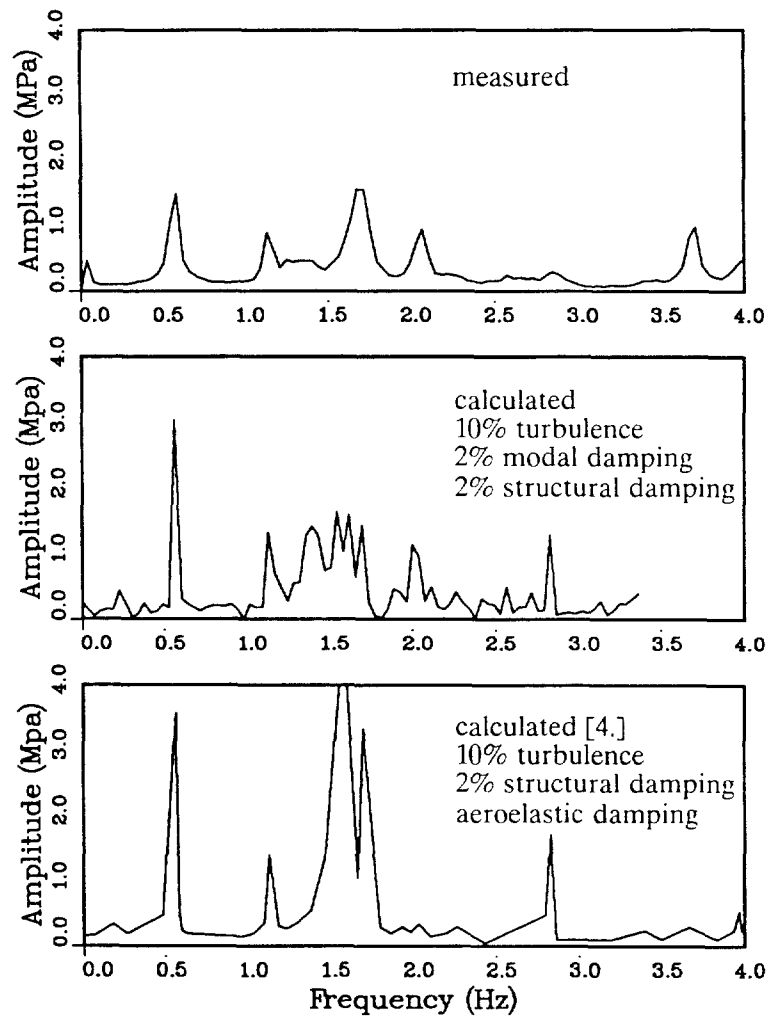


Figure 23: Amplitude spectra of lead-lag stress response at 34 rpm, 15.6 m/s wind

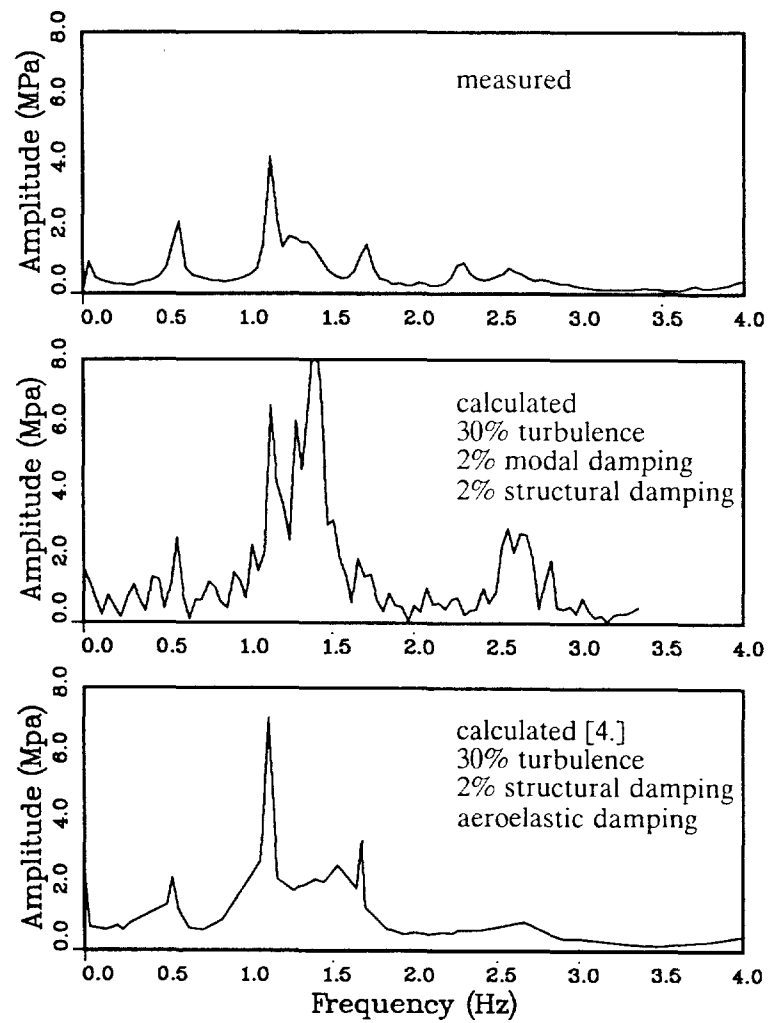


Figure 24: Amplitude spectra of flatwise stress response at 34 rpm, 15.6 m/s wind

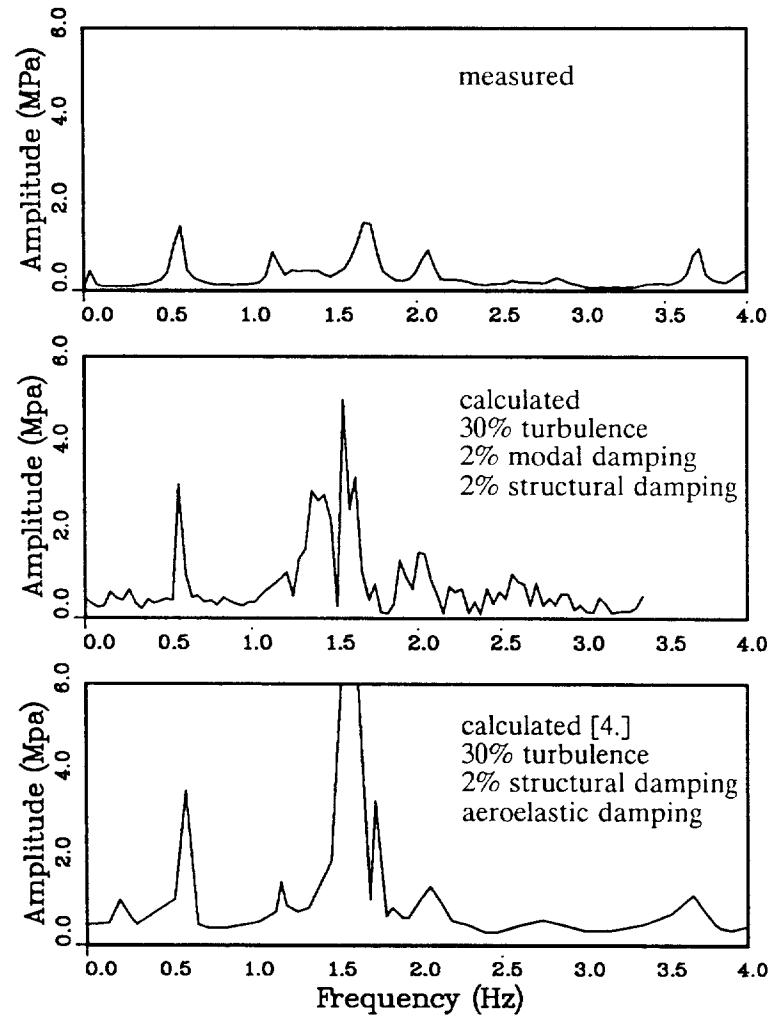


Figure 25: Amplitude spectra of lead-lag stress response at 34 rpm, 15.6 m/s wind

6. Summary

A new aerodynamic approach was used to evaluate unsteady blade stresses on the Sandia 34-meter wind turbine. Atmospheric turbulence is considered and introduced in the aerodynamic load calculations using the local circulation method code, MCL, developed at IREQ. This model uses the wind flow perturbations to estimate the local aerodynamic loads and the vortex intensities that are present in the wake. Performance data for the Sandia 34-meter Test Bed were obtained at 28 and 34 rpm; the agreement with experimental data is good. Some differences were observed in the C_p and in the power curves when they are compared with the double-multiple streamtube code SLICEIT from Sandia. The investigation, using the 17-meter turbine data as a reference, showed a similar difference between the double-multiple streamtube approach and MCL. This difference exists even if no dynamic stall model is used, the two approaches being essentially different. The performance of the Sandia 34-meter machine at 34 rpm, is well predicted by MCL over most of the wind speed range, including 15.6 m/s, where the stresses are estimated.

Interface with the structure is done using a computer code to transfer the aerodynamic loads from the aerodynamic blade nodes to structural nodes. Stresses are computed using a modal approach introduced in a NASTRAN procedure. The frequencies at zero rpm compare well with the measured and the computed values from Sandia. The Campbell diagram produced by IREQ's approach is also in good agreement with the data in Ashwill and Veers [13].

The stresses obtained are compared with the measured values in the lead-lag and the flatwise directions at the root of the blade. Results are compared with experimental data using the amplitude spectra. Computation was done at 10% and 30% turbulence using 2% modal damping with and without 2% structural damping being added. In general, the off-harmonic stresses increase with turbulence level, whereas the harmonic stresses decrease with an increase of turbulence level.

From the results obtained, lead-lag stress predictions compare well with field data and advantageously with Malcolm's results [4], taking into account the

uncertainties related to turbulent flow field, aerodynamic load estimations, structural assumptions and measurement averaging. Flatwise stresses are overestimated, especially at 2P and 1.39 Hz. The 2P stresses can be reduced by aeroelastic damping, but not at the level observed in field data. The resonance at 1.39 Hz would be easily damped using an aeroelastic damping model. The 2P overestimation required further investigation, The 3P predictions are closer to field data than with Malcolm's model. This may be due to the unsteady wake model used for the aerodynamic loading. The other discrepancies between IREQ and Malcolm models are probably produced mainly by aeroelastic damping.

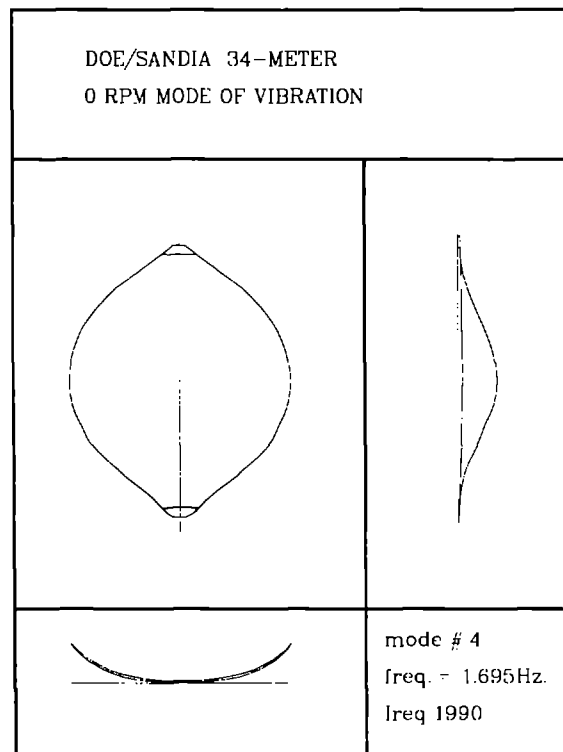
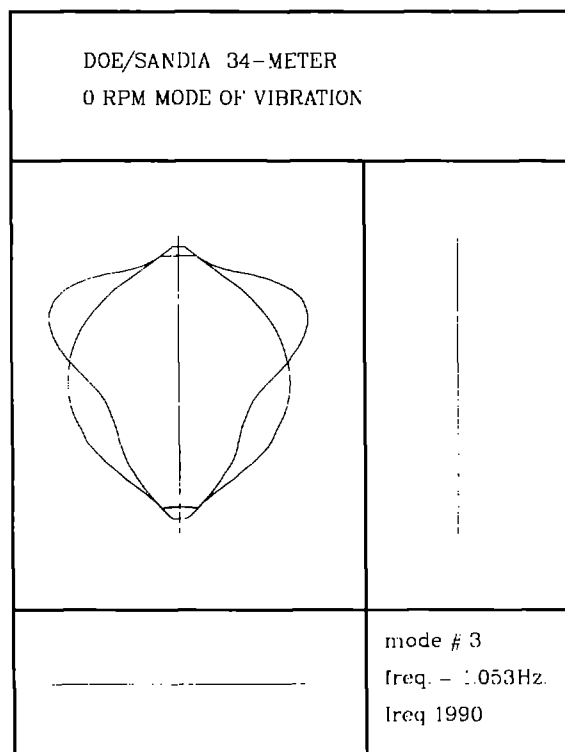
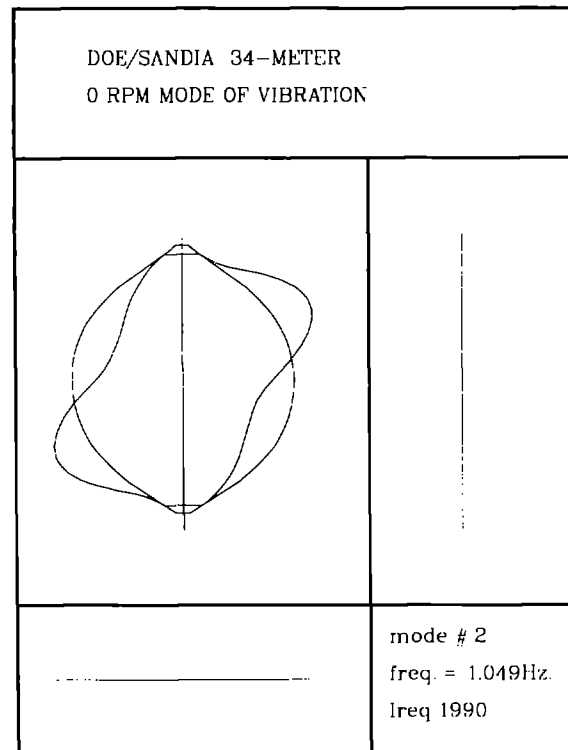
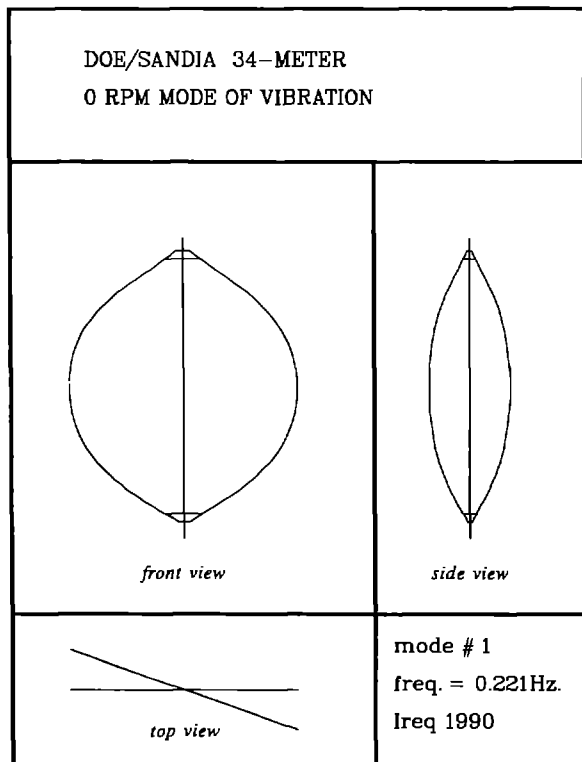
7. References

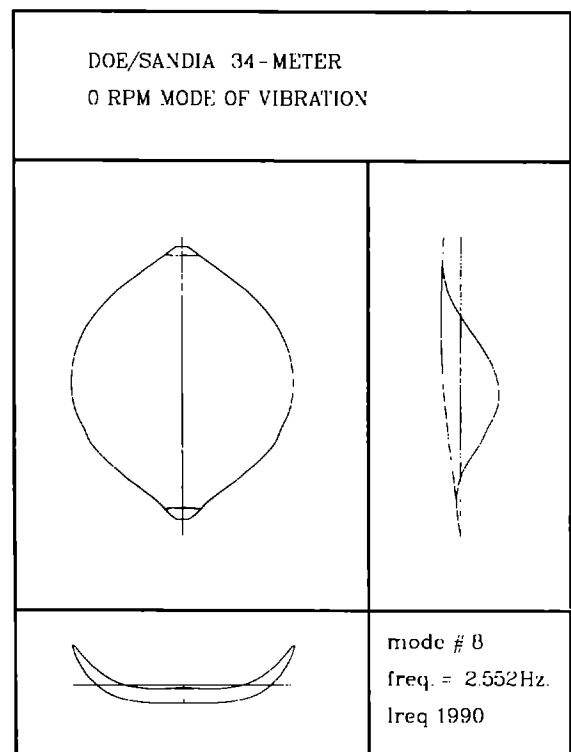
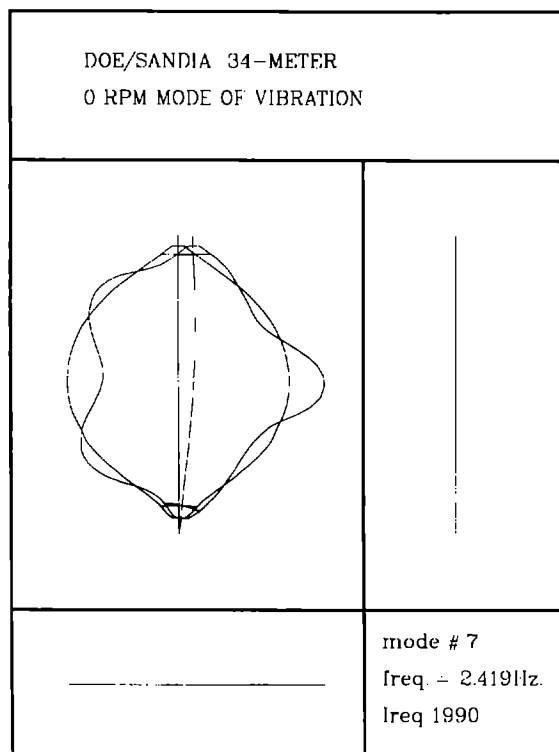
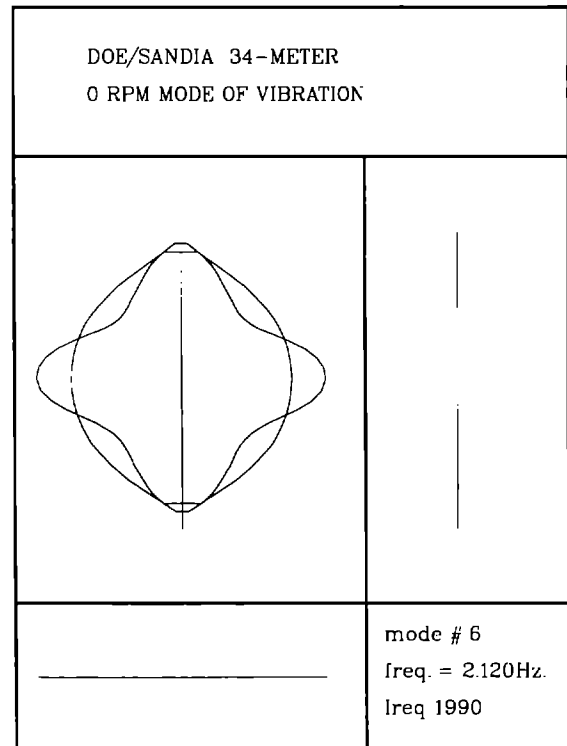
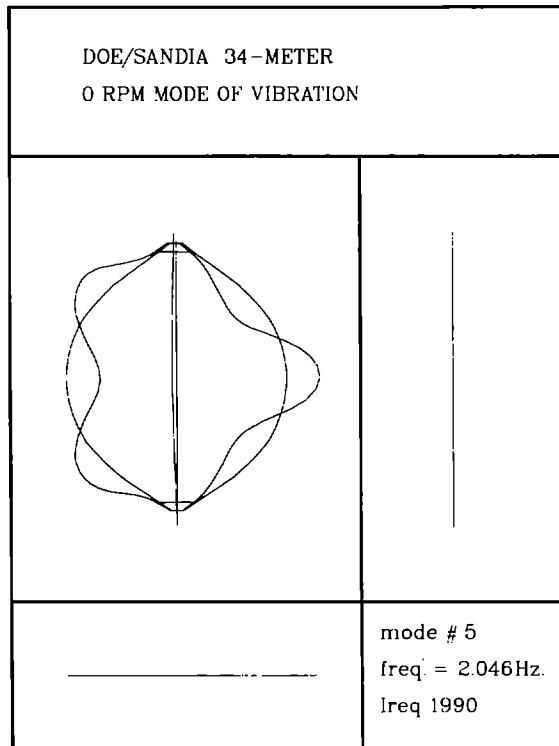
1. Massé, B., **Calcul des forces aérodynamiques instationnaires sur les pales d'une turbine d'aérogénérateur à axe vertical**, Université de Sherbrooke, Thèse de doctorat, Octobre 1987. (aussi rapport IREQ-RT4111G).
2. Frost, W. et al., **Engineering Handbook on the Atmospheric Environmental Guidelines for Use in Wind Turbine Generator Development**, NASA Technical paper 1359, December 1979.
3. Veers, P. S., **Modeling Stochastic Wind Loads on Vertical Axis Wind Turbines**, Sandia Report SAND83-1909, September 1984.
4. Malcolm, D., **Vertical Axis Wind Turbine Turbulent Wind Response Model**, Final Report Vol 1 & 2, Indal Technologies Inc., February 1987. (Also SAND88-7021, July 1988).
5. Massé, B., Pastorel, H. and Heilmann, W., **Nouveau modèle aérodynamique pour le calcul des effets de la turbulence atmosphérique sur les éoliennes Darrieus**, Energie, Mines et Ressources Canada, Rapport final, Juin 1989. (aussi rapport IREQ-4516, Nov. 1989).
6. Klimas, P. C., Dodd, H. M. and Clark, R. N., **An Overview of the DOE/Sandia/USDA Vertical Axis Wind Turbine Test Bed Project**, WindPower 87, SERI/CP-217-3315, October 1987, pp. 35-40.
7. Klimas, P. C., **Sandia National Laboratories 34-Meter Diameter Vertical Axis Wind Turbine Test Bed**, ASME Solar Energy Conference, March 1987, pp. 189-193.
8. Berg, D., private communication 1989.
9. Berg, D., **To Paint or not to Paint-What Price Beauty?**, Ninth Annual Vertical Axis Wing Turbine Research Seminar, Bushland, Texas, April 4-5, 1989.
10. Berg, D., **Test Bed Blade/Blade Joint Fairings**, Ninth Annual Vertical Axis Wing Turbine Research Seminar, Bushland, Texas, April 4-5, 1989.

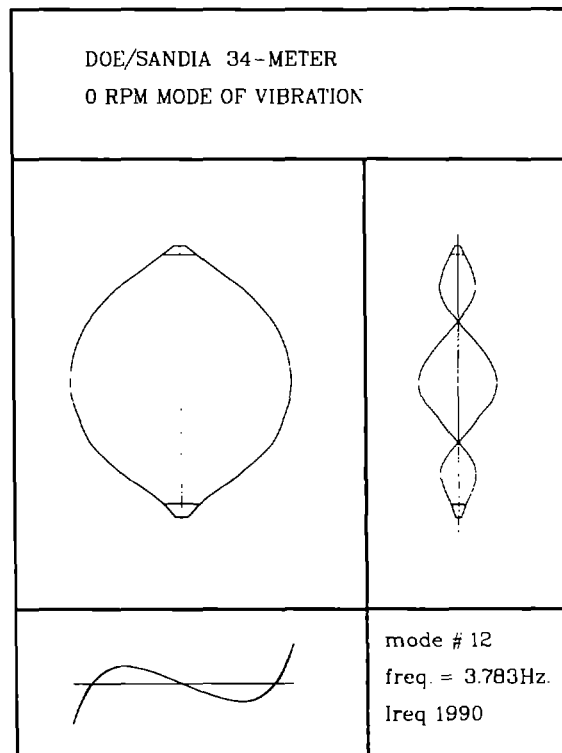
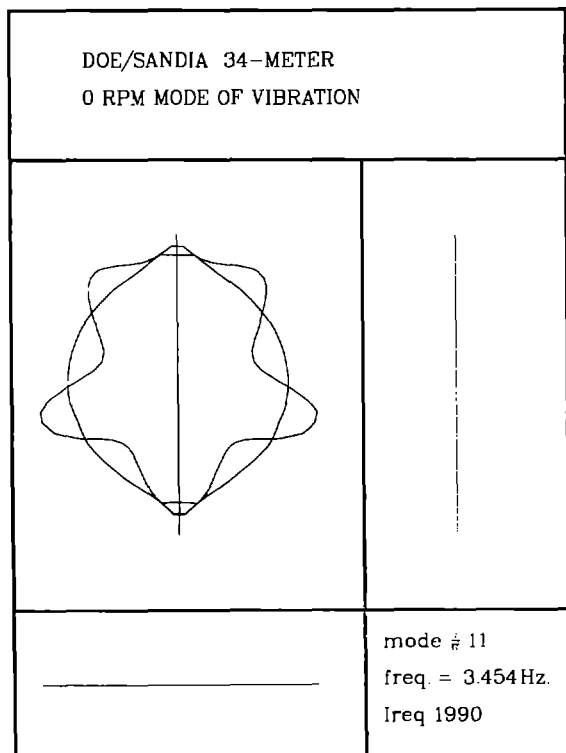
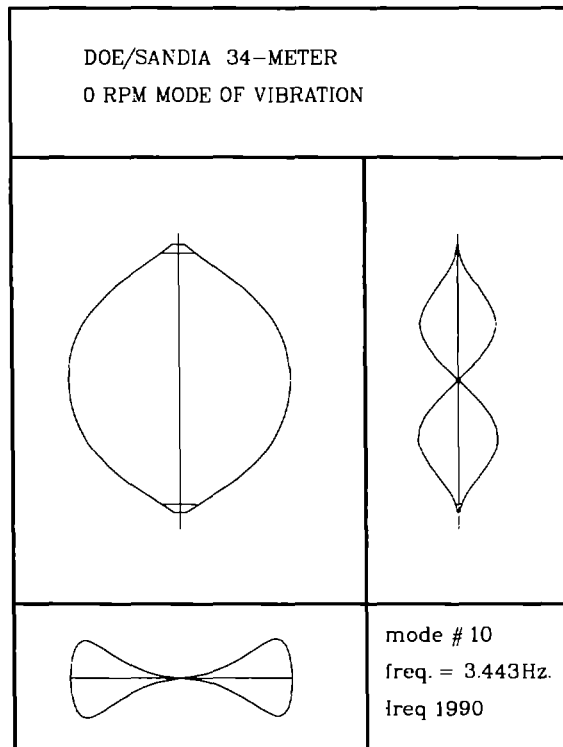
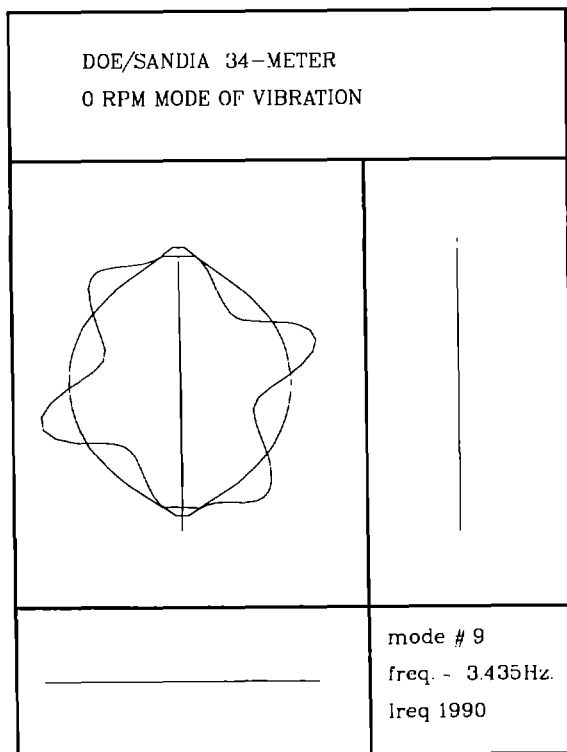
11. Massé, B. **Description de deux programmes d'ordinateur pour le calcul des performances et des charges aérodynamiques pour les éoliennes à axe vertical**, Institut de Recherche d'Hydro-Québec, IREQ-2379, July 1981.
12. Pastorel, H., **Méthode simplifiée de calcul des fréquences de résonance de rotors d'éoliennes à axe vertical**, Juin 1984, rapport IREQ-8RT3079G.
13. Ashwill, T. D. and Veers, P. S., **Structural Response Measurements and the Predictions for the Sandia 34-meter Test Bed**, Ninth ASME Wind Energy Symposium, New Orleans, LA, January 14-17, 1990.
14. Lobitz, D. W. and Sullivan, W. N., **VAWTDYN A Numerical Package for the Dynamic Analysis of Vertical Axis Wind Turbines**, Sandia Report SAND80-0085, July 1980.
15. Lobitz, D. W., **A Comparison of Finite Element Predictions and Experimental Data for the Forced Response of the DOE 100 Kw VAWT**, 6th Biennial Wind Energy Conference and Workshop, American Solar Energy Society, June 1-2, 1983.

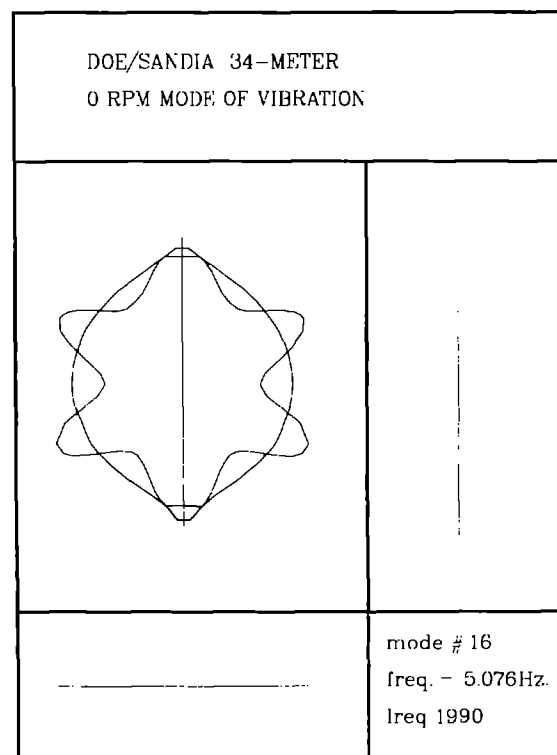
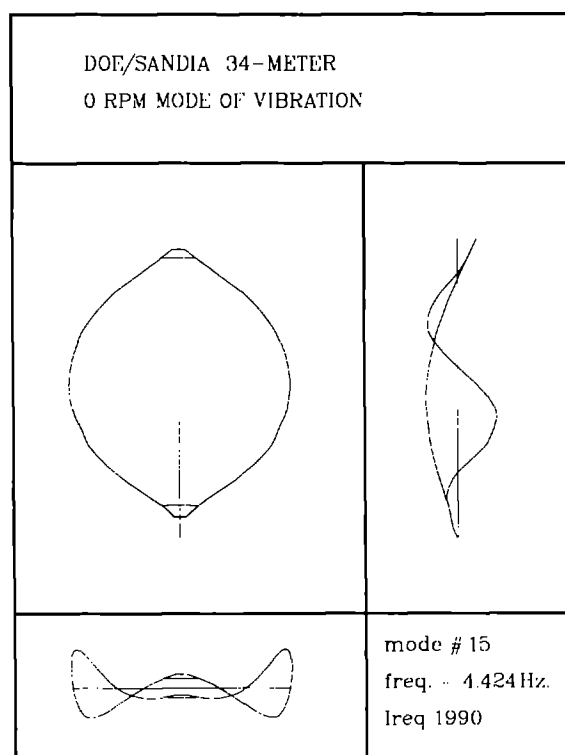
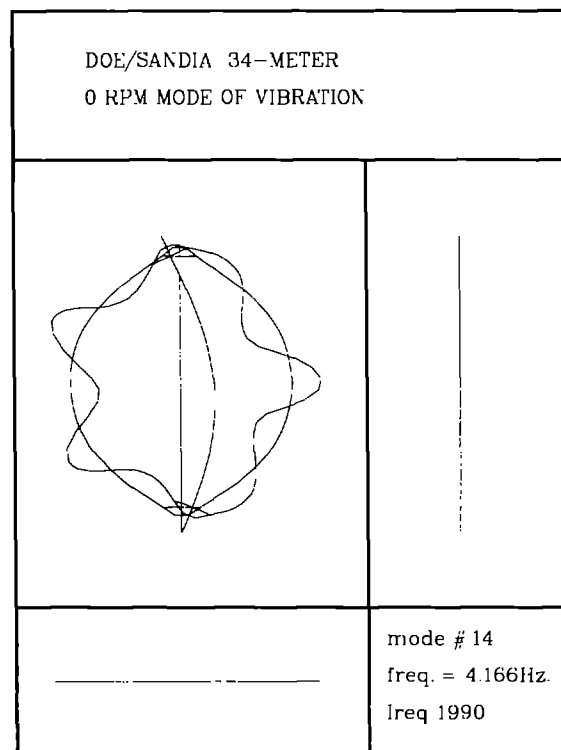
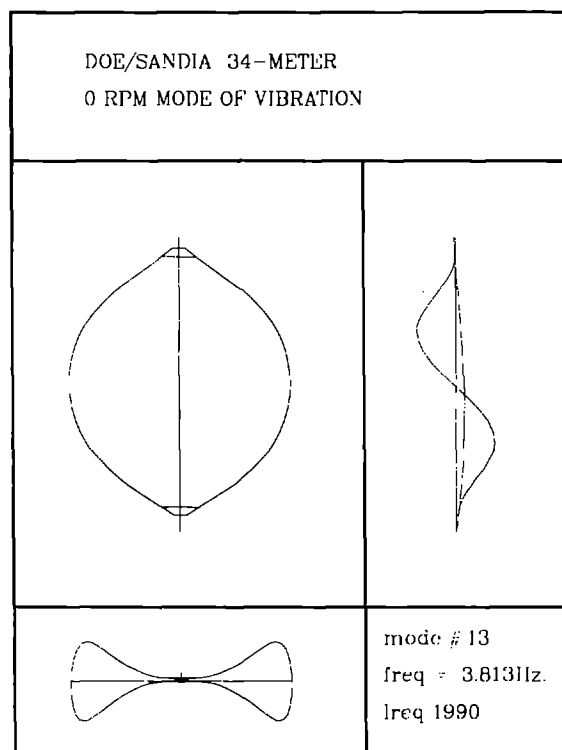
Appendix 1.

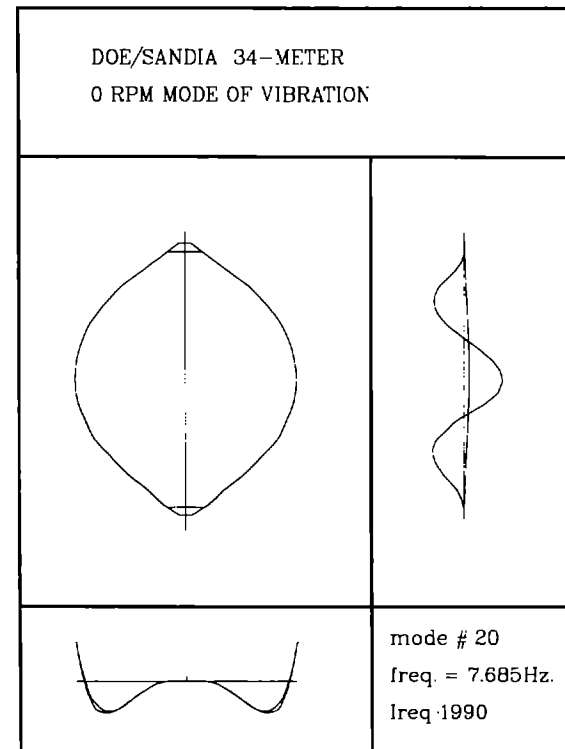
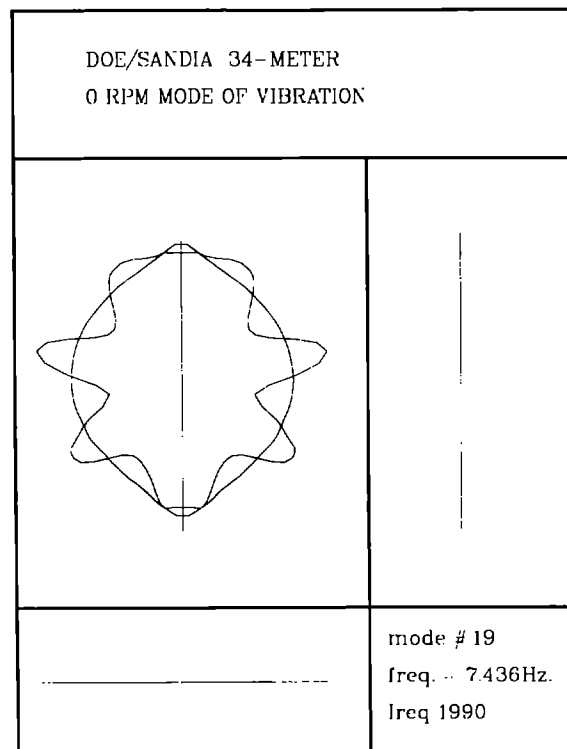
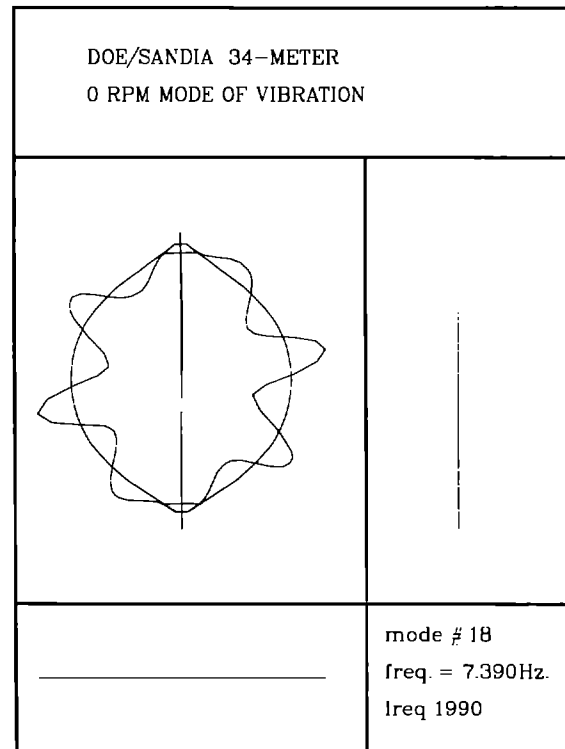
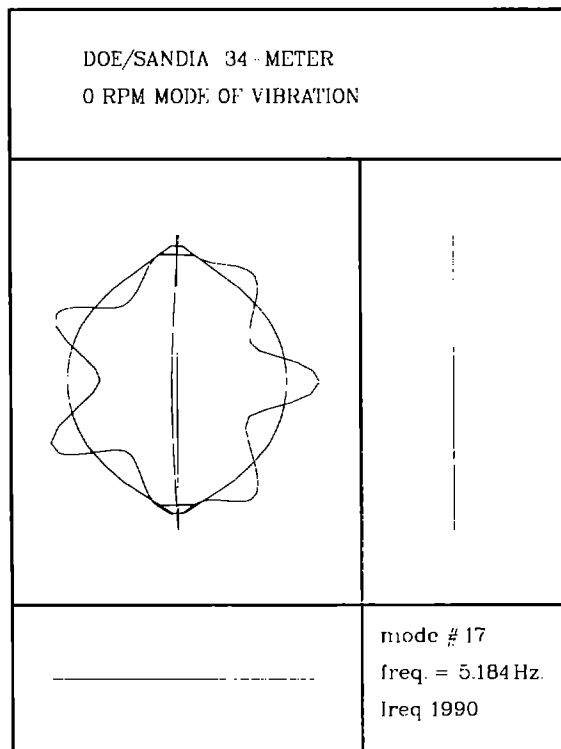
Normal modes of vibration.











Appendix 2.

Generalized complex eigenvectors.

Each complex eigenvector (rotating mode shape) may be expressed as:

$$\Phi_k^* = \sum_{i=1}^p (a_i + jb_i) \Phi_i$$

where $j^2 = -1$, p is the number of modes used for analysis and Φ_i are the normal modes (non rotating).

The following tables give, by step of 5 rpm, the values of a_i (real part) and b_i (imaginary part) in a matrix form. The rows are ordered according to the eigenvector numbers and the columns to the normal modes sequence.

Rotationnal speed : 5.0 RPM

Modal coefficients - Real part

EIGV\	1PR	1FA	1FS	1BE	2FA	2FS	1TI	1TO	3FA	2PR	3FS	3PR	2BE	2TI	2TO	4FS	4FA	5FA	5FS	3BE
1	1.00																			
2		1.00																		
3			1.00																	
4				1.00																
5					1.00		-0.03													
6						1.00														
7					0.06		1.00													
8				-0.02				1.00												
9									1.00	1.00										
10									1.00											
11			-0.02								1.00									
12												1.00								
13													1.00		-0.01					
14									-0.01					1.00			-0.01			
15													-0.01		1.00					
16																1.00				
17																	1.00			
18																		1.00		
19																			1.00	
20																				1.00

Modal coefficients - Imaginary part

EIGV\	1PR	1FA	1FS	1BE	2FA	2FS	1TI	1TO	3FA	2PR	3FS	3PR	2BE	2TI	2TO	4FS	4FA	5FA	5FS	3BE
1																				
2				-0.01									0.01							
3	-0.01									0.01										
4		-0.01					0.05													
5								-0.07												
6													-0.02							
7				0.08				0.38												
8		0.01			-0.08		0.40													
9			0.03								0.42									
10													0.03		0.01					
11										0.43		-0.01								
12						-0.04					-0.01									
13		0.03			0.01				0.03					0.10			-0.01			
14							-0.01		0.02				0.11		0.23				-0.01	
15		0.01			-0.01		-0.01							0.25			0.03			
16																				
17													-0.01		0.03					
18																				
19																				
20					-0.01		-0.01							-0.01						

Rotational speed : 10.0 RPM

Modal coefficients - Real part

EIGV#	1PR	1FA	1FS	1BE	2FA	2FS	1TI	1TO	3FA	2PR	3FS	3PR	2BE	2TI	2TO	4FS	4FA	5FA	5FS	3BE
1	1.00																			
2		1.00							-.01											
3			1.00								0.01									
4				1.00				-.02												
5					1.00		-.11													
6						1.00														
7		-.01			0.24		1.00							-.01						
8				-.06				1.00												
9									1.00											
10									1.00											
11			-.03							1.00										
12											1.00									
13												1.00								
14		-.02			0.01		0.01		-.04				1.00		-.06					
15													-.03		1.00					
16														0.01		1.00				
17																	1.00			
18																		1.00		
19																			1.00	
20																				1.00

Modal coefficients - Imaginary part

EIGV#	1PR	1FA	1FS	1BE	2FA	2FS	1TI	1TO	3FA	2PR	3FS	3PR	2BE	2TI	2TO	4FS	4FA	5FA	5FS	3BE
1																				
2				-.01				0.01					0.02							
3	-.01									0.02										
4		-.02					0.10													
5				-.02				-.18					0.01		-.01					-.01
6												-.05								
7				0.16				0.56							-.01					-.01
8		0.01			-.14		0.61													
9			0.06								0.37									
10													0.07		0.03					
11										0.37		-.02								
12						-.08					-.02									
13		0.05			0.01				0.07					0.21			-.02			
14								0.01					0.26		0.42					-.01
15		0.02			-.01		-.01		0.03					0.44			0.04			
16												0.01								
17													-.02		0.06					-.01
18																				
19																				
20					-.03		-.01							-.02			-.01			

Rotational speed : 15.0 RPM

Modal coefficients - Real part

EIGV#	1PR	1FA	1FS	1BE	2FA	2FS	1TI	1TO	3FA	2PR	3FS	3PR	2BE	2TI	2TO	4FS	4FA	5FA	5FS	3BE
1	1.00																			
2		1.00							-.01											
3			1.00								0.01									
4				1.00				-.05												
5					1.00		-.27							-.01						
6						1.00										0.01				
7		-.01			0.56		1.00							-.02			-.01			
8				-.10				1.00												
9										1.00										
10									1.00						0.01			-.01		
11			-.04			-.01					1.00								0.01	0.01
12				-.01								1.00	1.00		-.16					
13													1.00							
14		-.05			0.02		0.01		-.10					1.00			-.05			
15													-.06		1.00	1.00			0.01	
16						-.01										1.00				
17					0.01		0.01							0.02			1.00			
18								0.01										1.00		
19										-.01									1.00	
20																				1.00

Modal coefficients - Imaginary part

EIGV#	1PR	1FA	1FS	1BE	2FA	2FS	1TI	1TO	3FA	2PR	3FS	3PR	2BE	2TI	2TO	4FS	4FA	5FA	5FS	3BE
1																				
2				-.02				0.01					0.02		0.01					
3	-.02									0.03										
4		-.03			-.02		0.16													
5				-.10				-.33					0.01		-.01					-.01
6												-.07								
7				0.26			0.62						0.01		-.02					-.01
8		0.02			-.18		0.72							0.01						
9			0.09								0.30									
10													0.12		0.04					
11										0.31		-.03								
12		0.08			0.03				0.12					0.37			-.04			
13						-.12					-.03									
14				0.01			0.01						0.49		0.56					-.02
15		0.02			-.02		-.01		0.04					0.58			0.05			
16											0.01									
17				-.01									-.03		0.08					-.01
18																				
19																				
20					-.04		-.02							-.03			-.01			

Rotationnal speed : 20.0 RPM

Modal coefficients - Real part

EIGV#	1PR	1FA	1FS	1BE	2FA	2FS	1TI	1TO	3FA	2PR	3FS	3PR	2BE	2TI	2TO	4FS	4FA	5FA	5FS	3BE
1	1.00																			
2		1.00					0.01		-.02											
3			1.00								0.02									
4				1.00				-.09					0.01							
5		0.01			1.00		-.47							-.01						
6						1.00										0.02				
7		-.02			0.95		1.00								-.04					
8				-.14				1.00												
9										1.00		0.01								
10		-.01							1.00					0.01						
11			-.05			-.01					1.00									
12				-.01				-.01					1.00		-.32				0.02	0.01
13										0.01		1.00								
14		-.11			0.03		0.02		-.24					1.00			-.08	0.01		
15								-.01					-.08		1.00					0.01
16						-.02										1.00				
17					0.01		0.01							0.04			1.00			
18									0.02									1.00		
19											-.02								1.00	
20																				1.00

Modal coefficients - Imaginary part

EIGV#	1PR	1FA	1FS	1BE	2FA	2FS	1TI	1TO	3FA	2PR	3FS	3PR	2BE	2TI	2TO	4FS	4FA	5FA	5FS	3BE
1																				
2				-.03				0.01					0.03		0.01					
3	-.02									0.04										
4		-.05			-.05		0.22						0.02		-.01					-.01
5				-.27				-.53												
6	-.01											-.10								-.03
7				0.33				0.63					0.02		-.04					
8		0.02			-.21		0.79							0.01						
9			0.12								0.26									
10				-.01									0.22		0.06					
11										0.27		-.05								
12		0.10			0.06		0.01		0.21					0.58			-.07			
13			0.01			-.16					-.05									
14				0.01				0.02					0.82		0.68					-.02
15		0.03			-.02		-.02		0.05					0.68			0.04			
16												0.01								
17				-.01									-.03		0.09					-.02
18																				-.01
19																				
20					-.05		-.03								-.04		-.02	-.01		

Rotational speed : 25.0 RPM

Modal coefficients - Real part

EIGV#	1PR	1FA	1FS	1BE	2FA	2FS	1TI	1TO	3FA	2PR	3FS	3PR	2BE	2TI	2TO	4FS	4FA	5FA	5FS	3BE
1	1.00																			
2		1.00					0.02		-.03											
3			1.00			0.01					0.03									
4				1.00				-.14					0.01							
5		0.01			1.00		-.65							-.02			-.01			
6			-.01			1.00										0.03				
7		-.02			1.00		0.75		-.01					-.06			-.02			
8				-.17				1.00							0.01					
9									1.00											
10				-.02				-.01					1.00		-.38					0.02
11		0.02			0.03		0.02		1.00					0.28			-.04	-.02		
12			-.07			-.03					1.00								0.02	
13										0.02		1.00								
14				0.01				0.02					1.00		0.63					-.02
15				0.01				-.01					-.10		1.00					0.01
16						-.02										1.00				
17					0.02		0.01							0.06			1.00			
18					-.01				0.02					-.01				1.00		
19				0.01				0.01							0.01					1.00
20											-.02								1.00	

Modal coefficients - Imaginary part

EIGV#	1PR	1FA	1FS	1BE	2FA	2FS	1TI	1TO	3FA	2PR	3FS	3PR	2BE	2TI	2TO	4FS	4FA	5FA	5FS	3BE
1																				
2				-.05				0.02					0.04		0.01					
3	-.03									0.06										
4		-.08			-.09		0.29										-.01			
5				-.51				-.73					0.02		-.01					-.01
6	-.01											-.13								
7				0.29				0.46					0.03		-.05					-.03
8		0.03			-.22		0.83							0.01			-.01			
9			0.16								0.23								0.01	
10		0.11			0.09		0.02		-.32					0.67			-.10	0.01		
11							0.01								0.25					-.01
12										0.24		-.10								
13			0.01			-.21					-.10									
14		0.17			-.03		-.03		0.43					-.82			0.08	-.01		
15		0.03			-.03		-.02		0.06					0.74			0.02			
16												0.01								
17				-.01									-.04		0.09					-.02
18																				-.16
19					-.07		-.04		-.01					-.05			-.03	-.16		
20																				

Rotationnal speed : 30.0 RPM

Modal coefficients - Real part

EIGV#	1PR	1FA	1FS	1BE	2FA	2FS	1TI	1TO	3FA	2PR	3FS	3PR	2BE	2TI	2TO	4FS	4FA	5FA	5FS	3BE
1	1.00																			
2		1.00					0.03		-.04											
3			1.00			0.01					0.04									
4				1.00				-.20					0.02		-.01					
5		0.01			1.00		-.76		-.01					-.02			-.01			
6			-.01			1.00										0.04				
7		-.02			1.00		0.61		-.01					-.08			-.02			
8				-.20				1.00					-.01		0.01					
9										1.00										0.04
10				-.04				-.03					1.00		-.64					
11		-.04			0.02		0.02		1.00					0.18			-.02	-.03		
12			-.08			-.11					1.00								0.03	
13										0.09		1.00								
14				0.01				0.02					1.00		0.51					-.02
15				0.01				-.01					-.11		1.00					0.01
16						-.03										1.00				
17					0.02		0.02							0.09			1.00			
18				0.01				0.01							0.01				1.00	1.00
19									0.03									1.00		
20											-.03								1.00	

Modal coefficients - Imaginary part

EIGV#	1PR	1FA	1FS	1BE	2FA	2FS	1TI	1TO	3FA	2PR	3FS	3PR	2BE	2TI	2TO	4FS	4FA	5FA	5FS	3BE
1																				
2			-.01										0.05		0.01					
3	-.03			-.08				0.03			0.07									
4		-.13			-.14		0.37										-.01			
5				-.81			-.89						0.02		-.01					
6	-.01											-.17								
7				0.26				0.38					0.04		-.07					-.04
8		0.03			-.23		0.87							0.01			-.01			
9			0.19			0.01					0.21								0.01	
10		0.13			0.16		0.06		0.04						0.96		-.16			
11							0.01						0.40		0.23					-.01
12										0.23		-.41								
13			0.04			-.25					-.41								-.01	
14		0.21			-.02		-.02		0.65					-.63			0.07	-.02		
15		0.04			-.03		-.02		0.08					0.79			-.01			
16												0.01								
17				-.01									-.04		0.09					-.03
18					-.08		-.04							-.06			-.04	0.02		
19																				0.02
20																				

Rotational speed : 35.0 RPM

Modal coefficients - Real part

EIGV#	1PR	1FA	1FS	1BE	2FA	2FS	1TI	1TO	3FA	2PR	3FS	3PR	2BE	2TI	2TO	4FS	4FA	5FA	5FS	3BE
1	1.00																			
2		1.00			-.02	0.01	0.07		-.05											
3			1.00								0.05									
4				1.00				-.28					0.04		-.01					
5				1.00				0.90					-.02							
6			-.01			1.00					0.01					0.05				
7		-.03			1.00		0.53		-.01					-.12			-.02			
8				-.23				1.00					-.01		0.01					
9		0.13			0.24		0.10		0.07					1.00			-.19			
10	0.01									1.00										
11		-.10			0.02		0.02		1.00					0.26			-.03	-.04		
12										-.05		1.00								
13			-.09			0.06					1.00					0.01			0.04	
14				0.01				0.03					1.00		0.43					-.02
15				0.01				-.01					-.12		1.00					0.02
16						-.04					-.01					1.00				
17					0.03		0.02							0.11			1.00			
18				0.01				0.01							0.01					1.00
19									0.04									1.00		
20											-.04								1.00	

Modal coefficients - Imaginary part

EIGV#	1PR	1FA	1FS	1BE	2FA	2FS	1TI	1TO	3FA	2PR	3FS	3PR	2BE	2TI	2TO	4FS	4FA	5FA	5FS	3BE
1			-.01																	
2				-.17				0.06					0.06		0.02					
3	-.03									0.09										
4		-.28			-.19		0.45		0.01					0.01			-.01			
5					0.88		-.73		-.01					-.03			-.01			
6	-.01											-.21								
7				0.24				0.34					0.06		-.10					-.04
8		0.04			-.23		0.90							0.01			-.01			
9				0.07				0.05					-.88		0.71					-.05
10			0.22			0.01					0.20								0.01	
11								0.01					0.70		0.34					-.01
12			-.01			-.31					0.23					-.01			0.01	
13	-.01									0.21		0.24								
14		0.25			-.02		-.02		1.00					-.56			0.07	-.05		
15		0.04			-.03		-.03		0.09					0.82			-.03			
16												0.01								
17				-.01									-.04		0.08					-.04
18					-.10		-.05							-.06			-.05	0.01		
19																				0.01
20																				

Rotationnal speed : 40.0 RPM

Modal coefficients - Real part

EIGV\	1PR	1FA	1FS	1BE	2FA	2FS	1TI	1TO	3FA	2PR	3FS	3PR	2BE	2TI	2TO	4FS	4FA	5FA	5FS	3BE
1	1.00																			
2		1.00			-.13		0.34		-.06								-.01	0.01		
3			1.00			0.01					0.06								0.01	
4		1.00			0.22		-.46		-.06					-.01	-.01		0.01	0.01		
5				1.00				0.76					-.01		-.01					-.01
6			-.01			1.00					0.01					0.06				
7		-.04			1.00		0.47		-.02					-.19			-.02			
8				-.25				1.00					-.02		0.02					
9		0.13			0.37		0.16		0.08					1.00			-.22			
10	0.01									1.00										
11				-.01				0.02					1.00		0.43					-.02
12										-.03		1.00								
13			-.11			0.03					1.00					0.01			0.05	
14		0.22			-.01		-.01		1.00					-.39			0.06	-.06		
15				0.01			-.01						-.11		1.00				0.02	
16						-.05					-.01					1.00				
17					0.03		0.03							0.13			1.00			
18				0.02				0.01							0.01				1.00	1.00
19									0.06									1.00		
20											-.05								1.00	

Modal coefficients - Imaginary part

EIGV\	1PR	1FA	1FS	1BE	2FA	2FS	1TI	1TO	3FA	2PR	3FS	3PR	2BE	2TI	2TO	4FS	4FA	5FA	5FS	3BE
1			-.01																	
2				-.65				0.25					0.06		0.03					
3	-.04									0.11										
4				0.86				-.29					0.10							
5		-.01			0.68		-.59		-.01					-.02			-.01			
6	-.01									0.01		-.25								
7				0.22				0.32					0.09		-.14					-.05
8		0.04			-.22		0.94		-.01								-.02			
9				0.10				0.07					-.79		0.75					-.07
10			0.25			0.01					0.19								0.01	
11		0.19			-.03		-.03		-.92					-.32			0.05	0.05		
12						-.36					0.11					-.02			0.01	
13	-.01									0.20		0.11								
14				-.01				-.02					-.71		-.25					0.01
15		0.05			-.03		-.03		0.12					0.83			-.06			
16											0.01									
17				-.01									-.04		0.07					-.06
18					-.11		-.06							-.07			-.06	0.01		
19																				0.01
20																				

Rotationnal speed : 45.0 RPM

Modal coefficients - Real part

EIGV#	1PR	1FA	1FS	1BE	2FA	2FS	1TI	1TO	3FA	2PR	3FS	3PR	2BE	2TI	2TO	4FS	4FA	5FA	5FS	3BE
1	1.00																			
2				1.00				-.44							-.03					
3			1.00			0.02					0.07								0.01	
4		1.00			0.08		-.13		-.07					-.01				0.01		
5				1.00				0.67							-.01					-.01
6			-.02			1.00					0.01					0.07				
7		-.06			1.00		0.41		-.03					-.31				-.01		
8				-.27				1.00					-.04		0.04					
9		0.13			0.60		0.28		0.07					1.00			-.25			
10	0.01									1.00										
11				-.01				0.03					1.00		0.40					-.02
12									-.02		1.00	1.00								
13			-.12			0.02					1.00					0.01			0.06	
14		0.20			-.01				1.00					-.35			0.05	-.07		
15				0.02				-.02					-.09		1.00					0.01
16						-.06					-.01					1.00				
17					0.04		0.03		-.01					0.15			1.00			
18				0.02				0.02							0.02					1.00
19					0.01				0.07					-.01			0.01	1.00		
20						0.01					-.06								1.00	

Modal coefficients - Imaginary part

EIGV#	1PR	1FA	1FS	1BE	2FA	2FS	1TI	1TO	3FA	2PR	3FS	3PR	2BE	2TI	2TO	4FS	4FA	5FA	5FS	3BE
1			-.01																	
2		0.39			-.27		0.60		-.03					0.01			-.02			
3	-.04									0.13										
4				0.20				-.08					0.10		0.02					
5		-.02			0.55		-.50							-.02			-.01			
6	-.01									0.01		-.30								
7				0.19				0.33					0.15		-.23					-.05
8		0.04			-.22		0.96		-.01					-.02			-.02			
9				0.16				0.10					-.73		0.78					-.10
10			0.28			0.01					0.19					0.01			0.01	
11		0.22			-.03		-.03		-.68					-.29			0.05	0.04		
12						-.41					0.07					-.02			0.01	
13	-.01									0.20		0.08								
14				-.01				-.02					-.56		-.12					0.01
15		0.07			-.03		-.04		0.18					0.83			-.08	-.01		
16																				
17				-.01									-.03		0.07					-.08
18					-.13		-.07							-.08			-.08	0.01		
19																				0.01
20																				

Rotationnal speed : 50.0 RPM

Modal coefficients - Real part

EIGV#	1PR	1FA	1FS	1BE	2FA	2FS	1TI	1TO	3FA	2PR	3FS	3PR	2BE	2TI	2TO	4FS	4FA	5FA	5FS	3BE
1	1.00																			
2				1.00				-.51					0.02		-.03					
3			1.00			0.02					0.08								0.01	
4		1.00			0.07		-.08		-.08					-.01				0.01		
5				1.00				0.61							-.02	0.08				-.02
6			-.02			1.00					0.01								-.01	
7		-.10			1.00		0.38		-.04					-.53			0.05	-.01		
8				-.27			1.00						-.07		0.07					
9		0.13			1.00		0.50		0.06					0.93			-.29			
10	0.01									1.00										
11				-.01				0.03					1.00		0.37					-.02
12										-.01		1.00								
13			-.13			0.01					1.00					0.01			0.08	
14		0.19				0.01			1.00					-.46			0.07	-.08		
15				0.02				-.02					-.01		1.00					0.01
16						-.08					-.01					1.00				
17					0.04		0.03		-.01					0.16			1.00			
18				0.02				0.02					-.01		0.02					1.00
19					0.01				0.08					-.01			0.01	1.00		
20						0.01					-.08								1.00	

Modal coefficients - Imaginary part

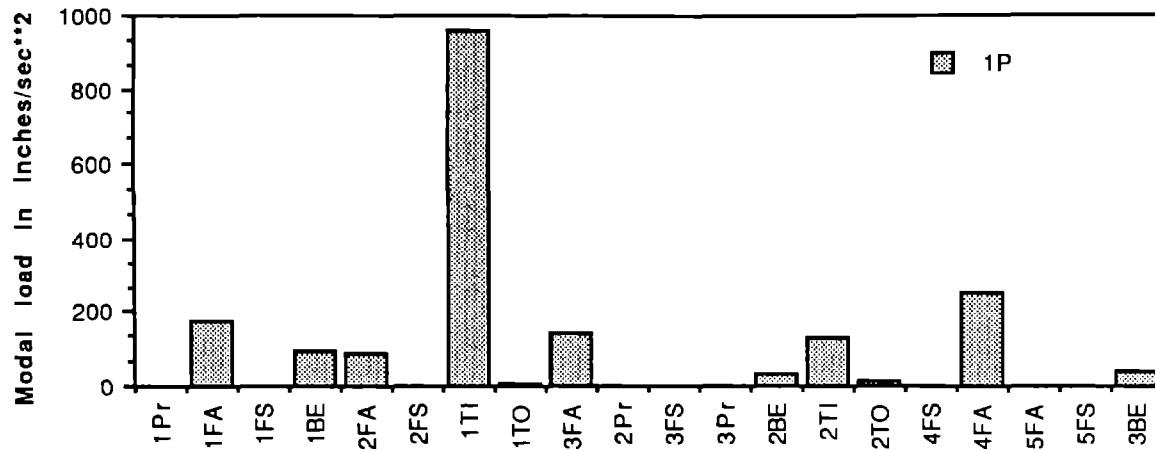
EIGV#	1PR	1FA	1FS	1BE	2FA	2FS	1TI	1TO	3FA	2PR	3FS	3PR	2BE	2TI	2TO	4FS	4FA	5FA	5FS	3BE
1			-.01																	
2		0.22			-.31		0.67		-.02					0.02			-.02			
3	-.04									0.15										
4				0.09				-.04					0.12		0.02					
5		-.03			0.47		-.43							-.02			-.01			
6	-.01									0.01		-.35								
7				0.16				0.34					0.27		-.41					-.05
8		0.03			-.25		0.95		-.01					-.05			-.01			
9				0.27				0.14					-.67		0.76					-.14
10			0.30			0.01					0.19					0.01			0.01	
11		0.25			-.03		-.03		-.55					-.27			0.05	0.04		
12						-.47					0.06					-.03			0.01	
13	-.01									0.20		0.06								
14								-.02					-.51		0.10					0.01
15		0.11			-.02		-.04		0.39					0.77			-.09	-.02		
16																				
17				-.01									-.03		0.06					-.10
18					-.15		-.08							-.09			-.10	0.01		
19																				0.01
20																				

Appendix 3.

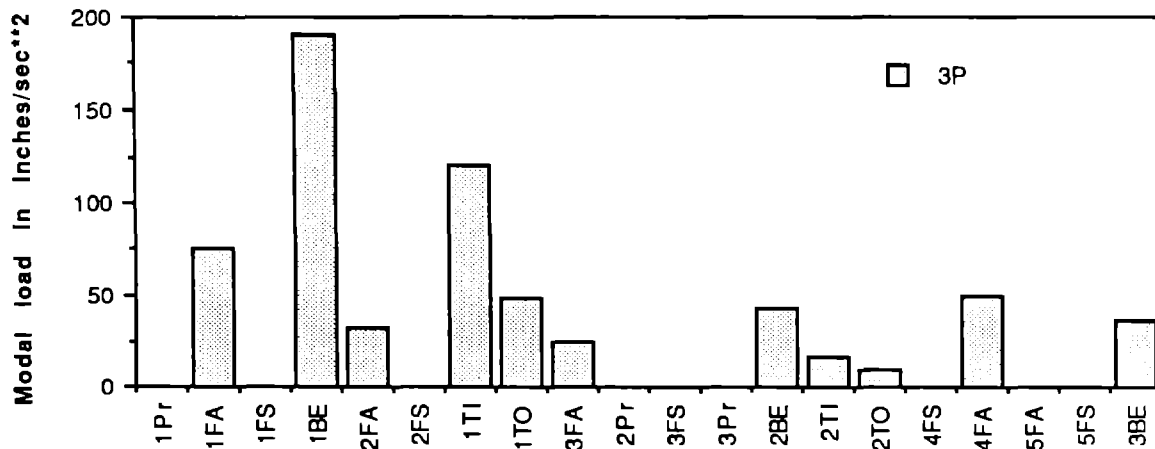
Aerodynamic harmonic loading.

The following figures show for each harmonic the aerodynamic loading applied to each normal mode.

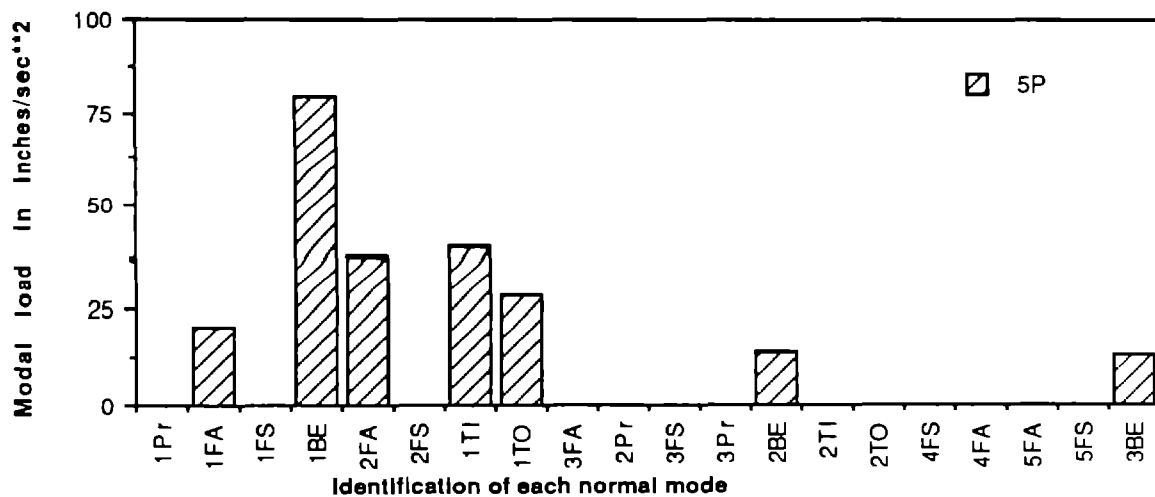
1P aerodynamic loading



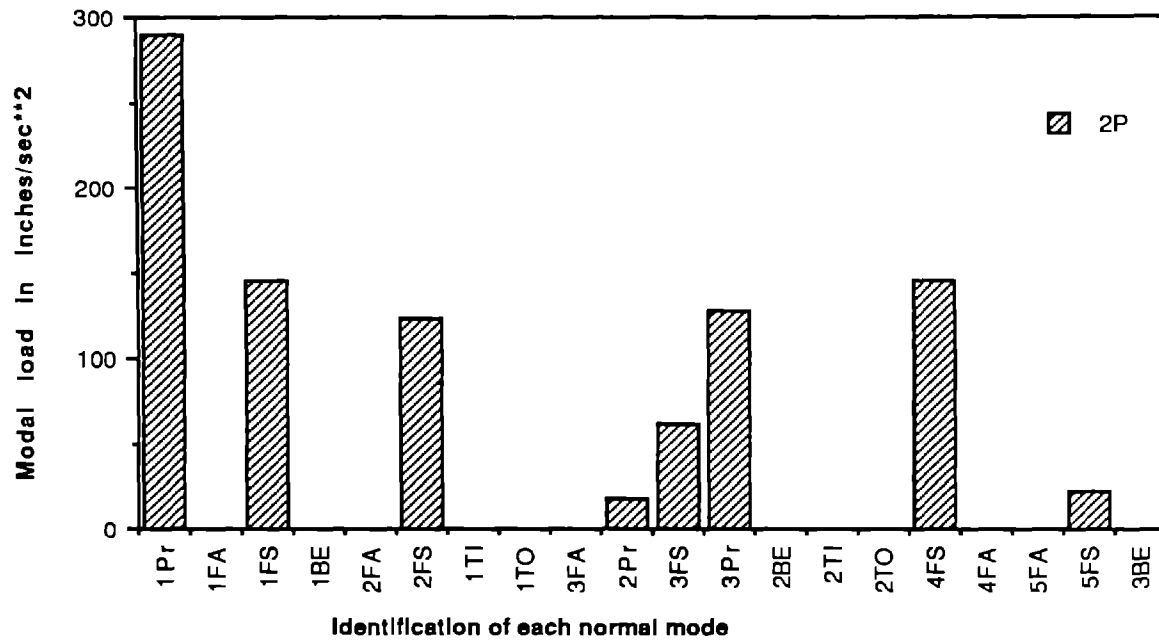
3P aerodynamic loading



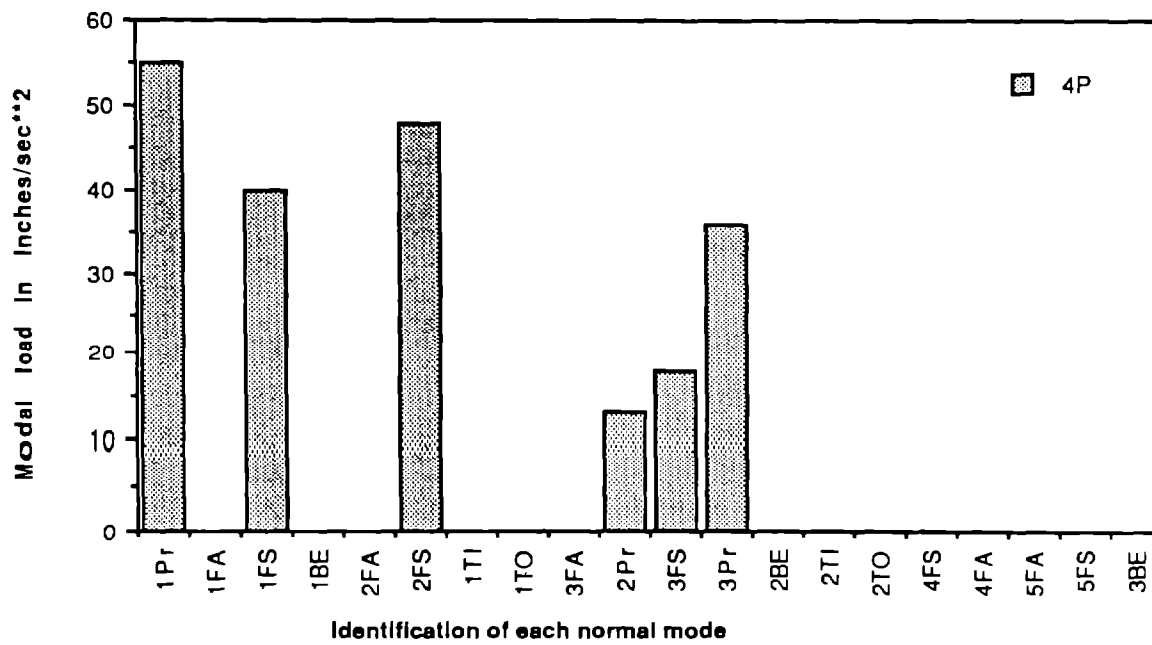
5P aerodynamic loading



2P aerodynamic loading



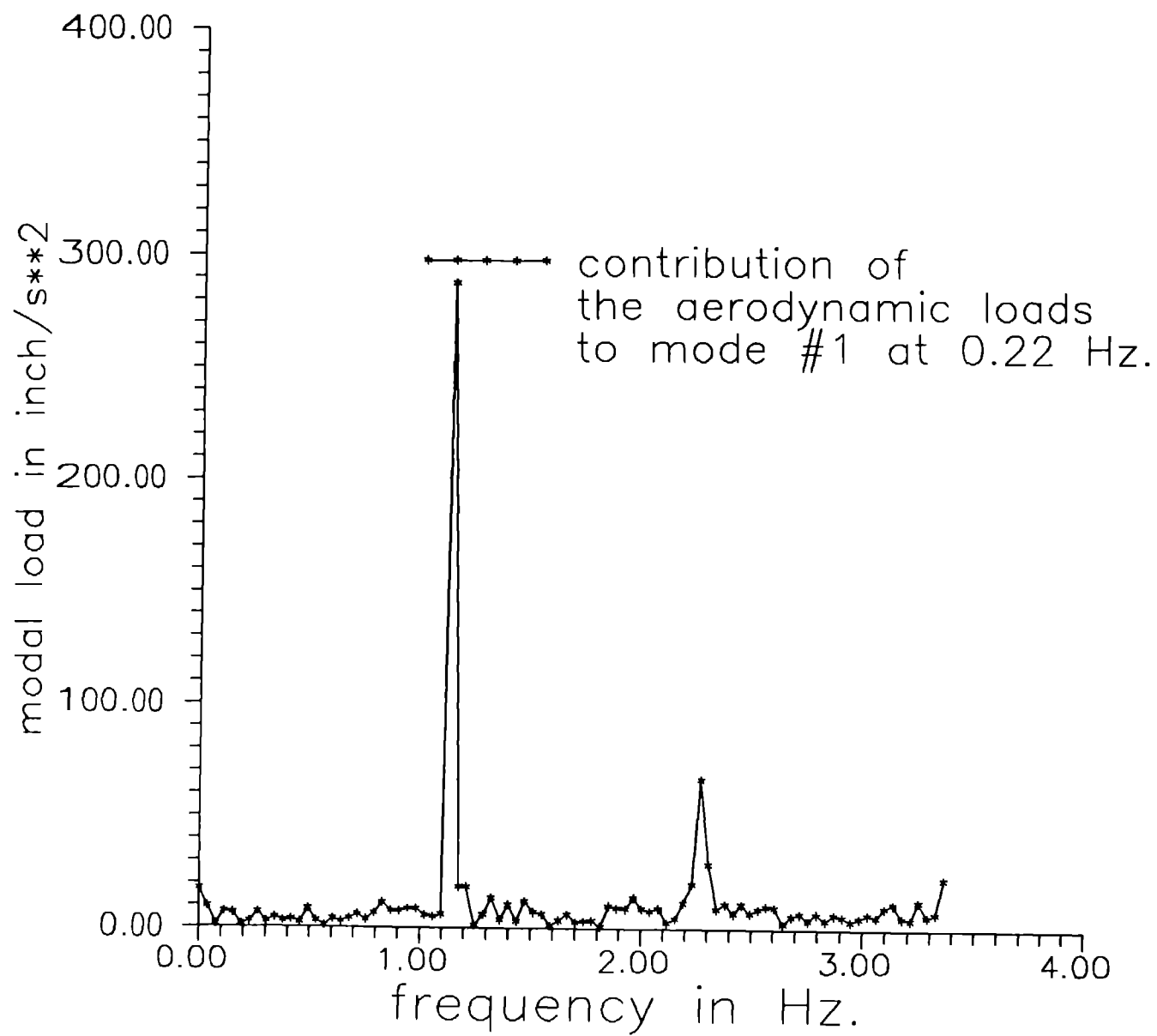
4P aerodynamic loading

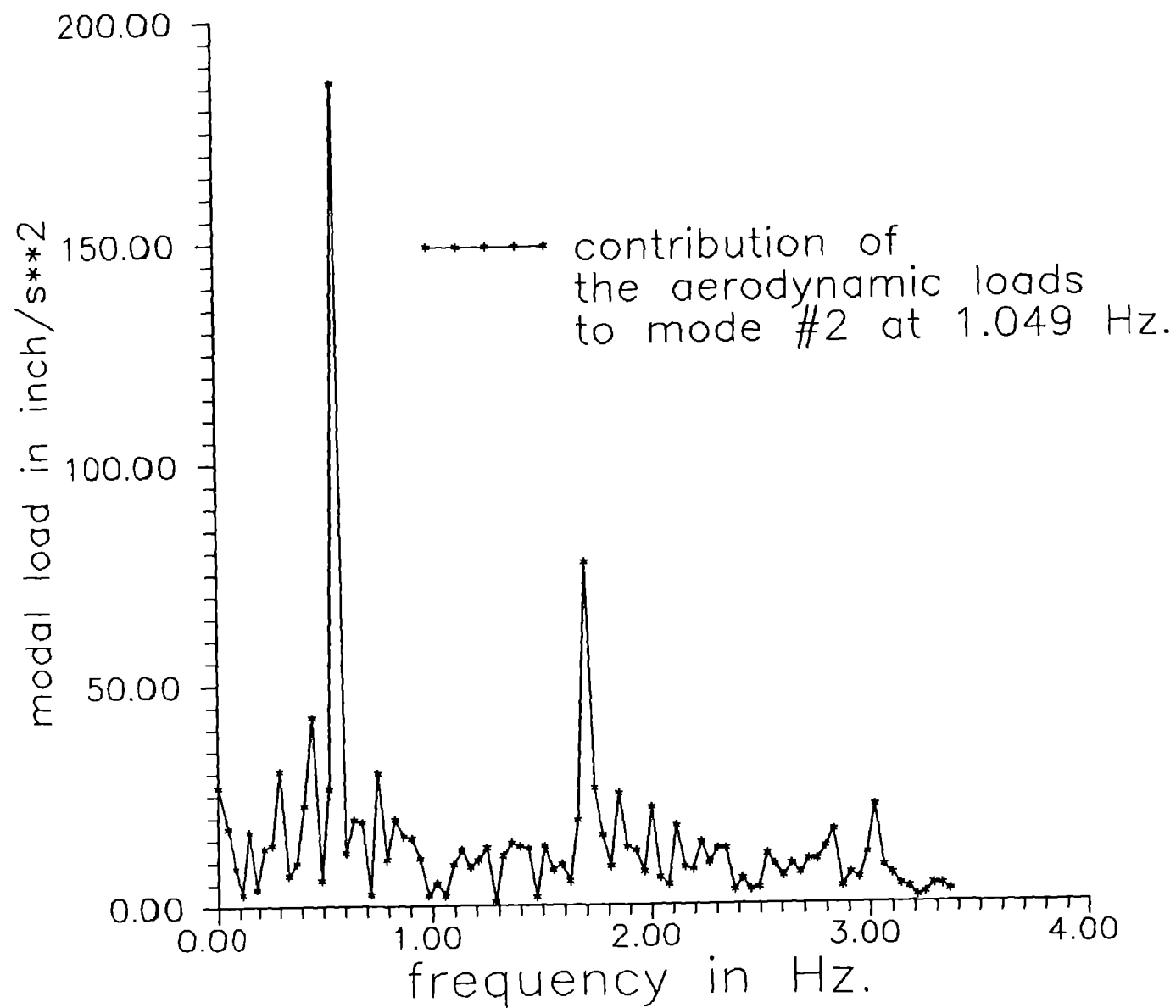


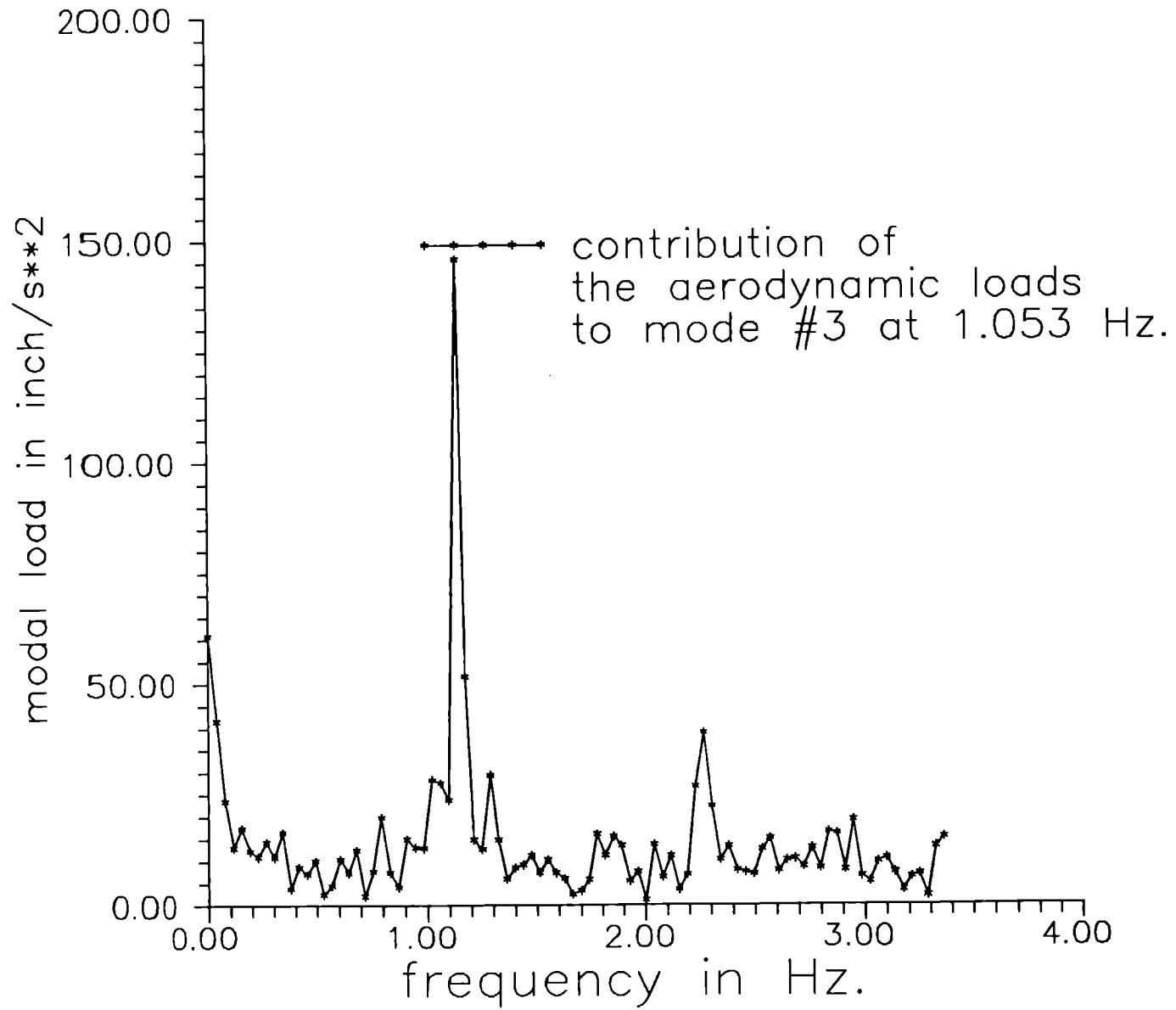
Appendix 4.

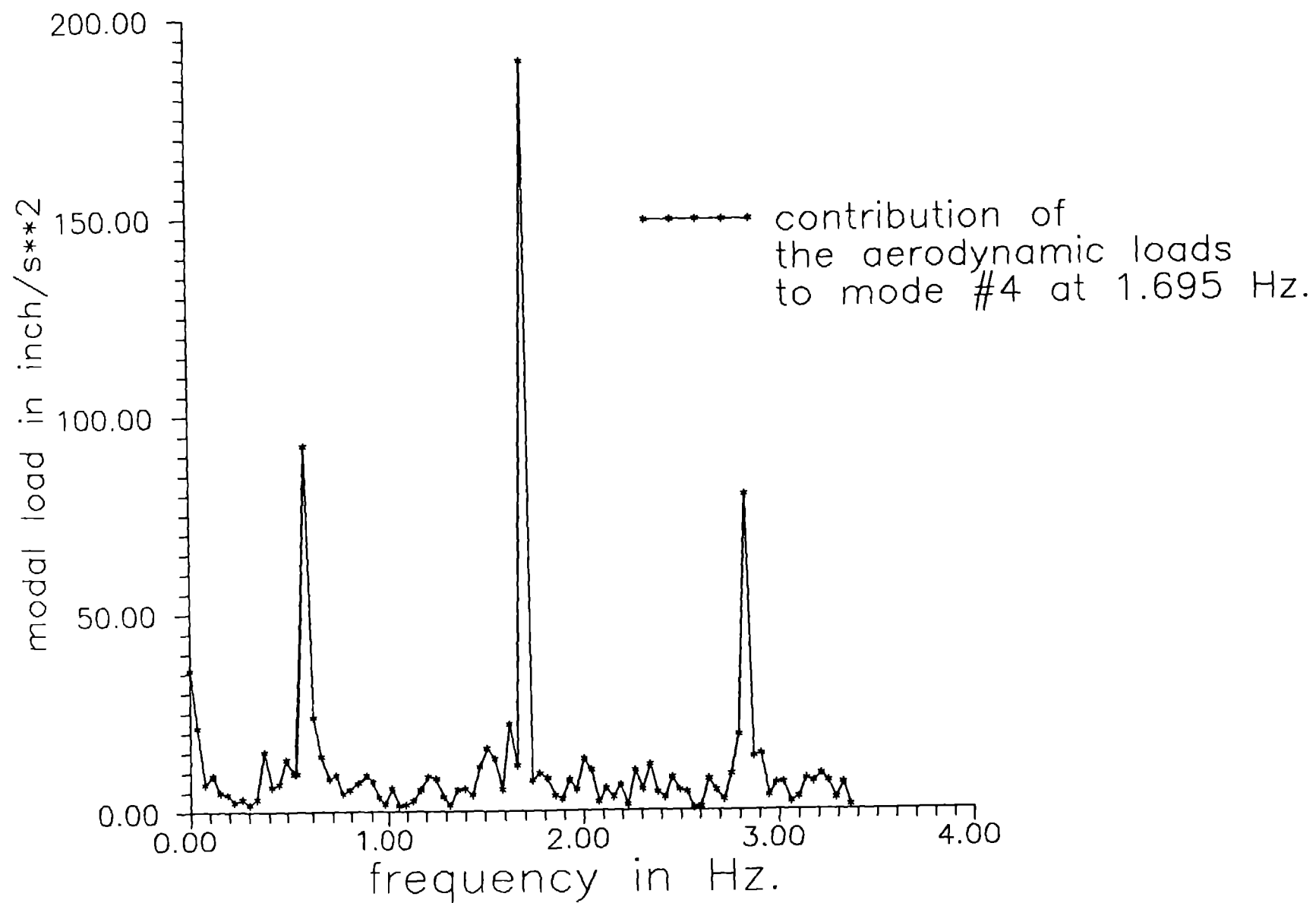
Aerodynamic modal loads applied in NASTRAN

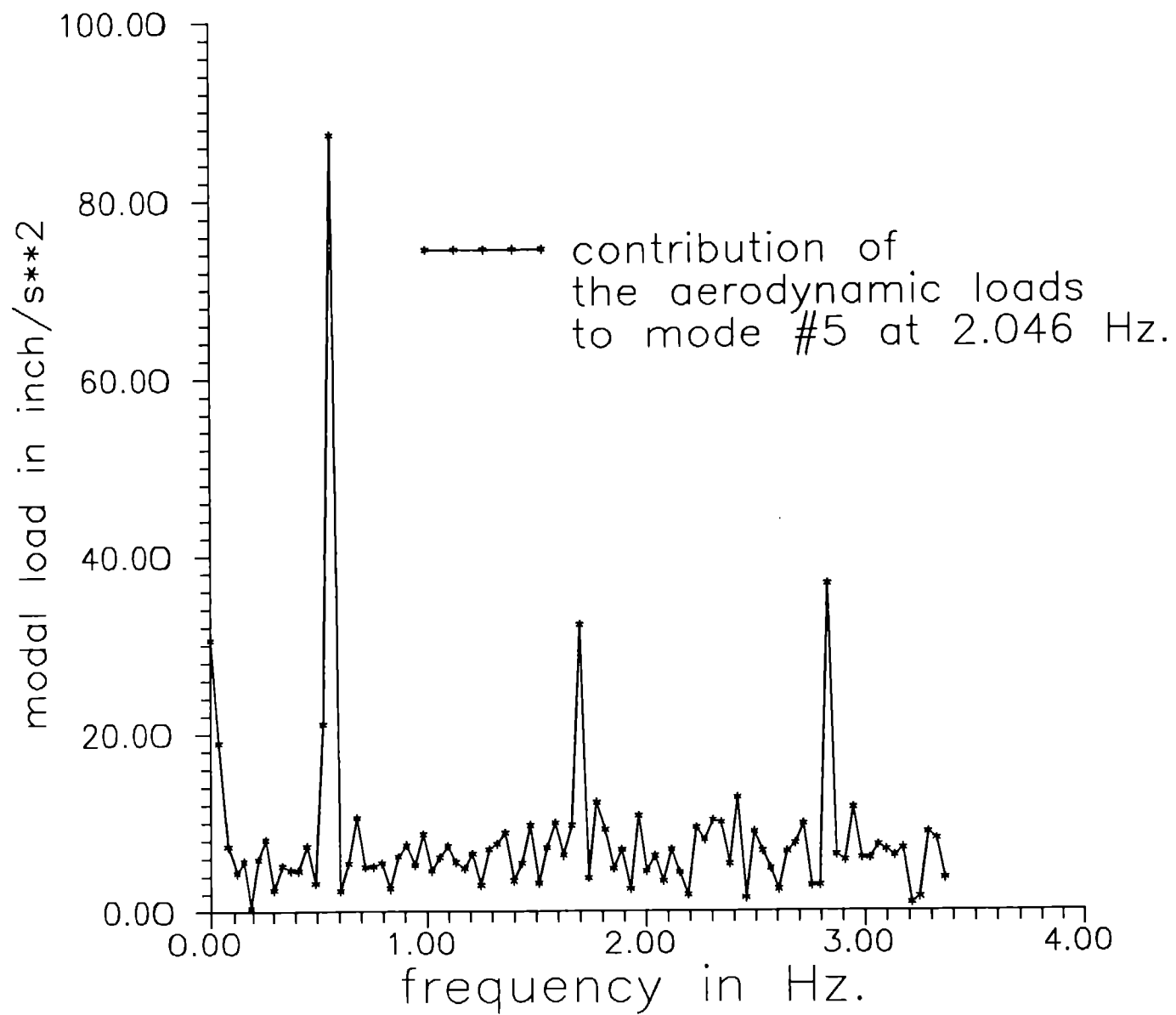
The following figures show the aerodynamic load contribution to each mode in function of frequencies. The main loading occurs at a frequency of 1 per rev. for the mode no. 7.

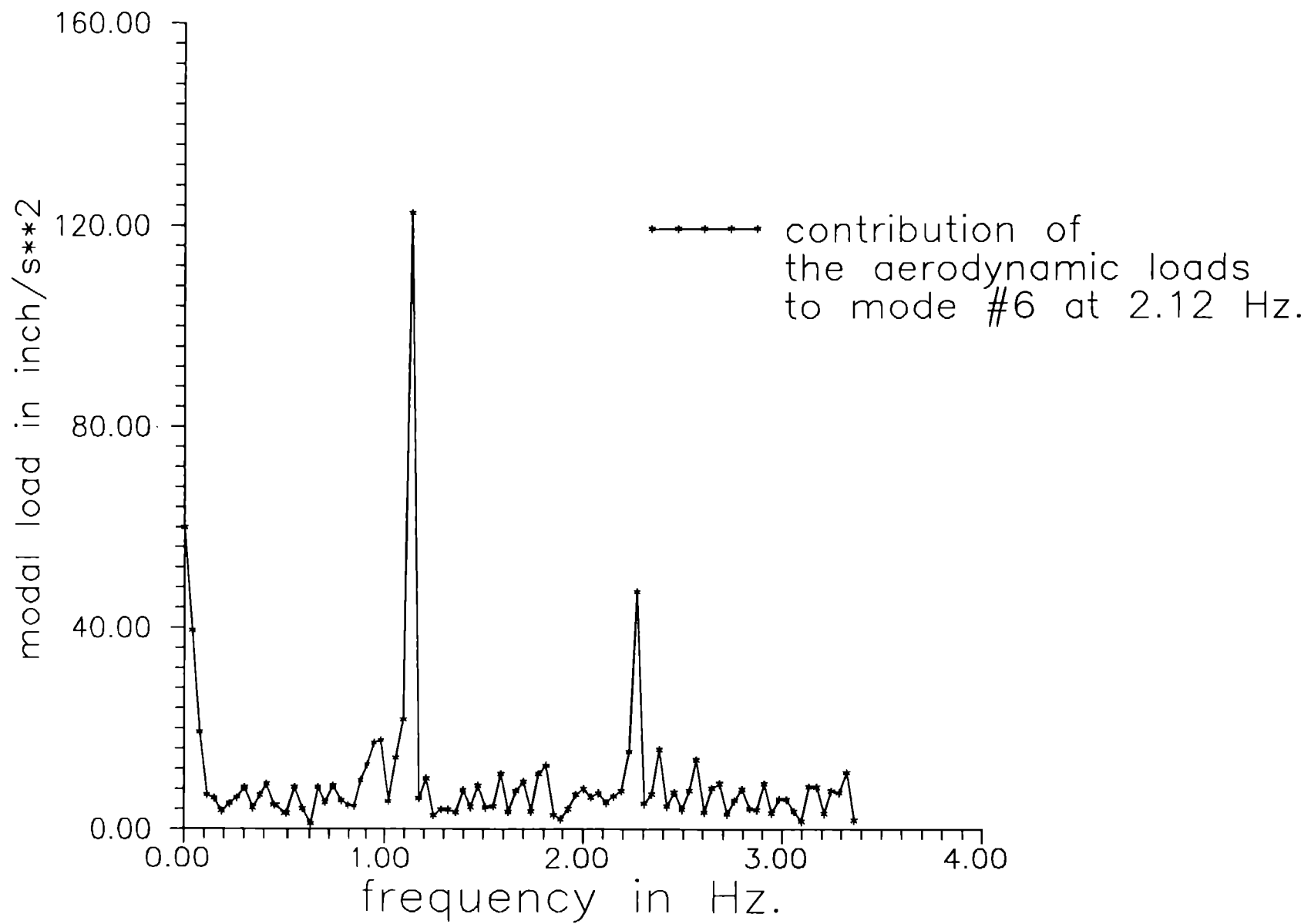


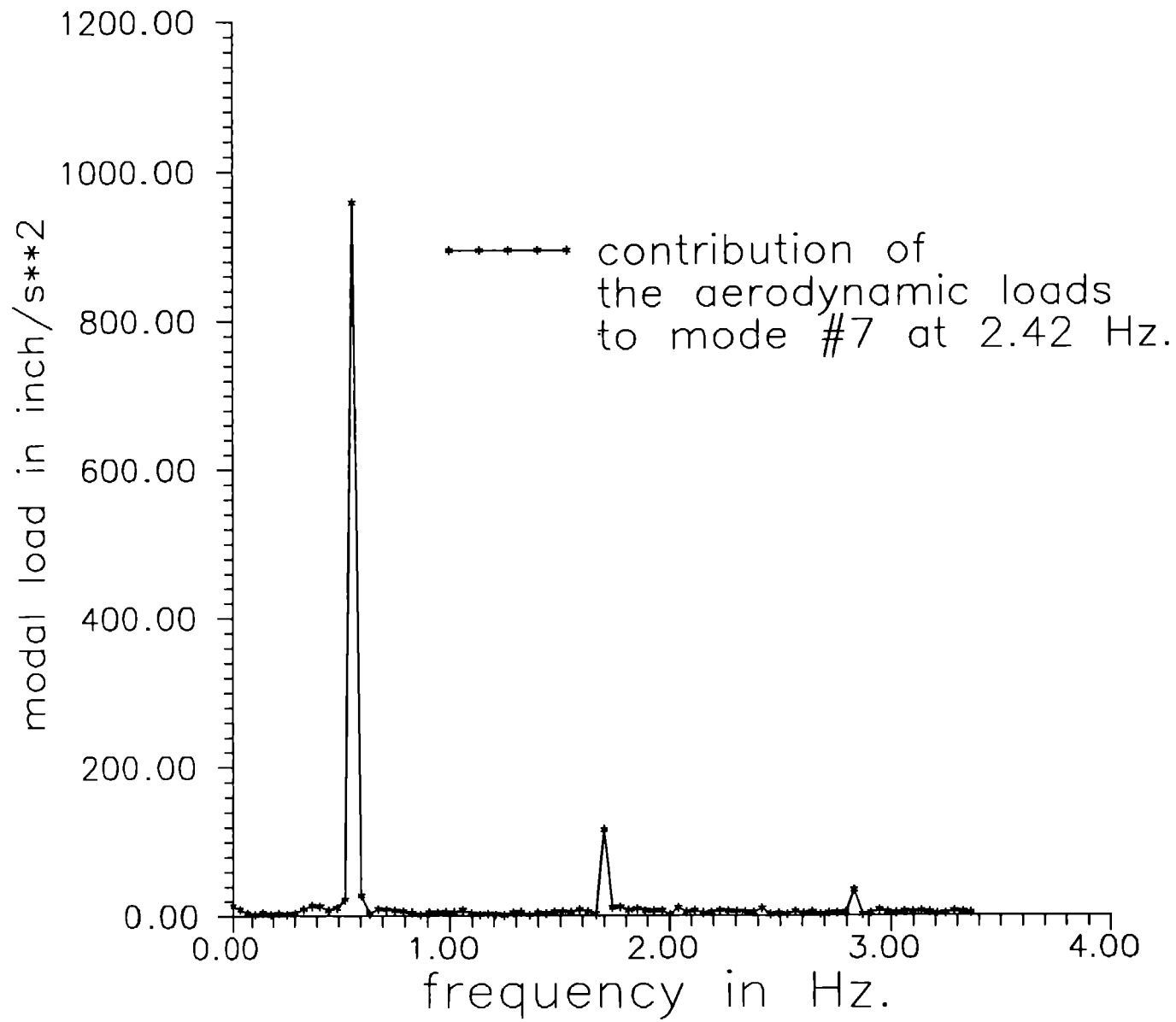


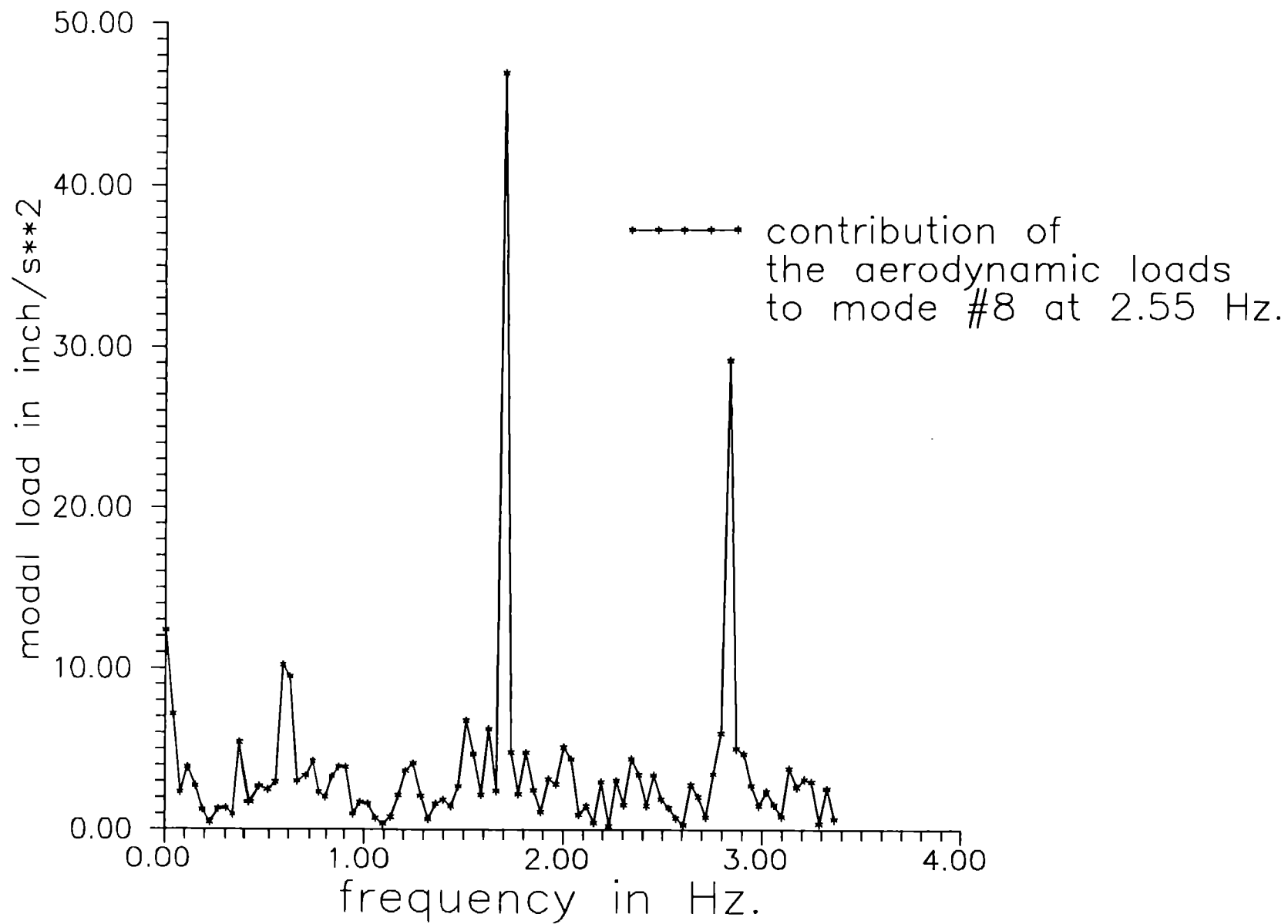


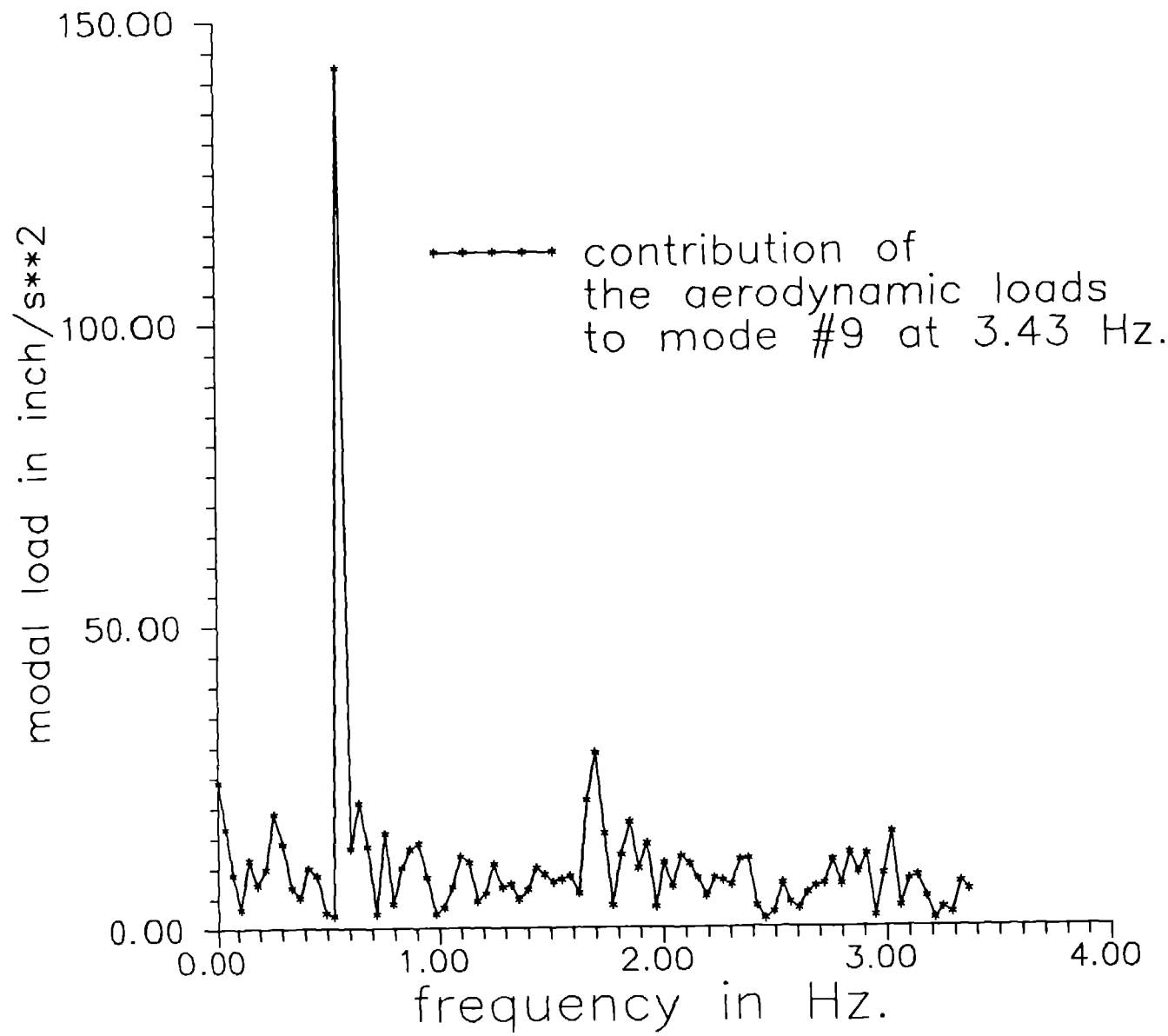


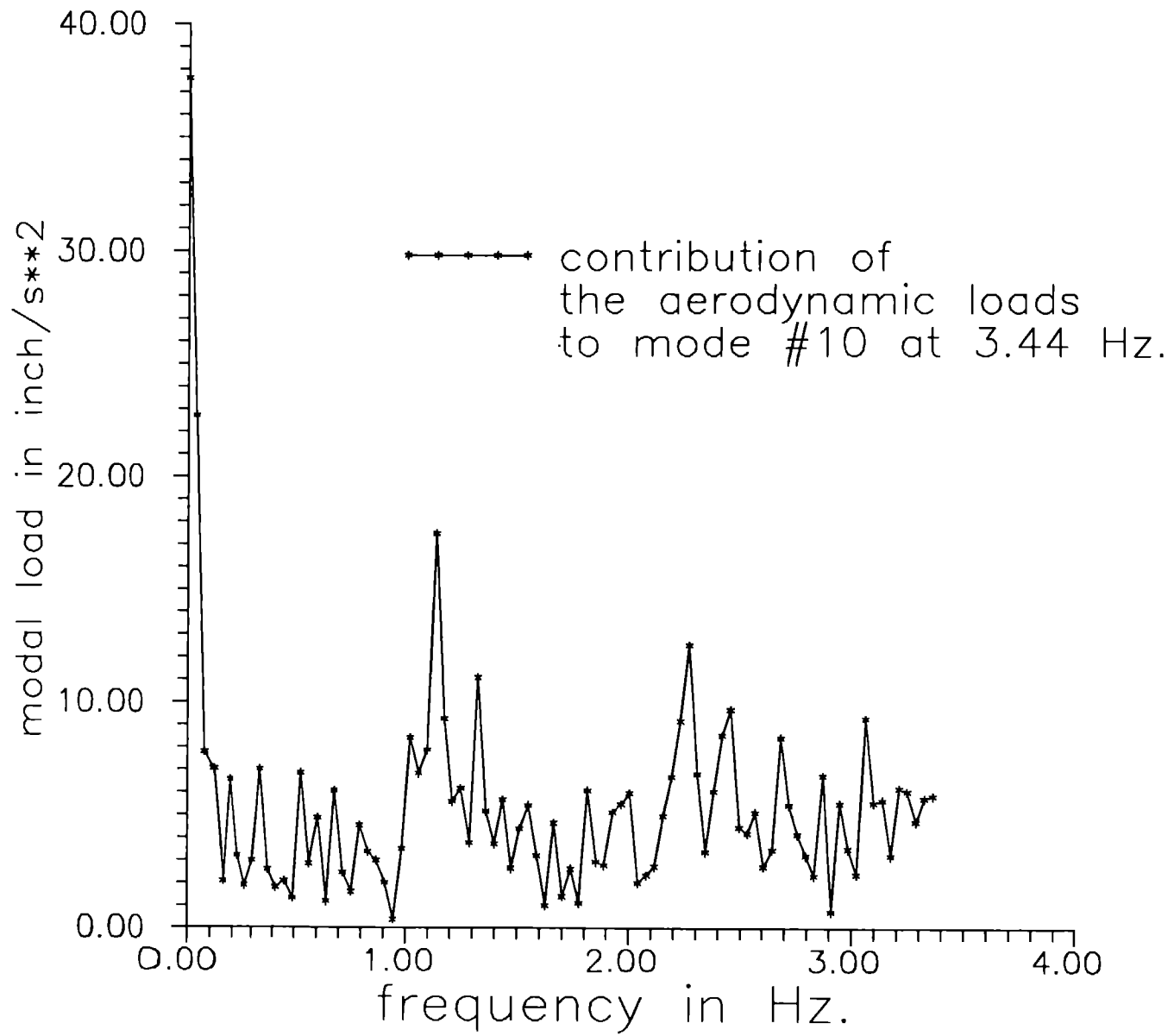


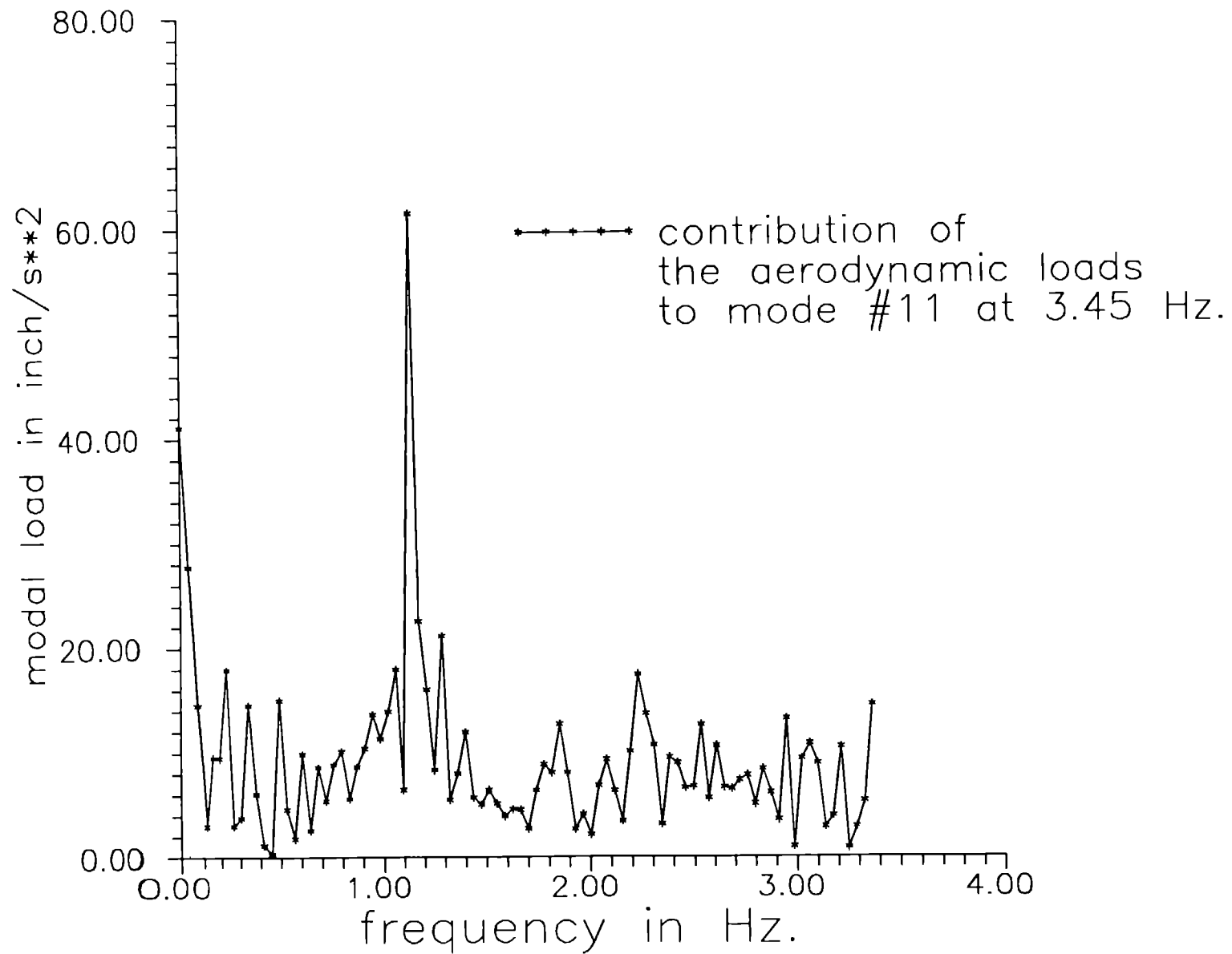


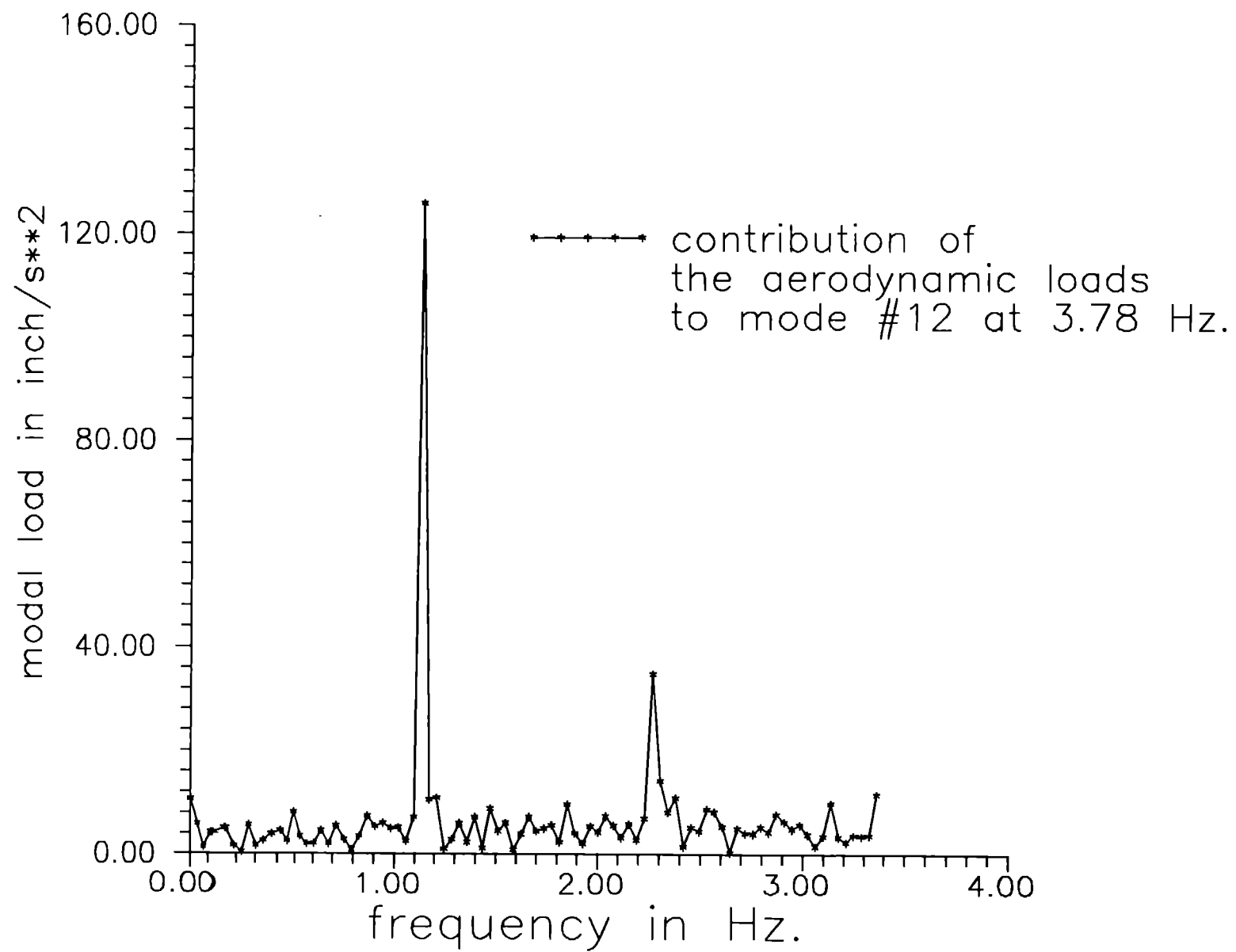


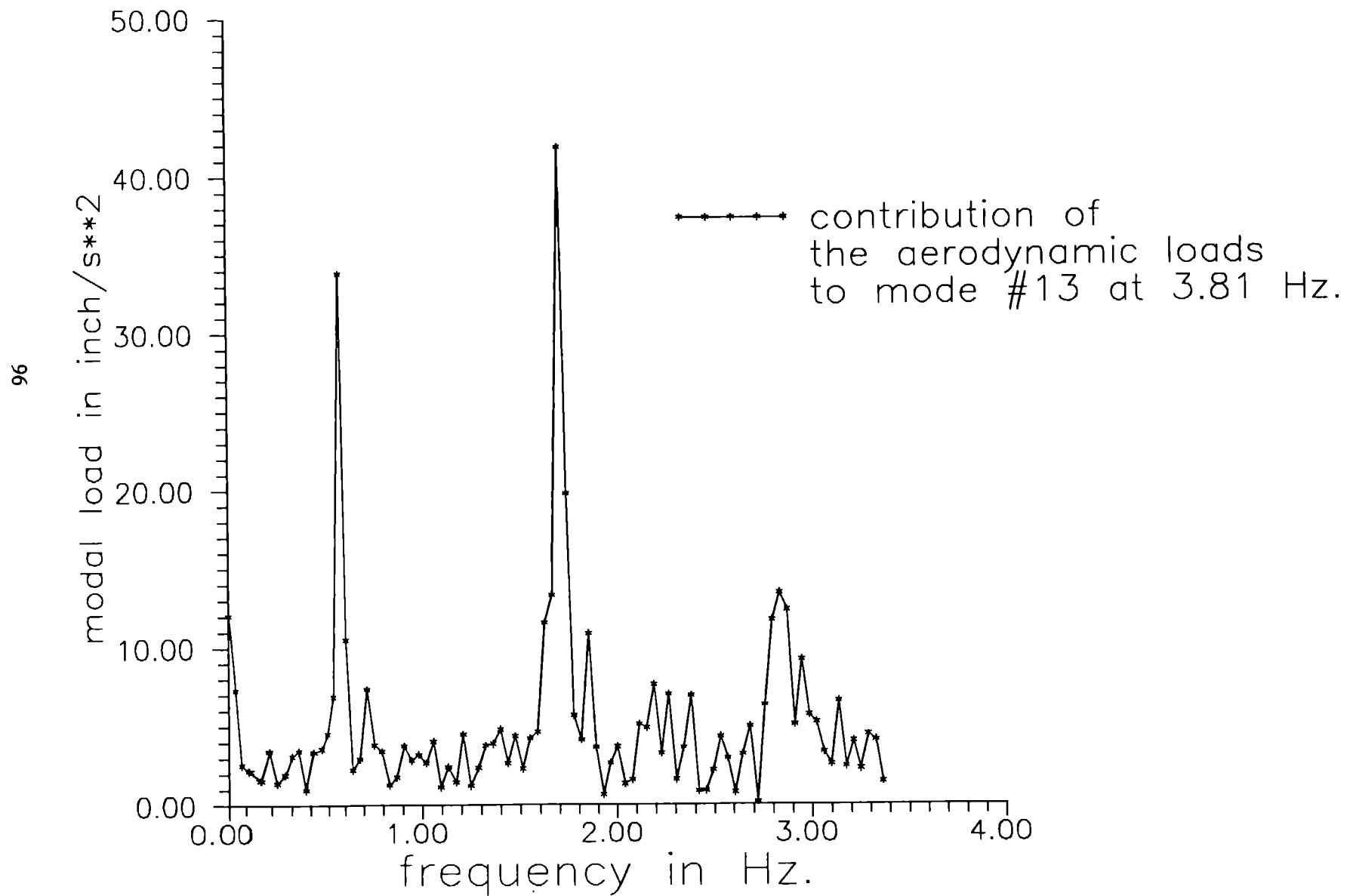


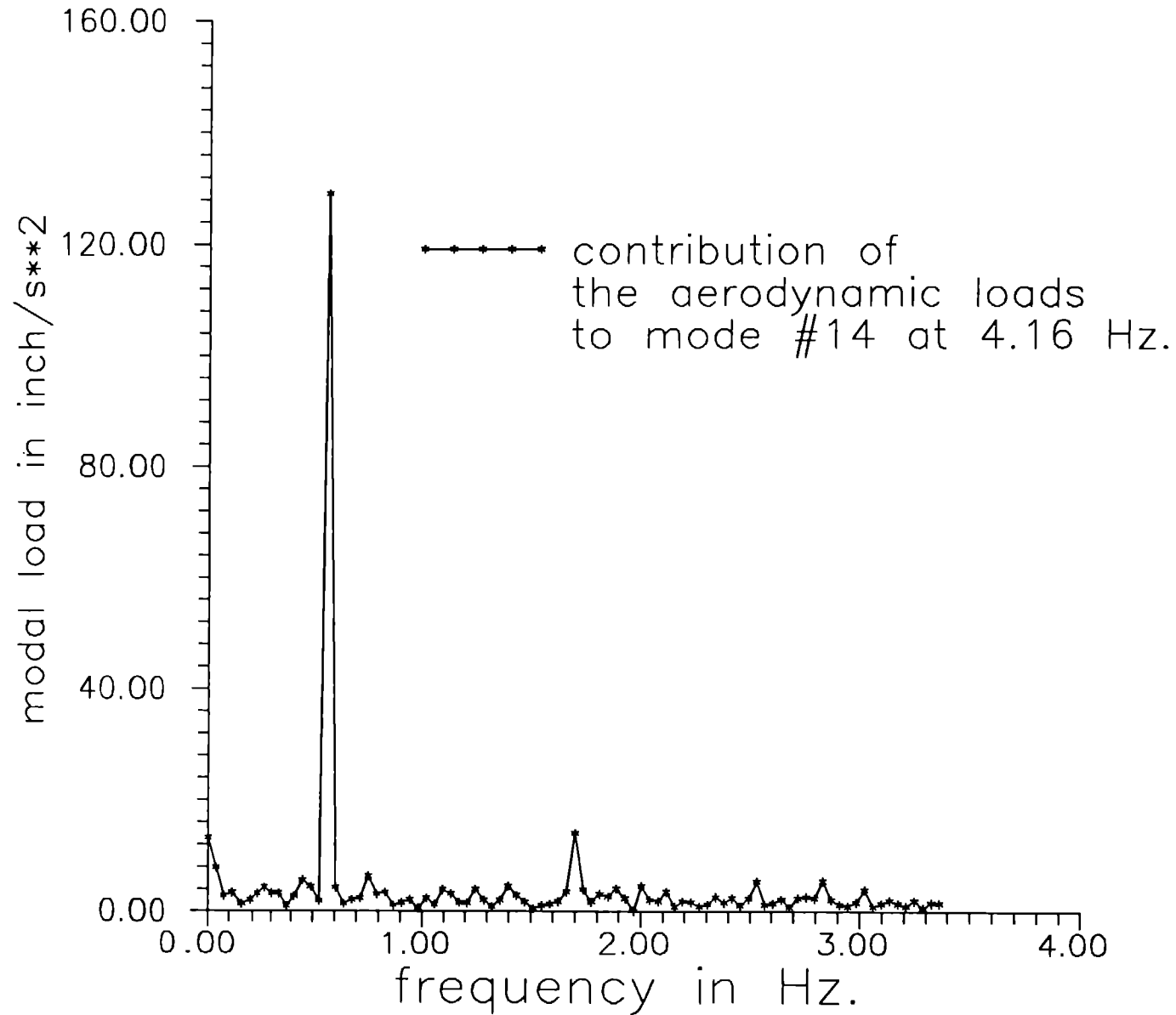


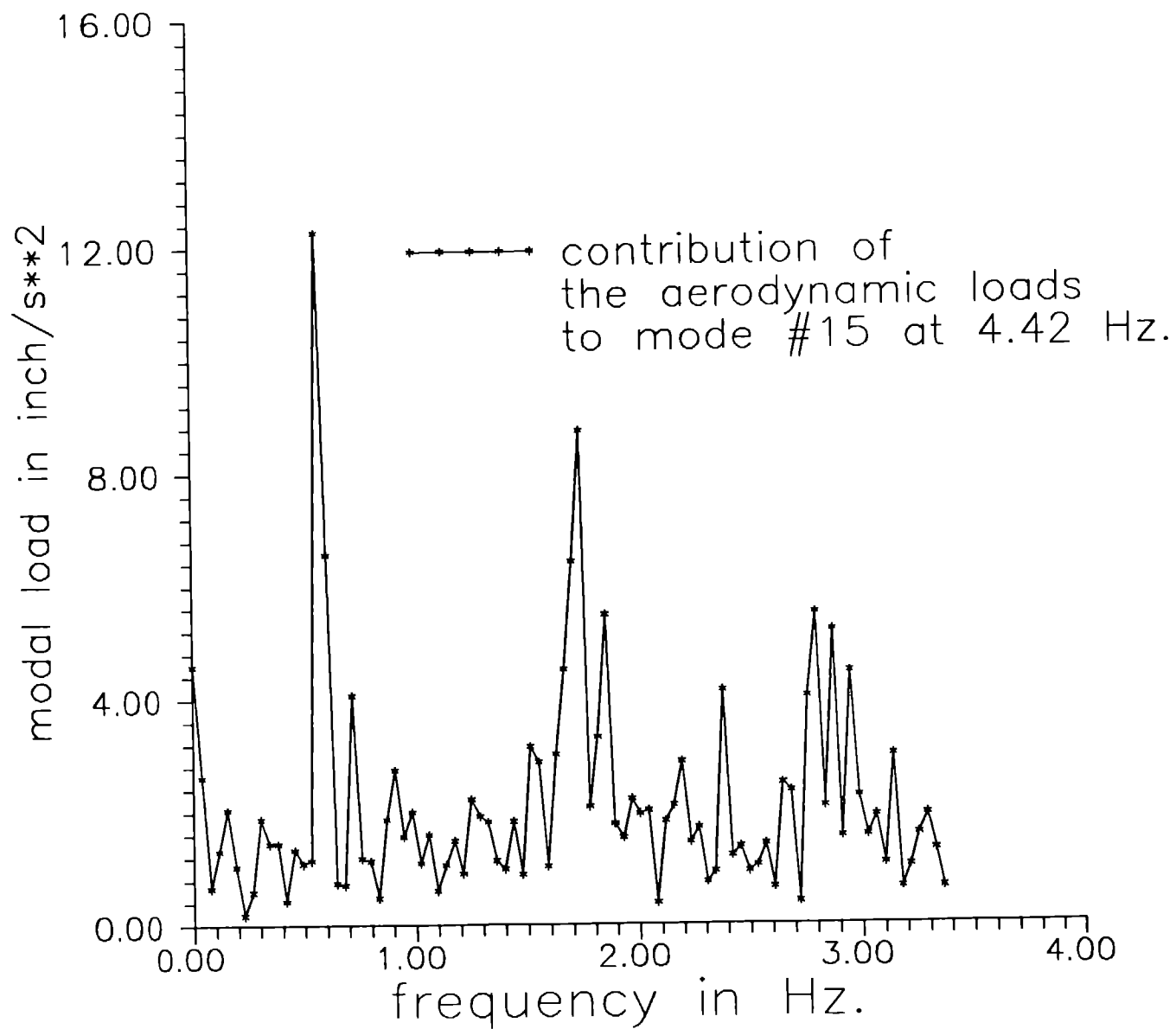


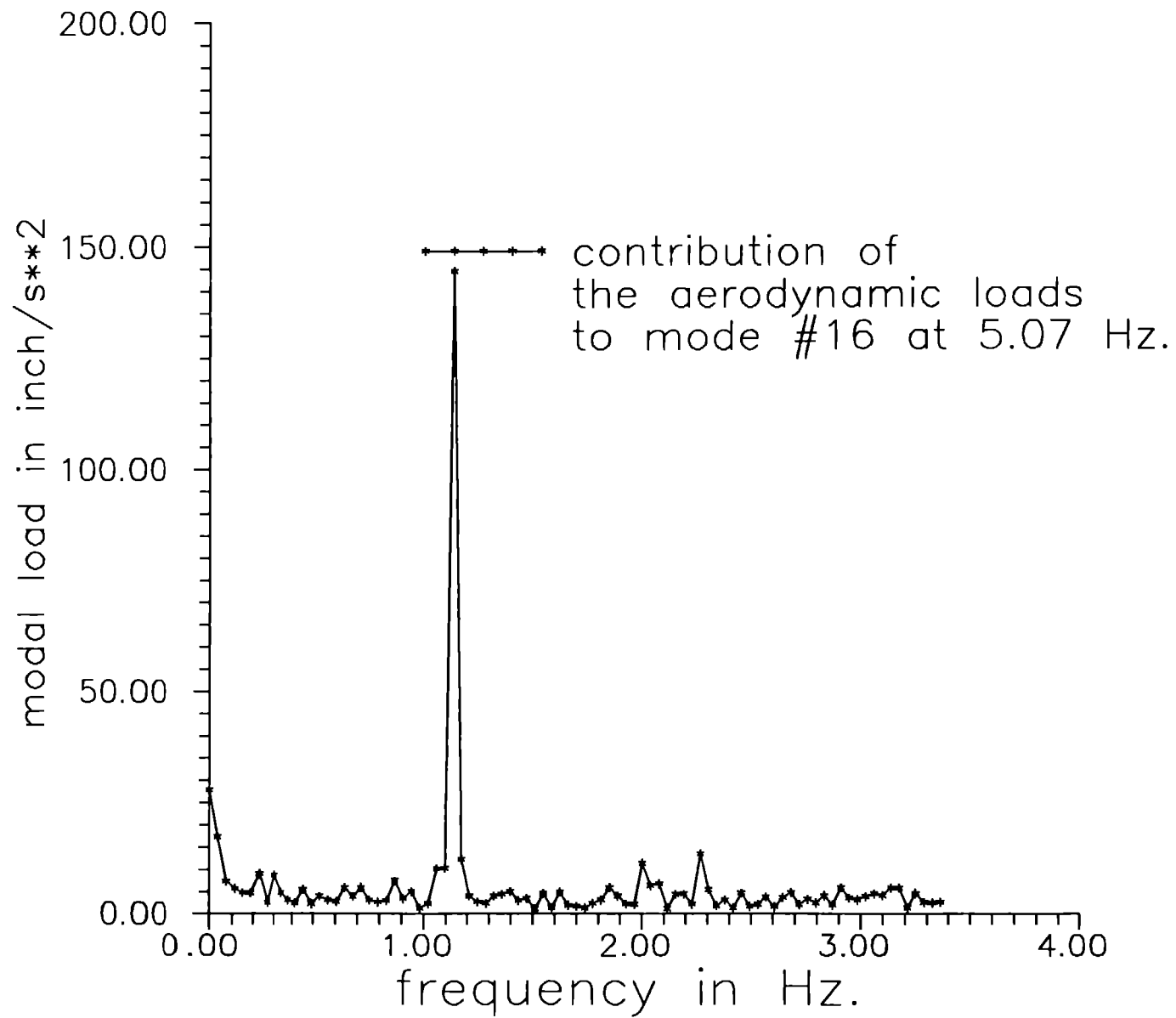


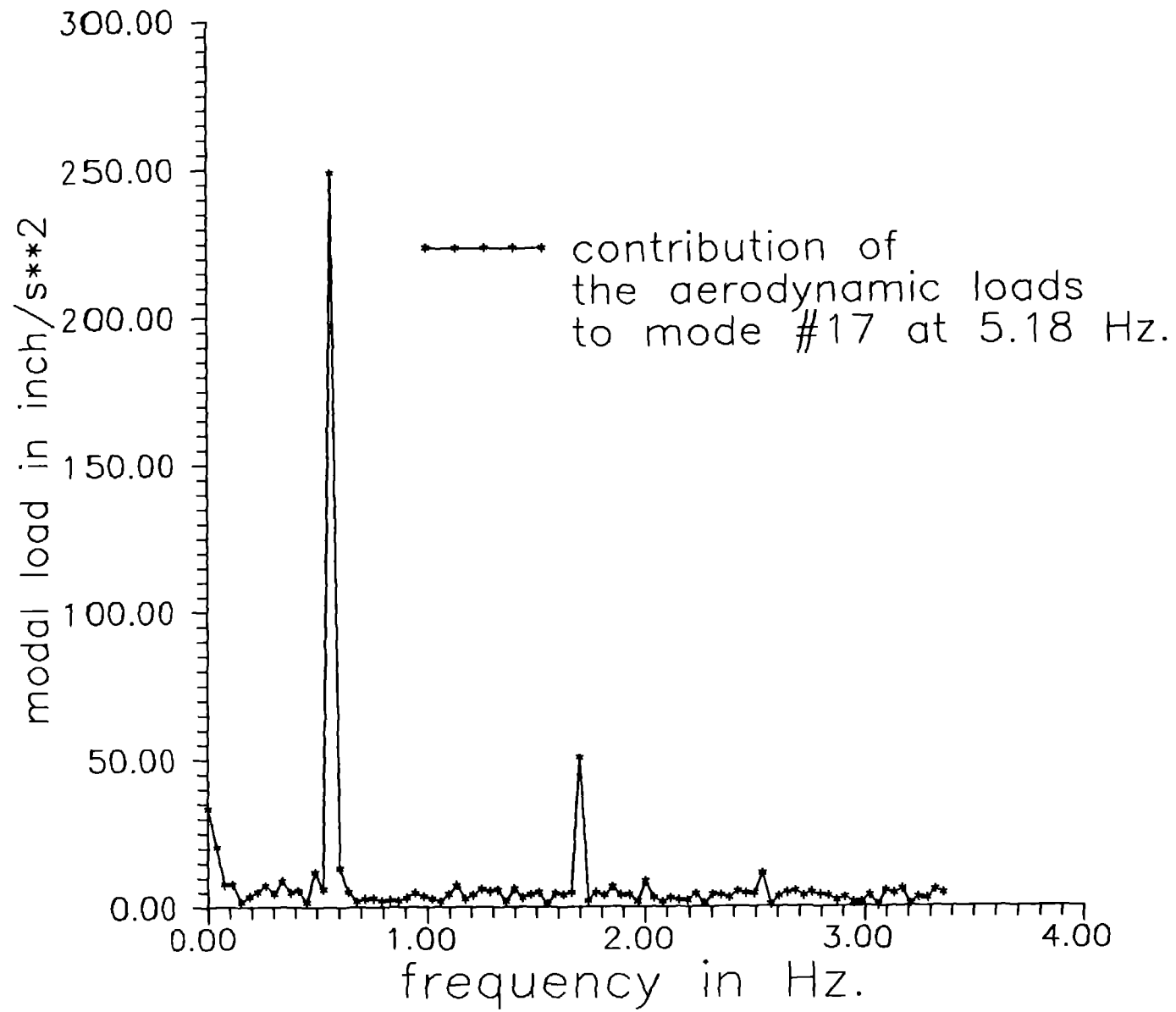


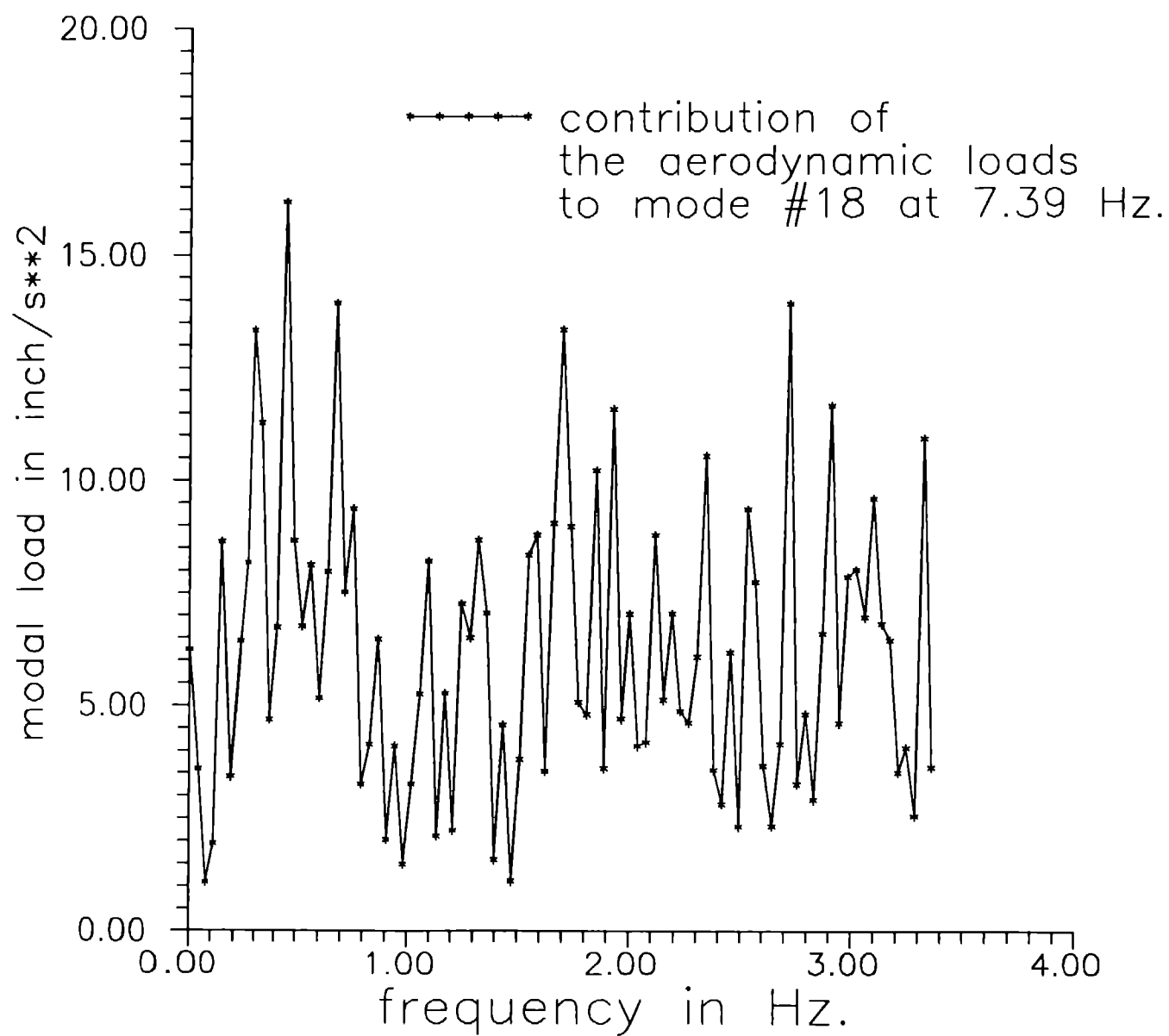


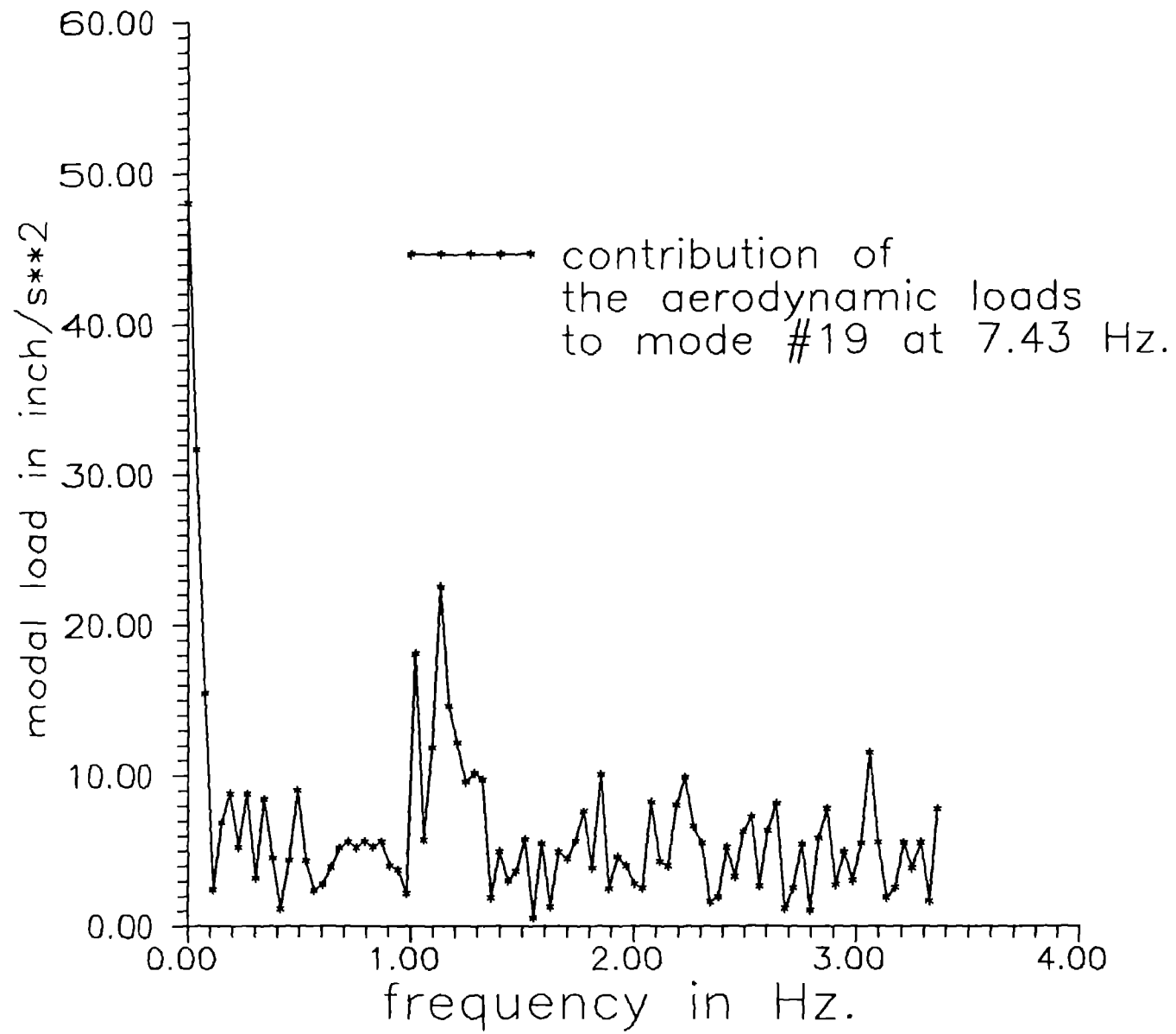


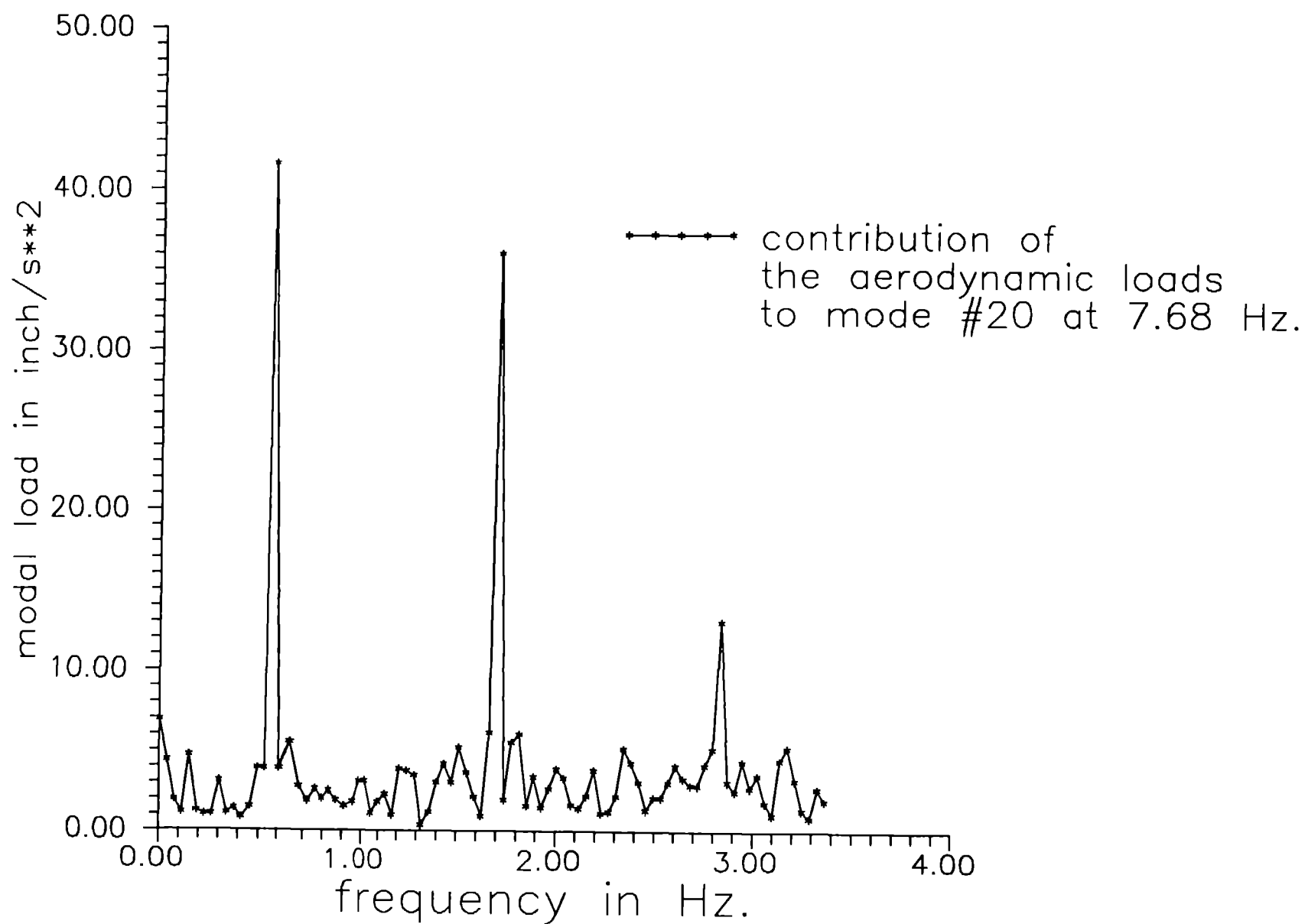












DISTRIBUTION:

D. K. Ai
Alcoa Technical Center
Aluminum Company of America
Alcoa Center, PA 15069

Dr. R. E. Akins
Washington & Lee University
P.O. Box 735
Lexington, VA 24450

Dr. Mike Anderson
Renewable Energy Systems, Ltd.
Eaton Court, Maylands Avenue
Hemel Hempstead
Herts HP2 7DR
UNITED KINGDOM

Dr. M. P. Ansell
School of Material Science
University of Bath
Claverton Down
Bath BA2 7AY
Avon
UNITED KINGDOM

Holt Ashley
Dept. of Aeronautics and
Astronautics Mechanical Engr.
Stanford University
Stanford, CA 94305

K. Bergey
University of Oklahoma
Aero Engineering Department
Norman, OK 73069

Ir. Jos Beurskens
Programme Manager for
Renewable Energies
Netherlands Energy Research
Foundation ECN
Westerduinweg 3
P.O. Box 1
1755 ZG Petten (NH)
THE NETHERLANDS

J. R. Birk
Electric Power Research Institute
3412 Hillview Avenue
Palo Alto, CA 94304

N. Butler
Bonneville Power Administration
P.O. Box 3621
Portland, OR 97208

Dr. R. N. Clark
USDA
Agricultural Research Service
Southwest Great Plains Research
Center
Bushland, TX 79012

C. Coleman
Northern Power Systems
Box 659
Moretown, VT 05660

Otto de Vries
National Aerospace Laboratory
Anthony Fokkerweg 2
Amsterdam 1017
THE NETHERLANDS

E. A. DeMeo
Electric Power Research Institute
3412 Hillview Avenue
Palo Alto, CA 94304

C. W. Dodd
Universal Data Systems
5000 Bradford Drive
Huntsville, AL 35805

J. B. Dragt
Institute for Wind Energy
Faculty of Civil Engineering
Delft University of Technology
Stevinweg 1
2628 CN Delft
THE NETHERLANDS

A. J. Eggers, Jr.
RANN, Inc.
260 Sheridan Ave., Suite 414
Palo Alto, CA 94306

John Ereaux
RR No. 2
Woodbridge, Ontario L4L 1A6
CANADA

Dr. R. A. Galbraith
Dept. of Aerospace Engineering
James Watt Building
University of Glasgow
Glasgow G12 8QG
ENGLAND

A. D. Garrad
Garrad Hasson
9-11 Saint Stephens Street
Bristol BS1 1EE
ENGLAND

P. R. Goldman
Wind/Hydro/Ocean Division
U.S. Department of Energy
1000 Independence Avenue
Washington, DC 20585

Dr. I. J. Graham
Dept. of Mechanical Engineering
Southern University
P.O. Box 9445
Baton Rouge, LA 70813-9445

Professor G. Gregorek
Aeronautical & Astronautical
Dept.
Ohio State University
2300 West Case Road
Columbus, OH 43220

Professor N. D. Ham
Aero/Astro Dept.
Massachusetts Institute of
Technology
77 Massachusetts Avenue
Cambridge, MA 02139

Loretta Helling
Librarian
National Atomic Museum
Albuquerque, NM 87185

T. Hillesland
Pacific Gas and Electric Co.
3400 Crow Canyon Road
San Ramon, CA 94583

Eric N. Hinrichsen
Power Technologies, Inc.
P.O. Box 1058
Schenectady, NY 12301-1058

W. E. Holley
U.S. WindPower
6952 Preston Avenue
Livermore, CA 94550

M. A. Ilyan
Pacific Gas and Electric Co.
3400 Crow Canyon Road
San Ramon, CA 94583

K. Jackson
Dynamic Design
123 C Street
Davis, CA 95616

O. Krauss
Division of Engineering Research
Michigan State University
East Lansing, MI 48825

V. Lacey
Indal Technologies, Inc.
3570 Hawkestone Road
Mississauga, Ontario L5C 2V8
CANADA

A. Laneville
Faculty of Applied Science
University of Sherbrooke
Sherbrooke, Quebec J1K 2R1
CANADA

G. G. Leigh
New Mexico Engineering
Research Institute
Campus P.O. Box 25
Albuquerque, NM 87131

L. K. Liljegren
120 East Penn Street
San Dimas, CA 91773

R. R. Loose, Director
Wind/Hydro/Ocean Division
U.S. Department of Energy
1000 Independence Ave., SW
Washington, DC 20585

Robert Lynette
R. Lynette & Assoc., Inc.
15042 NE 40th Street
Suite 206
Redmond, WA 98052

Peter Hauge Madsen
Riso National Laboratory
Postbox 49
DK-4000 Roskilde
DENMARK

David Malcolm
R. Lynette & Associates, Inc.
15042 N.E. 40th Street, Suite 206
Redmond, WA 98052

Prof. J. F. Mandell
Montana State University
302 Cableigh Hall
Bozeman, MT 59717

Bernard Masse
Institut de Recherche d'Hydro-Quebec
1800, Montee Ste-Julie
Varenes, Quebec J3X 1S1
CANADA

Gerald McNerney
U.S. Windpower, Inc.
6952 Preston Avenue
Livermore, CA 94550

R. N. Meroney
Dept. of Civil Engineering
Colorado State University
Fort Collins, CO 80521

Alan H. Miller
NREL
1617 Cole Boulevard
Golden, CO 80401

R. H. Monroe
Gougeon Brothers
100 Patterson Avenue
Bay City, MI 48706

D. Morrison
New Mexico Engineering
Research Institute
Campus P.O. Box 25
Albuquerque, NM 87131

V. Nelson
Department of Physics
West Texas State University
P.O. Box 248
Canyon, TX 79016

J. W. Oler
Mechanical Engineering Dept.
Texas Tech University
P.O. Box 4289
Lubbock, TX 79409

Dr. D. I. Page
Energy Technology Support Unit
B 156.7 Harwell Laboratory
Oxfordshire, OX11 0RA
UNITED KINGDOM

Chuck Paquette
The American Wind Energy Association
777 N. Capitol Street, NE
Suite 805
Washington, DC 20002

Ion Paraschivoiu
Dept. of Mechanical Engineering
Ecole Polytechnique
CP 6079
Succursale A
Montreal, Quebec H3C 3A7
CANADA

Troels Friis Pedersen
Riso National Laboratory
Postbox 49
DK-4000 Roskilde
DENMARK

Helge Petersen
Riso National Laboratory
Postbox 49
DK-4000 Roskilde
DENMARK

Dr. R. Ganesh Rajagopalan
Assistant Professor
Aerospace Engineering Department
Iowa State University
404 Town Engineering Bldg.
Ames, IA 50011

Raj Rangi
Manager, Wind Technology
Dept. of Energy, Mines and Resources
580 Booth 7th Floor
Ottawa, Ontario K1A 0E4
CANADA

Markus G. Real, President
Alpha Real Ag
Feldeggstrasse 89
CH 8008 Zurich
Switzerland

R. L. Scheffler
Research and Development Dept.
Room 497
Southern California Edison
P.O. Box 800
Rosemead, CA 91770

L. Schienbein
7080 Donlon Way, Suite 210A
Dublin, CA 94568

Thomas Schweizer
Princeton Economic Research, Inc.
12300 Twinbrook Parkway
Rockville, MD 20852

David Sharpe
Dept. of Aeronautical Engineering
Queen Mary College
Mile End Road
London, E1 4NS
UNITED KINGDOM

J. Sladky, Jr.
Kinetics Group, Inc.
P.O. Box 1071
Mercer Island, WA 98040

M. Snyder
Aero Engineering Department
Wichita State University
Wichita, KS 67208

L. H. Soderholm
Agricultural Engineering
Room 213
Iowa State University
Ames, IA 50010

Peter South
ADECON
6535 Millcreek Dr., Unit 67
Mississauga, Ontario L5N 2M2
CANADA

W. J. Steele
Pacific Gas and Electric Co.
3400 Crow Canyon Road
San Ramon, CA 94583

Forrest S. Stoddard
West Texas State University
Alternative Energy Institute
WT Box 248
Canyon, Texas 79016

Derek Taylor
Alternative Energy Group
Walton Hall
Open University
Milton Keynes MK7 6AA
UNITED KINGDOM

G. P. Tennyson
DOE/AL/ETWMD
Albuquerque, NM 87115

Walter V. Thompson	400	R. C. Maydew
410 Ericwood Court	1434	D. W. Lobitz
Manteca, CA 95336	1434	D. R. Martinez
	1511	G. F. Homicz
R. W. Thresher	1514	J. G. Arguello
NREL	1514	H. S. Morgan
1617 Cole Boulevard	1540	J. R. Asay
Golden, CO 80401	1544	R. C. Reuter, Jr.
	1545	C. R. Dohrmann
K. J. Touryan	1552	J. H. Strickland
3701 Hawkins Street, NE	1562	K. E. Metzinger
Albuquerque, NM 87109-4512	1562	E. D. Reedy
	2741	T. G. Carne
W. A. Vachon	2741	G. H. James III
W. A. Vachon & Associates	2741	J. P. Lauffer
P.O. Box 149	2741	R. Rodeman
Manchester, MA 01944	3161	P. S. Wilson
	6214	H. M. Dodd (50)
P. Vittecoq	6214	T. D. Ashwill
Faculty of Applied Science	6214	D. E. Berg
University of Sherbrooke	6214	S. C. Newton
Sherbrooke, Quebec J1K 2R1	6214	M. A. Rumsey
CANADA	6214	L. L. Schluter
	6214	W. A. Stephenson
T. Watson	6214	H. J. Sutherland
Canadian Standards Association	6214	P. S. Veers
178 Rexdale Boulevard	7141	Technical Library (5)
Rexdale, Ontario M9W 1R3	7151	Technical Publications
CANADA	7613-2	Document Processing (10)
		For DOE/OSTI
L. Wendell	8523-2	Central Technical Files
Battelle-Pacific Northwest		
Laboratory		
P.O. Box 999		
Richland, WA 99352		
W. Wentz		
Aero Engineering Department		
Wichita State University		
Wichita, KS 67208		
R. E. Wilson		
Mechanical Engineering Dept.		
Oregon State University		
Corvallis, OR 97331		
M. Zuteck		
MDZ Consulting		
931 Grove Street		
Kemah, TX 77565		